EPFL

Design guidelines for next-generation sodium-nickel-chloride batteries

Daniel Alexander LANDMANN

École
polytechnique
fédérale
de Lausanne

2022

Acknowledgements

Abstract

Sodium-nickel-chloride batteries have a proven track record for backup power applications, but also show great potential for large-scale stationary electricity storage currently dominated by lithium-ion batteries. While lithium-ion cells rely on critical cobalt and lithium, sodium-nickel-chloride batteries are based on abundant, non-critical sodium chloride, nickel, and alumina, and are thus ideally suited for large-scale deployment. However, to be competitive with lithium-ion batteries, the charge and discharge rate capabilities of sodium-nickel-chloride batteries need to be improved and cell production cost needs to be reduced.

In this PhD thesis, rate limiting processes in state-of-the-art sodium-metal-chloride cells are assessed and measures are proposed to improve their performance and reduce cost.

On the negative electrode, plating and stripping of liquid sodium metal from a ceramic Na-β''-alumina electrolyte is investigated at 250 °C in a home-built, specifically-designed high-temperature electrochemical cell. Operating the negative electrode above the melting temperature of sodium eliminates mass transport limitations at the sodium/Na-β''-alumina interface and enables stable cycling at unprecedentedly high current densities above 1000 mA/cm^2 without sodium metal dendrite formation.

On the positive electrode, the chlorination and de-chlorination conversion reactions of nickel and iron in sodium tetrachloroaluminate electrolyte are investigated at 300 °C employing planar model electrodes. Analysis of cyclic voltammetry data reveals a diffusion limitation during oxidation with a diffusion coefficient of $2.3 \cdot 10^{-3}$ cm^2/s for the nickel electrode and an upper bound of $1.2 \cdot 10^{-5}$ cm^2/s for the iron electrode. Post-mortem analysis of the electrodes shows that chlorination of the nickel electrode proceeds via uniform oxidation of nickel and the formation of $NiCl_2$ platelets on the surface of the electrode. In contrast, the chlorination of the iron electrodes proceeds via stress-induced cracking, resulting in non-uniform iron oxidation and the pulverization of the iron electrode. For enhanced rate capability, it is thus important to improve transition-metal-ion diffusion in the tetrachloroaluminate electrolyte, preferably by enhancing metal-ion mobility.

A complementary approach to improve the rate capability of sodium-nickel-chloride batteries is to modify the microstructure of the positive electrode. By moving from planar model electrodes to high-capacity porous electrodes, it is shown how microstructure design can improve sodium-ion transport across the porous positive electrode. By these measures, the nominal discharge current density could be increased from 70 to 150 mA/cm^2 demonstrating the potential for further improvements in rate capability.

To reduce production cost of sodium-nickel-chloride batteries, the replacement of tubular Na-β''-alumina electrolytes by planar Na-β''-alumina electrolyte discs is investigated. Despite their potential for lower cost, the use of planar discs results in severely higher mechanical stress on the electrolyte. A practical solution to mitigate the gas pressure difference is to seal the cell below atmospheric gas pressure allowing implementation of planar electrolyte discs.

Insights into the transport and conversion processes at the electrodes presented in this PhD thesis will contribute to enable competitive high-power sodium-nickel-chloride batteries for stationary electricity storage.

Zusammenfassung

Natrium-Nickel-Chlorid-Batterien haben sich für Notstromanwendungen bewährt, zeigen aber auch Potenzial für stationäre Stromspeicherung, die derzeit von Lithium-Ionen-Batterien dominiert wird. Während Lithium-Ionen-Zellen auf kritisches Kobalt und Lithium angewiesen sind, basieren Natrium-Nickel-Chlorid-Batterien auf reichlich vorhandenem, unkritischem Natriumchlorid, Nickel und Aluminiumoxid und sind daher ideal für den großtechnischen Einsatz geeignet. Um aber mit Lithium-Ionen-Batterien konkurrieren zu können, müssen Lade- und Entladeraten erhöht und die Produktionskosten gesenkt werden.

In dieser Dissertation werden die ratenbegrenzenden Prozesse in Natrium-Metall-Chlorid-Zellen identifiziert und Maßnahmen zur Verbesserung ihrer Leistung und Kostensenkung vorgeschlagen.

An der negativen Elektrode wird die elektrochemische Reduktion und Oxidation von flüssigem Natrium an einem Na-β"-Aluminiumoxid-Elektrolyten bei 250 °C in einer elektrochemischen Hochtemperaturzelle untersucht. Die Verwendung der negativen Elektrode oberhalb der Schmelztemperatur von Natrium eliminiert Massentransport Limitationen an der Natrium/Na-β"-Aluminiumoxid-Grenzfläche und ermöglicht stabile Zyklen mit beispiellos hohen Stromdichten von über 1000 mA/cm^2 ohne Bildung von Dendriten.

An der positiven Elektrode werden die Chlorierung und De-Chlorierung von Nickel und Eisen in Natriumtetrachloraluminat bei 300 °C mit ebenen Modellelektroden untersucht. Lineare Voltammetrie zeigt eine Diffusionslimitierung während der Oxidation mit einem Diffusionskoeffizienten von 2,3·10^{-3} cm^2/s für die Nickelelektrode und 1,2·10^{-5} cm^2/s für die Eisenelektrode. Die Analyse der Elektroden zeigt, dass die Chlorierung der Nickelelektrode durch eine gleichmäßige Oxidation und die Bildung von NiCl$_2$-Plättchen auf der Oberfläche der Elektrode erfolgt. Im Gegensatz dazu führt die Chlorierung der Eisenelektrode zu spannungsinduzierter Rissen, die eine ungleichmäßige Eisenoxidation und Pulverisierung der Eisenelektrode zur Folge haben. Für die Erhöhung der Ratenfähigkeit ist es daher wichtig, die Metall-Ionen-Diffusion im Tetrachloroaluminat zu verbessern, vorzugsweise durch die Erhöhung der Metall-Ionen-Mobilität.

Ein ergänzender Ansatz zur Verbesserung der Ratenfähigkeit von Natrium-Nickel-Chlorid-Batterien ist die Anpassung der Mikrostruktur in der positiven Elektrode. Der Wechsel von ebenen Modellelektroden zu porösen Elektroden mit hoher Kapazität zeigt, wie die Gestaltung der Mikrostruktur den Natriumionentransport durch die poröse Elektrode verbessern kann. Durch diese Maßnahmen konnte die Entladestromdichte von 70 auf 150 mA/cm^2 erhöht werden und weiteres Potenzial für die Erhöhung der Ratenfähigkeit von Natrium-Nickel-Chlorid-Batterien aufgedeckt werden.

Um die Produktionskosten von Natrium-Nickel-Chlorid-Batterien zu senken, wird der Ersatz von röhrenförmigen Na-β"-Aluminiumoxid-Elektrolyten durch Na-β"-Aluminiumoxid-Elektrolyt-Scheiben untersucht. Neben den niedrigeren Kosten führt diese Änderung jedoch zu einer höheren mechanischen Beanspruchung des Elektrolyten. Um den Druckunterschied zu verringern, erwies sich die Reduktion des atmosphärischen Drucks während der Versiegelung der Zelle als probates Mittel.

Die in dieser Dissertation präsentierten Erkenntnisse zu Transport- und Reaktionsprozessen werden zur Erhöhung der Wettbewerbsfähigkeit von Natrium-Nickel-Chlorid-Batterien für die stationäre Stromspeicherung beitragen.

Nomenclature

Greek symbols

$\alpha_{a/c}$ Anodic and cathodic charge transfer coefficient [-]

η_s Surface overpotential [V]

η_C Coulombic efficiency [-]

ρ Density [g/cm^3]

φ_1 Potential of electron conducting phase [V]

φ_2 Potential of ion conducting phase [V]

Δp Pressure difference [pa]

σ Conductivity [S/cm]

σ_{max} Maximum relevant stress [pa]

υ Scan rate [V/s]

Arabic symbols

A Surface area [cm^2]

a Slope from Randles-Sevcik plot [A/cm$^2 \cdot$(V/s)$^{-0.5}$]

C Concentration [mol/cm^3]

D Diffusion coefficient [cm^2/s]

E^0 Equilibrium potential of an electrochemical reaction [V]

E_λ Upper boundary voltage [V]

F Faraday constant [C/mol]

j Current density [A/cm^2]

M Molar mass [g/mol]

m Mass [g]

Q Charge [C]

R Universal gas constant, 8.314 [J/molK]

r Radius [mm]

T Temperature [K]

t Time [s]

t_e Electrolyte thickness [mm]

V Volume [cm^3]

z Number of electrons involved in a electrochemical reaction [-]

Abbreviations

CC	Constant current
CCD	Critical current density for dendrite formation
CE	Counter electrode
CSIR	Council for scientific and industrial research
CV	Constant voltage
DOD	Depth of discharge
EDS	Energy-dispersive x-ray spectroscopy
Fe-FeCl$_2$	Iron-iron chloride electrode
LSV	Linear sweep voltammetry
NaAlCl$_4$	Sodium tetrachloroaluminate
NaNiCl	Sodium-nickel-chloride battery
NaS	Sodium-sulphur battery
Ni-NiCl$_2$	Nickel-nickel chloride electrode
NMC	Nickel manganese cobalt oxide
NiMH	Nickel-metal hydride battery
SEM	Scanning electron microscopy
SHE	Standard hydrogen electrode
SOC	State of charge
WE	Working electrode
XRD	X-ray diffraction
ZEBRA	Zeolite battery research Africa

Contents

1. Introduction

The 2015 Paris agreement on climate change was signed by 195 nations and strives to limit global temperature increase well below 2 °C above pre-industrial levels, binding governments worldwide to reduce global greenhouse gas emissions (e.g. CO_2).[1–3] Electricity production requires particular attention, as this sector currently accounts for about one third of global greenhouse gas emissions.[4] Decarbonization strategies foresee mainly the reduction of fossil-fuel-burning coal and gas power plants towards renewable hydro, wind, and solar power generation.

Already before the Paris agreement, the nuclear disaster of the Japanese Fukushima power plant in 2011 caused governments worldwide to reconsider national electricity supply. As a direct cause of this accident, the European countries Germany, Belgium, and Switzerland decided to follow Austria and Italy towards nuclear-free electricity production.[5] For Switzerland, the phase-out of nuclear technology implies that 19.5 TWh or 32% of the total electricity production have to be covered by alternative and efficiency increasing measures every year till 2034.[6]

Further challenges for future electricity supply arise from the mobility sector. The transition from conventional fossil-fuel-powered internal combustion engines to plug-in hybrids and battery-powered electric vehicles will lead to an increase in electricity demand. The decision of the council of the European Union from 2018 to reduce the CO_2-emission norm for light motorcars from today's 95 g/km in average to 62 g/km in 2030 will accelerate this shift and force car manufacturers to design, build, and sell more electric vehicles in the near future.[7] Synthesis of CO_2 – neutral hydrocarbon based fuels for future marine shipping and aviation will further increase electricity consumption.[8] Since 2017, the "Energiestrategie 2050" regulates the stepwise reduction of CO_2 emissions, phase-out from nuclear power plants and their replacement with more sustainable technologies in Switzerland. A key measure of this action plan is the promotion of domestic renewable electricity production by means of hydro, solar, wind, biomass, and geothermal power to compensate the fossil and nuclear phase-out.[5] Especially solar and wind energy suffer from their intermittent nature due the dependency on local meteorological conditions and season-dependent weather conditions.
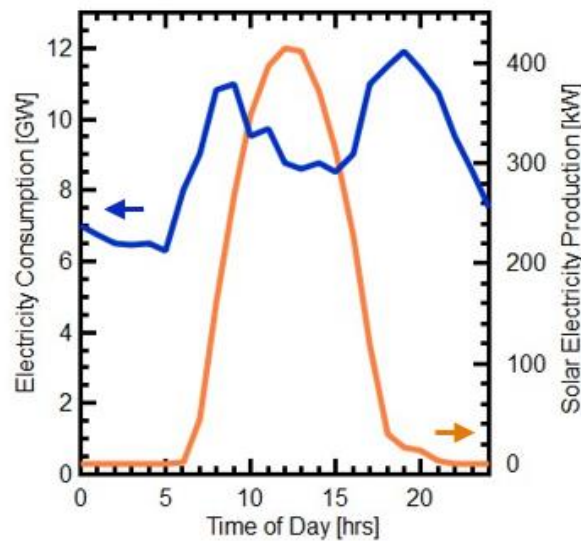
Figure 1-1: Comparison of total electricity consumption in Switzerland[6] and electricity production by Mont Soleil's solar power plant[9] evidencing the temporal mismatch between electricity supply and demand.

In figure 1-1, the orange graph shows an example of the electricity production profile of the photovoltaic plant on Mont Soleil, Switzerland, on a sunny summer day peaking near noon.[9] The blue graph represents Switzerland's total electricity consumption on a typical working day in summer.[6] Two prominent peaks can be found at 9 am and 7 pm.[6] The daily temporal mismatch between renewable electricity production and demand requires an intraday storage solution. Besides pumped hydro and other storage technologies, rechargeable batteries are a formidable solution to store the surplus in electricity production during the day and shift it towards peak demand in the morning and evening hours.[10] Batteries of different size and cell chemistry already power many of our everyday energy needs. A battery stores electrical energy in the form of chemical energy.[10] The chemistry, on which these storage devices rely on, strongly affect their specific energy content, power capability, operating temperature, cost, lifetime, and environmental impact.

Most prominently, lithium-ion batteries enable portable electronic devices such as smart phones and laptops with an energy content of about 10 Wh[11], but also power electric cars with batteries of up to 100 kWh[12]. Also used for stationary applications[13], the largest battery of this type is the 1600 MWh grid storage plant[14], located in Moss Landing, California, USA. The lithium-ion battery most commonly uses a graphite anode and a transition metal-oxide cathode[15, 16]. With a nominal cell potential of 3.7 V, and a gravimetric energy and power density of 250 Wh/kg and 500 W/kg on cell level, these batteries excel most other battery chemistries in terms of performance.[17,18]

In terms of performance, lithium-ion systems are the battery of choice,[19] but their cell chemistry is based on lithium and cobalt, which are classified as critical raw materials by the European Commission due to challenges in the supply chain resulting from geological,

political, economic, ecological, and social factors.[20–23] While it is predicted that lithium and cobalt reserves are sufficient to fulfill the demand in lithium-ion batteries from the mobility sector, not enough lithium and cobalt are available, if lithium-ion batteries are to be deployed at scale for stationary storage applications.[24] For example, the stationary grid storage plant in Moss Landing has a capacity of 1600 MWh[14], mentioned above, comprises about sixteen thousand large, nickel-manganese-cobalt-oxide-based (NMC111) electric car batteries with a total cobalt content of 950 tons.[25]

An alternative to lithium-ion batteries for stationary storage applications are high-temperature sodium-sulphur (NaS) batteries. The sodium-sulfur battery produced by the Japanese company NGK located in Abu Dhabi provides a storage capacity of 648 MWh.[26] This battery type is operated at 300-350 °C, uses a liquid sodium metal anode, sulphur as cathode material, a solid-state ceramic sodium-β"-alumina electrolyte. Consequently, it is constituted exclusively of abundant, non-critical raw materials. With a nominal cell potential of 2.1 V[27], the gravimetric energy and power densities are typically on the order of 120 Wh/kg and 100 W/kg on cell level.[28]

This PhD thesis focuses on a second alternative to lithium-ion batteries, the high-temperature sodium-nickel-chloride (NaNiCl) battery. These are also operated at 300 °C and provide higher gravimetric energy and power densities on the order of 140 Wh/kg[29] and 179 W/kg[29,30] on cell level than NaS cells. Sodium-nickel-chloride batteries avoid the use of critical and rare elements.[16,20,31] Similar to sodium sulfur batteries, these batteries feature a liquid sodium metal anode, a solid-state ceramic sodium-β"-alumina, but replace the sulfur on the positive electrode with nickel as active material.[32] These batteries are produced in Switzerland by the Swiss company FZSonick and are already successfully deployed for backup power applications in mobile telecommunication antennas.[33] In particular, their low self-discharge rate compared to lithium-ion batteries qualifies sodium-nickel-chloride batteries for backup power applications.[34] However, sodium-nickel-chloride batteries also show great potential for large-scale stationary electricity storage[29,35], as successfully shown with a 0.54 MWh installation in Switzerland (figure 1-2).[36] When comparing the lithium-ion to the sodium-nickel-chloride battery's energy and power density, one has to consider that comparison on a system level is more favorable for the sodium-nickel-chloride chemistry. Overall, this results in a relatively small reduction in specific energy, but still a significant drawback in specific power for the sodium-nickel-chloride chemistry. Origin is the narrow optimal operating temperature of 15-35 °C for lithium-ion batteries leading to heating, cooling requirements and additional weight on a battery system level,[37] while the sodium-nickel-chloride battery's high operating temperature requires heating only. A summarized overview comparing energy density, power density, nominal cell voltage, and operating temperature of Li-ion, NaS, and NaNiCl batteries is shown in table 1-1.

Figure 1-2: Largest sodium-nickel-chloride battery in Switzerland with a capacity of 0.54 MWh, image taken with permission from: Genossenschaft Migros Zürich.

	Li-ion	NaS	NaNiCl
Energy density [Wh/kg]	250	120	140
Power density [W/kg]	500	100	179
Nominal cell potential [V]	3.7	2.1	2.58
Ideal operating temperature [°C]	15-35	350	300

Table 1-1: Comparison of Li-ion, NaS, and NaNiCl batteries, data from ref. 17, 18, 27-30.

This PhD thesis investigates the rate limiting processes in sodium-nickel-chloride batteries with the aim to derive design guidelines to improve the power performance of this technology enabling application in the emerging stationary electricity storage market. Ideally, design guidelines should also facilitate cell assembly to reduce cell manufacturing cost while promoting long-term cycling stability, which is key for reducing the cost of energy stored per cycle and the levelized cost of energy stored.

1.1 History of the sodium-nickel-chloride battery

Sodium-nickel-chloride batteries belong to the group of molten salt or ZEBRA batteries, which is a group of rechargeable high-temperature sodium-metal chloride batteries operated at around 300 °C. The term ZEBRA stems from a research project at the Council for Scientific and Industrial Research (CSIR) in Pretoria, South Africa, named "**ZE**olite **B**attery **R**esearch **A**frica". Later, the acronym was associated with the more general description of "**Z**ero **E**mission **B**attery **R**esearch **A**ctivities".

The development of these high-temperature sodium batteries dates back to 1967, when engineers at Ford Motor Company first presented a rechargeable sodium-sulfur battery cell.[39] Towards a battery technology for motive power applications, they selected electrode materials in the molten state, providing a high mobility of electroactive species. A Na-β''-alumina ceramic as solid electrolyte provided an unprecedented match of high and selective ion conductivity with good mechanical and (electro-) chemical stability.[40] However, the highly corrosive molten sulfur cathode and its violently exothermic reaction in contact with sodium upon cell rupture impeded initial commercial applications of sodium-sulfur batteries, and triggered efforts to implement alternative materials on the positive electrode.

This motivated research on a safer high-temperature technology, leading to a first patent application on sodium-metal chloride cells by CSIR in 1978.[41] The new technology, which would later become the ZEBRA battery, took over the tried and tested Na-β''-alumina electrolyte and liquid sodium anode from the sodium-sulfur technology. At the positive electrode, it applied solid transition metal chlorides immersed in a molten salt, sodium tetrachloroaluminate electrolyte ($NaAlCl_4$) to enable fast reaction kinetics and a high mobility of electroactive species. At first, the development of sodium-metal chloride cells focused on iron as transition metal, providing a theoretical capacity of 310 mAh/g.[42] The results were reported in scientific literature only after a decade of development, in 1986.[42] As one of the researchers, Johan Coetzer at CSIR, pointed out, a viable battery required a suitable combination of electrochemical performance, materials cost, and safety characteristics. By that time, $Na/Fe\text{-}FeCl_2$ cells had already been successfully applied in electric cars with batteries on kWh-scale, demonstrating a safe chemistry. Soon after, further progress was demonstrated for cells based on nickel ($Na/Ni\text{-}NiCl_2$) instead of iron, providing a comparable theoretical capacity (305 mAh/g), but higher cell voltage (2.59 V for $Ni\text{-}NiCl_2$ vs. 2.35 V for $Fe\text{-}FeCl_2$ at 250 °C).[41] Even more importantly, $Na/Ni\text{-}NiCl_2$ cells provided a superior cycle life, compared to $Na/Fe\text{-}FeCl_2$ cells.[32] In addition, cells were now assembled in the discharged state, without the need to handle metal chlorides and metallic sodium. Instead, a sintered mixture of Ni metal and NaCl powder was applied as positive electrode, and the sodium negative electrode was generated electrochemically during the first charge. Further improvements were made by introducing the electrode materials in compacted powder

form, and by improving cell and battery design to suit the target markets of industrial traction and automotive applications.[43] After another decade, in 1998, AEG Anglo Batteries produced maintenance-free ZEBRA battery systems for electric vehicles in a pilot line, which offered higher energy density than the lead acid and NiMH batteries available at that time.[44] Soon after, an improved ZEBRA battery type was demonstrated, providing a specific energy of about 140 Wh/kg on cell level.[45] In 1999, the company MES-DEA acquired and industrialized the ZEBRA battery technology in Stabio, Switzerland,[34] with a focus on electromotive applications. In a first phase, a production capacity of 40 MWh per year was implemented with a specific energy and power of 120 Wh/kg and 180 W/kg on cell level, with respect to the entire battery system.[34,46] In 2011, General Electric (GE) entered development and fabrication of commercial sodium-nickel-chloride batteries in the US, with large-scale grid storage as a target market. However, market expectations in terms of demand were too high at that time, and consequently GE had to first drastically scale back and finally cease production of this battery technology in 2015.[47–49]

Currently the only remaining producer of commercial sodium-nickel-chloride batteries is the company FzSoNick in Switzerland. Their batteries are mainly deployed as back-up power source for telecommunication antennas, but also show strong potential for large-scale grid storage needed for the implementation for renewable energy production.[29,33,35]

1.2   Working principle of the sodium-nickel-chloride battery

1.2.1 Construction and cell reactions

Cells in a sodium-nickel-chloride battery feature a liquid sodium metal negative and a porous positive electrode mainly consisting of interconnected nickel particles and sodium chloride (figure 1-3). Both electrodes are separated by a ceramic sodium-β''-alumina (Na-β''-alumina) electrolyte. A secondary electrolyte consisting of molten tetrachloroaluminate ($NaAlCl_4$) saturated with sodium chloride (NaCl) fills the pores in the positive electrode compartment.

Sodium-nickel-chloride batteries are operated near 300 °C. At this temperature, the sodium-ion conductivity of Na-β''-alumina (~0.2 S/cm[46]) and molten $NaAlCl_4$ (~0.65 S/cm[50]) is sufficiently high to enable continuous discharge currents densities of up to 50 mA/cm^2 in commercial cells.[29,30,51] $NaAlCl_4$ saturated with NaCl can be treated as a concentrated mixture of a binary molten salt with Na^+ and Cl^- ions and neutral $AlCl_3$ species.[52]

In commercial cells, the major constituents of the cathode, Ni and NaCl, are combined with Al and Fe to improve the battery performance according to the following reactions (cell potentials at 280±20 °C):[46,53]

$$Al + 4\,NaCl \leftrightarrow NaAlCl_4 + 3\,Na, \quad E^0 \approx 1.60 \text{ V vs. } Na/Na^+ \qquad \text{Reaction 1}$$

$$Fe + 2\,NaCl \leftrightarrow FeCl_2 + 2\,Na, \quad E^0 \approx 2.35 \text{ V vs. } Na/Na^+ \qquad \text{Reaction 2}$$

$$Ni + 2\,NaCl \leftrightarrow NiCl_2 + 2\,Na, \quad E^0 \approx 2.58 \text{ V vs. } Na/Na^+ \qquad \text{Reaction 3}$$
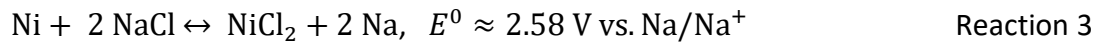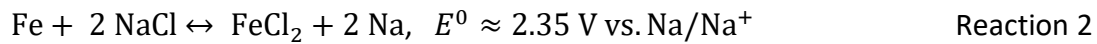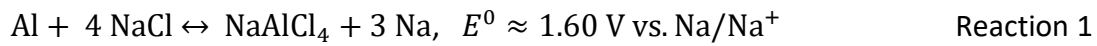
Only during first charge above 1.6 V, small amounts of Al lead to additional sodium at the negative electrode, and additional NaAlCl4 at the positive electrode following reaction (1). At the same time, electrochemical oxidation of Al increases the rate performance by enlarging the available surface area of the solid electrode materials. Reaction 1 is usually not used in normal battery operation, where a lower voltage limit at 1.8 V vs. Na/Na+ is enforced by the battery management system. Iron (2) enhances the pulse power capability at high depths of discharge (DOD), while decreasing materials cost. Nickel (3) is applied in excess to maintain electronic conductivity in the electrode at all states of charge (SOC), utilizing about 30 % in the electrochemical reaction.[45] The low utilization rate of nickel significantly reduces the gravimetric energy density of the cathode composite, e.g. from theoretically 305 mAh/g to about 159 mAh/g.[54,55] However, the presence of a percolating, unreacted nickel backbone is required to ensure electronic conduction through the thick cathode also in fully charged cells.[56] Loss of contact, resulting from conversion of nickel to electronically insulating nickel chloride during prolonged charge/discharge cycling represents an important capacity fading mechanism

Chlorination of nickel starts in proximity of the Na-β''-Al$_2$O$_3$ electrolyte and proceeds away from it towards the cathode current collector as the battery is charged.[50] This causes an increase of cell resistance as the battery charging proceeds. This is ascribed to prolonged ionic pathways, which directly affect the charge (but also discharge) power capability of the cell. The progression of the reaction front strongly depends on the surface area of the porous nickel electrode and other microstructural parameters such as the tortuosity and length of the ion path.

Sodium-nickel-chloride cells are always assembled in the discharged state.[56] During the first charge, also called maiden charge, sodium is electrochemically produced by plating in the anode compartment following the reaction:[57]

$$Na \leftrightarrow Na^+ + e^- \qquad \text{Reaction 4}$$

To avoid depletion of sodium on the anode side during consecutive cycles, only 80-85% of the sodium plated during the maiden charge is cycled.[58] Cells are typically cycled for about 10 cycles, during which cell resistance reduces before they are send out to the customer.[56,59,60]
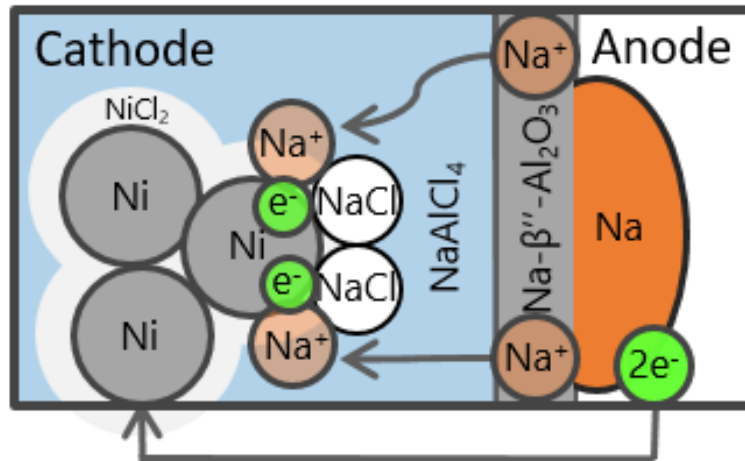
Figure 1-3: Working principle of a sodium-nickel-chloride battery during discharge.

1.2.2 Operational safety

Operational safety is a clear advantage of this technology.[61] In terms of cell chemistry, the dominating failure mode is of a passivating nature. This is because the molten phases, sodium and the salt electrolyte (NaAlCl$_4$), react to rock salt and aluminum. These phases are solid up to temperatures of 800 °C and 660 °C, respectively.[46,62]
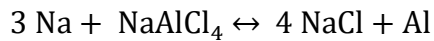
$$3 \text{ Na} + \text{ NaAlCl}_4 \leftrightarrow 4 \text{ NaCl} + \text{Al} \qquad\qquad\qquad \text{Reaction 5}$$

As a result, eventual cracks in the ceramic electrolyte lead to electric short-circuiting of a cell by formation of percolating aluminum structures. These short circuits represent a safe failure mechanism, and batteries comprising hundreds of cells were demonstrated to operate with 5-10% failed cells, at slightly reduced cell voltage.[46] As the only battery chemistry, sodium-nickel-chloride packs fulfil the UL9540A test norm, making thermal run away an unlikely event.[63] Further studies with abusive testing of sodium-nickel-chloride batteries proved the safe failure mode.[57,62,64]

1.3   Objectives and outline of this PhD thesis

Sodium-nickel-chloride batteries are based on abundant and cheap raw materials, namely rock salt, nickel, and alumina. They are a viable candidate for environmentally benign and safe, large-scale electricity storage. However, while being compatible in terms of energy density, the rate capability of sodium-nickel-chloride is significantly lower and cell cost is higher compared to state-of-the-art lithium-ion batteries.

This PhD thesis investigates the rate limiting processes in sodium-nickel-chloride batteries with the aim to derive design guidelines for improved the power performance of this technology and enable application in the emerging stationary electricity storage market. Ideally, design guidelines should also facilitate cell assembly to reduce cell-manufacturing cost and promote long-term cycling stability, which is key for reducing the cost of energy stored by cycle and the leveled cost of energy stored.

The outline of this PhD thesis below is provided as a guide to the reader. As the main part of this thesis in chapters 3, 4, 5, and 6 contains published articles, certain redundancies cannot be avoided.

Chapter 2 gives an overview of methods applied and developed in this PhD thesis. A modular, self-designed high-temperature electrochemical cell serves as experimental platform for most of the experiments. Its design is described in this chapter. Governing equations related to battery modelling are introduced and set into the context of sodium-nickel-chloride batteries along with a short description of electrochemical techniques applied in this thesis.

In **chapter 3**, potential rate limitations arising from the battery's liquid sodium negative electrode in contact with the ceramic Na-β''-alumina electrolyte are investigated in symmetric cell configuration. Stripping and plating at 10-2600 mA/cm^2 and temperatures ranging between 140 and 250 °C revealed that the negative electrode is not limiting the overall rate-performance of the sodium-nickel-chloride battery.

The conversion reaction occurring on the positive electrode of the sodium-nickel-chloride battery is investigated in **chapter 4** in asymmetric cell configuration. Planar model electrodes are employed to isolate phenomena associated with the de-/chlorination of the nickel and iron electrodes in sodium tetrachloroaluminate (NaAlCl$_4$) at 300 °C from microstructural effects dominating porous electrodes. Combining electrochemical methods with post-mortem morphological analysis of the electrodes reveals that de-/chlorination of nickel is very different from de-/chlorination of iron from which important battery design guidelines are derived.

In **chapter 5**, design guidelines derived from planar model electrodes are applied to enhance the rate capability of high-capacity porous electrodes demonstrating unprecedented current densities.

Chapter 6 gives a perspective on potential cell cost reduction in sodium-nickel-chloride batteries. Replacing the currently used tubular Na-β''-alumina electrolytes by planar Na-β''-alumina electrolyte discs promises cost advantages due to facilitated quality control and cell manufacturing, but results in higher mechanical stress on the planar electrolyte induced by volume changes on the negative and positive electrode upon cycling.

Finally, **chapter 7** concludes this thesis and gives an outlook on future work to be carried out in order to enhance the rate-capability of sodium-nickel-chloride batteries.

References

[1]   M. Hulme, *1.5°C and climate research after the Paris agreement*, Nat. Clim. Chang., 2016, *6,* 222.

[2]   J. Rogelj, M. Den Elzen, N. Höhne, T. Fransen, H. Fekete, H. Winkler, R. Schaeffer, F. Sha, K. Riahi, M. Meinshausen, *Paris agreement climate proposals need a boost to keep warming well below 2 °C*, Nature, 2016, *534*, 631.

[3]   R. Falkner, *The Paris agreement and the new logic of international climate politics*, Int. Aff., 2016, *92*, 1107.

[4]   T. Goh, B. W. Ang, B. Su, H. Wang, *Drivers of stagnating global carbon intensity of electricity and the way forward*, Energy Policy, 2018, *113*, 149.

[5]   Swiss Federal Council, *Message for energy strategy 2050*, 2013, *2050*.

[6]   Bundesamt für Energie, *Schweizerische Elektrizitätsstatistik 2016 / Statistique suisse de l' électricité 2016*, 2017, 1.

[7]   Council of the EU and recycling, Press Release, 2018, 18, URL: https://www.consilium.europa.eu/en/press/press-releases/2018/10/10/co2-emission-standards-for-cars-and-vans-council-agrees-its-position/, Date accessed: September 3, 2021.

[8]   K. Boulouchos, C. Bach, C. Bauer, D. Bucher, D. Cerruti, A. Dehdarian, M. Filippini, M. Held, S. Hirschberg, R. Kannan, T. Kober, A. Mancera Sugrañes, V. De Martinis, A. Mic, *Pathways to a net zero CO_2 swiss mobility system SCCER mobility whitepaper*, SCCER Mobil. Whitepaper, 2021.

[9]   Société Mont-Soleil, Stromproduktion Sonnenkraftwerk Mont-Soleil, URL: http://www.societe-mont-soleil.ch/stromproduktion.159.html, Date Accessed: 8th January 2019.

[10]   D. H. Doughty, P. C. Butler, A. A. Akhil, N. H. Clark, J. D. Boyes, *Stationary electrical energy storage*, Electrochem. Soc. Interface, 2010, *19*, 49.

[11]   D. Bresser, K. Hosoi, D. Howell, H. Li, H. Zeisel, K. Amine, S. Passerini, *Perspectives of automotive battery R&D in China, Germany, Japan, and the USA*, J. Power Sources, 2018, *382*, 176.

[12]   M. Armand and J.-M. Tarascon, *Building better batteries*, Nature, 2008, *451*, 2.

[13]   D. Choi, N. Shamim, A. Crawford, Q. Huang, C. K. Vartanian, V. V. Viswanathan, M. D. Paiss, J. E. Alam, D. M. Reed, V. L. Sprenkle, *Li-ion battery technology for grid application*, J. Power Sources, 2021, *511*, 230419.

[14]   Vistra Corp., Vistra completes expansion of battery energy storage system at its flagship california facility, URL: https://www.energy-storage.news/at-300mw-1200mwh-the-worlds-largest-battery-storage-system-so-far-is-up-and-running/, Date accessed: September 3, 2021.

[15]   Q. Liu, X. Su, D. Lei, Y. Qin, J. Wen, F. Guo, Y. A. Wu, Y. Rong, R. Kou, X. Xiao, F. Aguesse, J. Bareño, Y. Ren, W. Lu, Y. Li, *Approaching the capacity limit of lithium cobalt oxide in lithium-ion batteries via lanthanum and aluminium doping*, Nat. Energy, 2018, *3*, 936.

[16]   R. Wagner, N. Preschitschek, S. Passerini, J. Leker, M. Winter, *Current research trends and prospects among the various materials and designs used in lithium-based batteries*, J. Appl. Electrochem., 2013, *43*, 481.

[17]   A. Manthiram, *An outlook on lithium-ion battery technology*, ACS Cent. Sci., 2017, *3*, 1063.

[18]   M. J. Lain, J. Brandon, E. Kendrick, *Design strategies for high power vs. high energy lithium-ion cells*, Batteries, 2019, *5,* 64.

[19]   J. Xie, Y. Lu, *A retrospective on lithium-ion batteries*, Nat. Commun., 2020, *11*, 2499.

[20]   European Comission, *Critical raw materials resilience: Charting a path towards greater security and sustainablity*, URL: https://eur-lex.europa.eu/legal-content/EN/TXT/?uri=CELEX:52020DC0474, Date accessed: 3. Spetember, 2021.

[21]   H. Vikström, S. Davidsson, M. Höök, *Lithium availability and future production outlooks*, Appl. Energy, 2013, *110*, 252.

[22]   J.-M. Tarascon, *Is lithium the new gold?*, Nat. Chem., 2010, *2*, 510.

[23]   S. Jaffe, *Vulnerable links in the lithium-ion battery supply chain*, Joule, 2017, *1*, 225.

[24]   C. Vaalma, D. Buchholz, M. Weil, S. Passerini, *A cost and resource analysis of sodium-ion batteries*, Nat. Rev. Mater., 2018, *3*, 1.

[25]   H. Noh, S. Youn, C. Seung, Y. Sun, *Comparison of the structural and electrochemical properties cathode material for lithium-ion batteries*, J. Power Sources, 2013, *233*, 121.

[26]   A. Colthrope, UAE integrates 648 MWh of sodium sulfur batteries in one swoop, URL: https://www.energy-storage.news/uae-integrates-648mwh-of-sodium-sulfur-batteries-in-one-swoop/, Date accessed: September 3, 2021.

[27]   C. H. Hamann, W. Vielstrich, *Elektrochmie*, ISBN: 3-527-31066-5, Wiley, Weinheim, 2004.

[28]   B. Dunn, H. Kamath, J. Tarascon, *For the Grid : A battery of choices*, Science, 2011, *334*, 928.

[29]   R. Benato, N. Cosciani, G. Crugnola, S. Dambone Sessa, G. Lodi, C. Parmeggiani, M. Todeschini, *Sodium-nickel-chloride battery technology for large-scale stationary storage in the high voltage network*, J. Power Sources, 2015, *293*, 127.

[30]   O. Veneri, C. Capasso, S. Patalano, *Experimental study on the performance of a ZEBRA battery based propulsion system for urban commercial vehicles*, Appl. Energy, 2017, *185*, 2005.

[31]   K. B. Hueso, M. Armand, T. Rojo, *High temperature sodium batteries: Status, challenges and future trends*, Energy Environ. Sci., 2013, *6*, 734.

[32]   R. C. Galloway, *A sodium / beta-alumina / nickel chloride secondary Cell*, J. Electrochem. Soc., 1987, *134*, 256.

[33]   S. Restello, N. Zanon, E. Paolin, *Sodium nickel batteries for telecom hybrid power systems*, INTELEC, Int. Telecommun. Energy Conf., 2013, 324.

[34]   J. L. Sudworth, *The sodium/nickel chloride (ZEBRA) battery*, J. Power Sources, 2001, *100*, 149.

[35]   D. Larcher, J. M. Tarascon, *Towards greener and more sustainable batteries for electrical energy storage*, Nat. Chem., 2015, *7*, 19.

[36]   S. Egloff, *Migros Rietbach setzt auf Ökobatterie: Im Keller der Filiale landet der Solarstrom im Salzspeicher*, Limmattaler Zeitung, 18, 2021.

[37]   S. Ma, M. Jiang, P. Tao, C. Song, J. Wu, J. Wang, T. Deng, W. Shang, *Temperature effect and thermal impact in lithium-ion batteries: A review*, Prog. Nat. Sci. Mater. Int., 2018, *28*, 653.

[38]   Migros, Mirgos Klima Freundliche Filialen, URL: https://www.migros.ch/de/ nachhaltigkeit/klima-energie/unsere-fortschritte/klimafreundliche-filialen.html, Date accessed: September 3, 2021.

[39]   J. T. Kummer, N. Weber, *A sodium-sulfur secondary battery*, SAE Trans., 1968, *76*, 1023.

[40]   R. M. Dell, P. T. Moseley, *Beta-alumina electrolyte for use in sodium/sulphur batteries*, J. Power Sources, 1981, *6*, 143.

[41]   J. Coetzer, M. M. Thackeray, Patent: *Cathode for an electrochemical cell and an electrochemical cell*, US 4288506, 1978.

[42]   J. Coetzer, *A new high energy density battery system*, J. Power Sources, 1986, *18*, 377.

[43]   J. L. Sudworth, *Zebra batteries*, J. Power Sources, 1994, *51*, 105.

[44]   C. H. Dustmann, *ZEBRA battery meets USABC goals*, J. Power Sources, 1998, *72*, 27.

[45]   R. C. Galloway, S. Haslam, *The ZEBRA electric vehicle battery : power and energy improvements*, J. Power Sources, 1999, *80*, 164.

[46]   C. H. Dustmann, *Advances in ZEBRA batteries*, J. Power Sources, 2004, *127*, 85.

[47]   J. St. John, GE scales back production of grid-scale Durathon batteries, URL: https://www.greentechmedia.com/articles/read/ge-scales-back-production-of-grid-scale-durathon-batteries, Date accessed: September 9, 2021.

[48]   K. C. Karthikeyan, General Electric: Battery with 20 years of life and 3500+ CDC cycles – Durathon, URL: https://geekswipe.net/technology/energy/general-electric-battery-with-20-years-html/, Date accessed: September 9, 2021.

[49]   H. Viccaro, GE to end Durathon battery operations in Schenectady, URL: https://dailygazette.com/2015/11/13/ge-end-durathon-battery-operations-schenectady/, Date accessed: September 9, 2021.

[50]   J. O. B. Dr. -Ing. Claus Daniel, *Handbook of Battery Materials*, ISBN: 9783527328697, Wiley-Vch Verlag GmbH & Co KGaA, 2012.

[51]   V. Zinth, J. E. Soc, V. Zinth, S. Seidlmayer, N. Zanon, G. Crugnola, M. Schulz, R. Gilles, M. Hofmann, *In situ spatially resolved neutron diffraction of a sodium-metal-halide battery*, J. Electrochem. Soc., 2015, *162*.

[52]   R. Pollard, J. Newman, *Transport equations for a mixture of two binary molten salts in a porous electrode*, J. Electrochem. Soc., 1971, *126,* 1713.

[53]   R. J. Bones, J. Coetzer, R. C. Galloway, D. A. Teagle, *A sodium / iron (II) chloride cell with a beta alumina electrolyte*, J. Electrochem. Soc., 1987, *134*, 2379.

[54]   G. Li, X. Lu, J. Y. Kim, K. D. Meinhardt, H. J. Chang, N. L. Canfield, V. L. Sprenkle, *Advanced intermediate temperature sodium–nickel chloride batteries with ultra-high energy density*, Nat. Commun., 2016, *7*, 1.

[55]   B. M. Ahn, C. W. Ahn, B. D. Hahn, J. J. Choi, Y. Do Kim, S. K. Lim, K. Jung, Y. C. Park, J. H. Choi, *Easy approach to realize low cost and high cell capacity in sodium nickel-iron chloride battery*, Compos. Part B Eng., 2019, *168*, 442.

[56]   R. Christin, PhD thesis: *Modélisation multiphysique de cellules sodium chlorure de nickel*, Université Grenobles Alpes, 2015.

[57]   K. Frutschy, T. Chatwin, R. Bull, *Cell overcharge testing inside sodium-metal-halide battery*, J. Power Sources, 2015, *291*, 117.

[58]   G. Li, X. Lu, C. A. Coyle, J. Y. Kim, J. P. Lemmon, V. L. Sprenkle, Z. Yang, *Novel ternary molten salt electrolytes for intermediate-temperature sodium/nickel chloride batteries*, J. Power Sources, 2012, *220*, 193.

[59]   G. Li, X. Lu, J. Y. Kim, M. H. Engelhard, J. P. Lemmon, V. L. Sprenkle, *The role of FeS in initial activation and performance degradation of Na-NiCl$_2$ batteries*, J. Power Sources, 2014, *272*, 398.

[60]   X. Lu, G. Li, J. Y. Kim, J. P. Lemmon, V. L. Sprenkle, Z. Yang, *The effects of temperature on the electrochemical performance of sodium-nickel-chloride batteries*, J. Power Sources, 2012, *215*, 288.

[61]   M. M. Gross, S. J. Percival, R. Y. Lee, A. S. Peretti, E. D. Spoerke, L. J. Small, *A high-voltage, low-temperature molten sodium battery enabled by metal halide catholyte chemistry*, Cell Reports Physical Science, 2021, *2*, 100489.

[62]   R. Benato, S. D. Sessa, G. Crugnola, M. Todeschini, N. Zanon, S. Zin, *Sodium-nickel-chloride (Na-NiCl$_2$) battery safety tests for stationary electrochemical energy storage*, *2016 AEIT International Annual Conference*, 2016, pp. 1–5.

[63]   FZSoNick SA, FZSoNick TL range data sheet, URL: https://www.fzsonick.com/applications, Date accessed: September 9, 2021.

[64]   D. Trickett, Report: *Current status of health and safety issues of sodium / metal chloride (ZEBRA) batteries*, 1998, URL: https://www.osti.gov/servlets/purl/7101, Date accessed: 3 Spetember, 2021.

2. Methods

2.1 Development of a modular, high-temperature electrochemical cell

2.1.1 Electrochemical cell

In a first step, a modular, electrochemical cell for high-temperature operation was designed, constructed, tested, and debugged. The cell serves as an experimental platform to determine rate-limiting processes on the negative and positive electrode. The operation of sodium-nickel-chloride cells involves molten and corrosive phases (e.g. sodium and $NaAlCl_4$), which need to be reversibly supplied to the Na-β''-alumina electrolyte interfaces during cycling. Management of the molten phases is further complicated by significant volume changes occurring in the cell, both due to thermal expansion, and due to the electrochemical reactions of the active materials at different state-of-charge.

Thus, requirements for the cell design are:
•   Modular design, enabling alterations to cell configuration and electrode materials
•   Operation at temperatures up to 350 °C
•   Sealing of positive and negative electrode compartments, protection of active components from ambient atmosphere
•   Secure preload of active materials to Na-β''-alumina electrolyte interface
•   Management of liquid phases (liquid sodium and $NaAlCl_4$) during cell operation
•   Homogenous temperature distribution within the cell
•   Online temperature surveillance during operation

The design has to accommodate different cell configurations, allowing operation as symmetric cell with two sodium metal electrodes or as asymmetric cell combining a sodium metal negative electrode with a Ni-$NiCl_2$ positive electrode, with both planar and porous positive electrodes. Further, in asymmetric cell configuration, the planar electrodes should be interchangeable to allow mechanistic studies of nickel and iron de-/chlorination. A central part of the cell assembly are two ceramic α-alumina rings/collars with 20 mm inner diameter and 9 mm height provided by a commercial supplier. α-alumina is an electric and ionic insulator compatible with the corrosive high-temperature environment. With growing demand in cell capacity and therefore in thicker positive electrodes, a new design with 17 mm height of the α-alumina rings/collar was introduced. A sodium-ion-conducting Na-β''-alumina electrolyte disc is sandwiched between the two α-alumina collars, separating the anode from the cathode compartment. Na-β''-alumina discs of thickness 0.3-3 mm with tightly controlled microstructure (grain size, porosity) and sodium content are prepared based on the results of another PhD thesis conducted in our lab.[1] Sintered discs are surface ground at the Empa workshop. For practical lab use, an electrolyte thickness of 1 mm is set

representing a compromise between sodium-ion conductance and sufficient mechanical robustness.

A glass sealing paste developed by FZSonick, which requires sintering at 1010 °C, is employed to glue the two α-alumina collars onto the Na-β''-alumina disc. The assembly is compressed between two stainless steel blind flanges using six M6 bolts, electrically isolated from the steel flanges with ceramic alumina washers to avoid a short-circuit between negative and positive electrode.

Graphite foils with a thickness of 1 mm seal the α-alumina rings to the steel flanges preventing exposure of the active material to the surrounding atmosphere. Cell assembly is performed in an argon-filled glovebox, so the gas space of the cell is filled with argon.

Nickel 201 offers manufacturability and a larger thermal expansion coefficient ($16 \cdot 10^{-6}$ 1/K)[2] than α-alumina ($6.9 \cdot 10^{-6}$ 1/K)[3]. The fitting between the two was set to ISO H9/e8 at 300 °C, which gives the piston a 40 - 125 µm smaller diameter than the α-alumina collar. This allows movement and therefore compensation of volume changes in the electrodes during charge/discharge cycling and sealing of liquid active components. Due to larger thermal expansion coefficients for nickel, this translates to a "less tight" fitting of H8/e8 for manufacturing at 20 °C, which gives the piston an 80 – 146 µm smaller diameter than the α-alumina collar at room temperature. The theoretical fitting calculation was tested on a hot plate to ensure proper movement at 300 °C (figure 2-1).
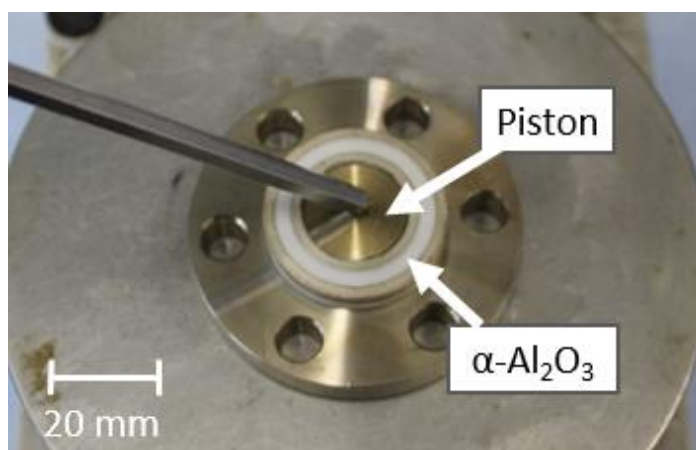
Figure 2-1: Testing movement of nickel piston in α-alumina collar at 300°C on hot plate.

In commercial cells, the Na-β''-alumina is pressed and sintered into the shape of a tube that is closed on the bottom side, which contains the electrode composite consisting of nickel powder, NaCl, and $NaAlCl_4$. This tubular electrolyte design guarantees the contact between composite and the Na-β''-alumina electrolyte during operation. For the planar cell configuration, a spring-loaded nickel piston pushes the cathode composite towards the electrolyte (figure 2-2a). Management of the liquid components of the electrochemical cell turned out to be critical. Leakage of liquid sodium and $NaAlCl_4$ into the spring compartment is further suppressed by a carbon foil filling the gap between the nickel piston and the α-alumina

collar (arrow in figure 2-2b). A nickel wire with a diameter of 1 mm connects the piston electrically to the steel casing with a resistance of 10 mΩ and bypasses the relatively resistive preload spring (160 mΩ). Each casing side contributes 7 mΩ to the overall resistance of the assembly. Glass fiber insulated nickel wires with a resistance of 12 mΩ ensure external electrical connection and are clamped to the outside of the stainless steel casing by M3 bolts. An equivalent circuit of one side of the cell starting with the external nickel cables progressing to Na-β"-alumina electrolyte without active material is shown in figure 2-2c. For reproducible temperature measurements a thermocouple (type K) is inserted in a groove at the interface between α-alumina and Na-β"-alumina. The glass seal between these two components also glues the temperature sensor and keeps it securely in place after tempering. An image of the entire cell comprising with temperature sensor and connection cables is shown in figure 2-2d.
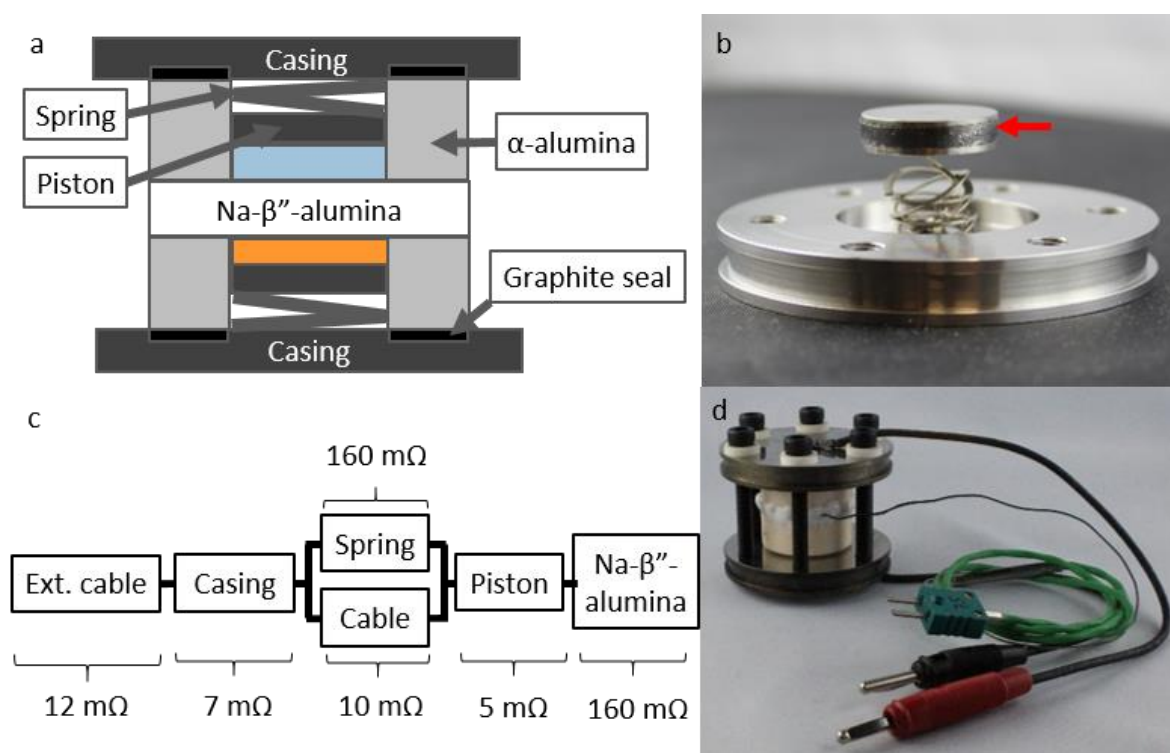
Figure 2-2: a) Drawing of high-temperature electrochemical cell design; b) Cell casing with spring-loaded titanium piston and additional nickel wire electrical connection, the red arrow points to the graphite piston ring; c) Equivalent circuit for one half of the cell including external connection cables and Na-β"-alumina at 300 °C (1mm thick, 20 mm diameter); d) Assembled cell with temperature sensor (green) and connection cables (red: positive electrode, black: negative electrode).

2.1.2 Cell heating

To heat the electrochemical cell up to temperatures of 350 °C a heater jacket was developed in-house as commercially available products were either too bulky or too hot on the outside for operation in an argon-filled glovebox. A resistive heater coil is woven in a up to 30 mm thick glass fiber housing to maintain the temperature distribution of the cell within 10 °C of the operating temperature set point, as shown in figure 2-3. Temperature control is achieved via a feed forward controller with manually adjustable gain.

Figure 2-3: Cell heater made of glass fiber weave with incorporated heater coil.

2.2   Governing equations for electrochemical processes

The governing processes in an electrochemical cell are charge transfer at the interfaces between electrodes and electrolyte(s), and transport of electrons and ionic species in the bulk of these materials. The following section gives a brief overview of the physical description of these processes, their application in experiments, as well as their implementation in multi-physics modelling.

2.2.1 Charge transfer

The Butler-Volmer equation describes the current density as a function of the surface overpotential η_s for charge transfer reactions at the electrode/electrolyte interface[4],[5], shown in equation 1. The surface overpotential is defined as the potential difference between electron conducting phase (φ_1), ion conducting phase (φ_2) and equilibrium potential (E^0). The exchange current density j_0 represents the current exchanged at dynamic equilibrium at the electrode/electrolyte interface when no surface overpotential is applied. The charge transfer coefficients α_a and α_c link the current to the applied surface overpotential for the anodic and cathodic reaction. Ideal, reversible electrochemical reactions feature transfer

coefficients of 0.5 for anodic and cathodic direction. In reality, reversible electrochemical systems exhibit transfer coefficients ranging from 0.4-0.6.[6]

$$j = j_0 \left[exp^{\frac{\alpha_a zF}{RT}\eta_S} - exp^{\frac{-\alpha_c zF}{RT}\eta_S} \right] \qquad \text{Equation 1}^{[4-6]}$$

For sufficiently large surface overpotentials ($|\eta_s| \gg RT/nF$) the current contribution from the counter reaction can be neglected.[6] The Butler-Vollmer equation for the anodic branch simplifies to:

$$j = j_0 \left[exp^{\frac{\alpha_a zF}{RT}\eta_S} \right] \qquad \text{Equation 2}^{[4-6]}$$

Taking the logarithm and solving for the surface overpotential η_s yields the Tafel equation:

$$\eta_S = -\frac{2.3RT}{\alpha_a nF}\lg(j_0) + \frac{2.3RT}{\alpha_a nF}\lg(j) \qquad \text{Equation 3}^{[6]}$$

Solved for $\lg(j)$:

$$\lg(j) = \lg(j_0) + \frac{\alpha_a nF}{2.3RT}\eta_S \qquad \text{Equation 4}^{[6]}$$

The semi-logarithmic representation of the Tafel equation allows an experimental determination of the exchange current density and the transfer coefficients (see figure. 2-4). In a semi-logarithmic plot with current density in logarithmic scale and the surface overpotential in linear scale, the current density increases or decreases linearly for anodic and cathodic branch for sufficiently high surface overpotentials ($|\eta_s| \gg RT/nF$). The current density at the axis intercept with zero surface overpotential represents the exchange current density. The slope of the anodic and cathodic branch determines the transfer coefficients α_a and α_c for the anodic and cathodic reaction respectively.[6]
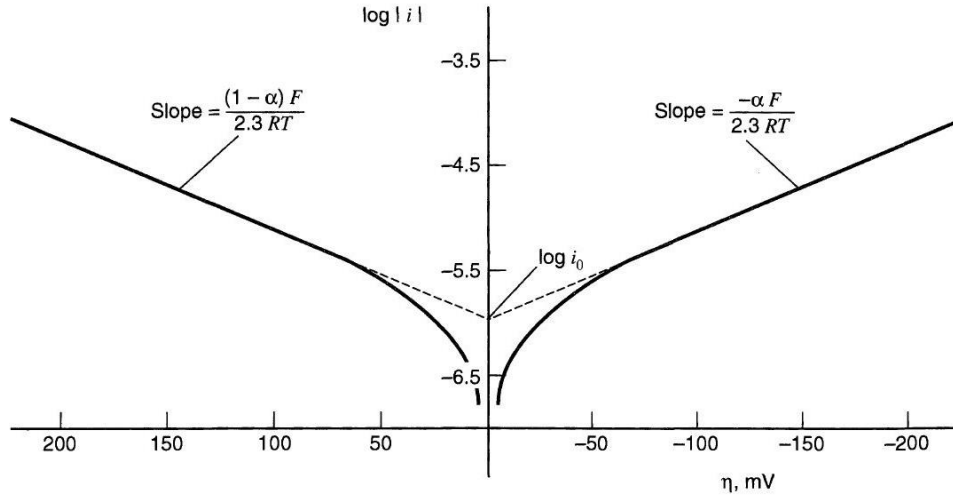
Figure 2-4: Tafel-plot for anodic and cathodic branch of an electrochemical reaction at α_a = α_c = 0.5, T=298 K and an extrapolated exchange current density j_0 = 10^{-6} A/cm², taken with permission from ref. 5.

2.2.2 Species transport

The transport of ionic species in the electrolyte(s) follows the laws of migration, diffusion, and convection[4,5]. The Nernst-Planck equation (5) summarizes the flux in [mol/s cm²] for each ionic species i, here written for one-dimensional mass transfer along the x-axis.

$$N_i(x) = -D_i \frac{\partial c_i(x)}{\partial x} - \frac{z_i F}{RT} D_i c_i \frac{\partial \varphi(x)}{\partial x} + c_i u(x); \qquad \text{Equation 5 [5]}$$

$$u_i = \frac{z_i F D_i}{RT} \qquad \text{Equation 6 [5]}$$

The first term on the right side describes mass transfer by diffusion resulting from a concentration gradient c_i of ionic species i with diffusion constant D_i along the x-axis. The second term on the right side describes mass transfer due to migration induced by the gradient of an electric potential φ. With the Einstein-Smoluchowski[5] relation (equation 6), the migration term can be expressed with the charge number z_i, Faraday constant F, diffusion constant, gas constant R, and temperature T. The last term in equation 5 represents transport of ionic species due to convection forced by the velocity field $u(x)$. The velocity field $u(x)$ is induced by pressure gradients in the fluid, which can be obtained by solving conservation of mass and momentum equations.

The sum of each ionic molar flux multiplied by the charge number z_i and Faraday constant F results in the current density j_{ionic} [mA/cm²] arising from the movement of ionic species, shown in equation 7.

$$j_{ionic}(x) = F \sum_i z_i N_i \qquad\qquad \text{Equation 7}$$

Similar to the Nernst-Planck equation for ionic species, Ohm's law in equation 8 describes the flux of electrons in electronic conductors with conductivity σ as a function of the gradient of the electric potential φ. Here written for one-dimensional current flow along the x-axis.

$$j_{electronic}(x) = -\sigma \frac{\partial \varphi(x)}{\partial x} \qquad\qquad \text{Equation 8 [4]}$$

With equations 5-8, conservation of charge can be described in equation 9:

$$j = \nabla \cdot j_{ionic} = -\nabla \cdot j_{electronic} \qquad\qquad \text{Equation 9 [4]}$$

Mass conservation can be described via a mass balance for a volume element. The change in concentration of species i equals the divergence of molar flux leaving, plus the species produced by the reaction term R_i shown in equation 10:

$$\frac{dc_i}{dt} = -\nabla \cdot N_i + R_i \qquad\qquad \text{Equation 10 [4]}$$

2.3 Battery model of sodium-nickel-chloride batteries

2.3.1 Battery modelling

All physical battery models rely on the fundamental laws of electrochemistry presented in the chapter before, but differ in the way the geometry is taken into account. In 1975, Newman and Tiedemann developed a macroscopic porous electrode theory[7], which treats porous electrodes filled with electrolyte as a superposition of two continua represented by volume averaged quantities. Rather than representing electrolyte and porous electrode with their exact geometric details, the structure is described by porosity, interface area, and effective resistivity over a volume that is small compared to the electrode, but large with respect to the pores. φ_1 and φ_2 represent the local electrical potential in the electron conducting matrix and in the ionic conducting solution phase, respectively. The charge transfer reaction takes place at their interface due to the surface overpotential $\varphi_1 - \varphi_2 - E^0$. Ohm's law describes movement of electrons in the matrix phase, ionic transport in the solution phase is based on the Nernst-Planck equation.

This approach eliminates the need for the exact geometric representation and therefore results in a significant reduction of computational effort. Based on this work, Sudoh and

Newman[8] published a further development of their macroscopic porous electrode model[7], where they applied the concept to a sodium-iron-chloride battery. This chemistry is analogous to the sodium-nickel-chloride battery, with nickel replaced by iron. Their one-dimensional, cylindrical model features a porous iron cathode filled with $NaAlCl_4$ secondary electrolyte, separated from the sodium metal anode by a $Na-\beta''-Al_2O_3$ electrolyte. "Macro-scopic porous electrode theory" is able to predict the concentration profiles of ionic species, the porosity of the electrodes, the reaction rate at the electrode/electrolyte interface, and terminal voltage as function of state of charge.

In 2015, this concept was applied by Christin et al.[9] to model the discharge of a commercial sodium-nickel-chloride battery including nickel and iron in the cathode. Modeling results were in good agreement with the experimental data. Figure 2-5a compares the cell voltage as a function of discharge time derived from model and experiment at a discharge current of 8 A. The presence of nickel and iron in the cathode compartment causes a kink in the discharge curve at 3.5 h discharge time. Figure 2-5b, c show the top-view of the simulated sodium-nickel chloride cell featuring a cloverleaf shaped $Na-\beta''$-alumina electrolyte and centered current collector. The progression of the discharge reaction ($NiCl_2$ + Na $\rightarrow$ NaCl + Ni) in the cathode compartment can be seen in figure 2-5b. The volume fraction of nickel chloride is decreasing towards the current collector and the volume fraction of sodium chloride is increasing accordingly at 50 % state of charge, illustrated in figure 2-5c. The sum of these two volume fractions is not equal to one, as the cathode also contains nickel, iron, iron chloride and $NaAlCl_4$.
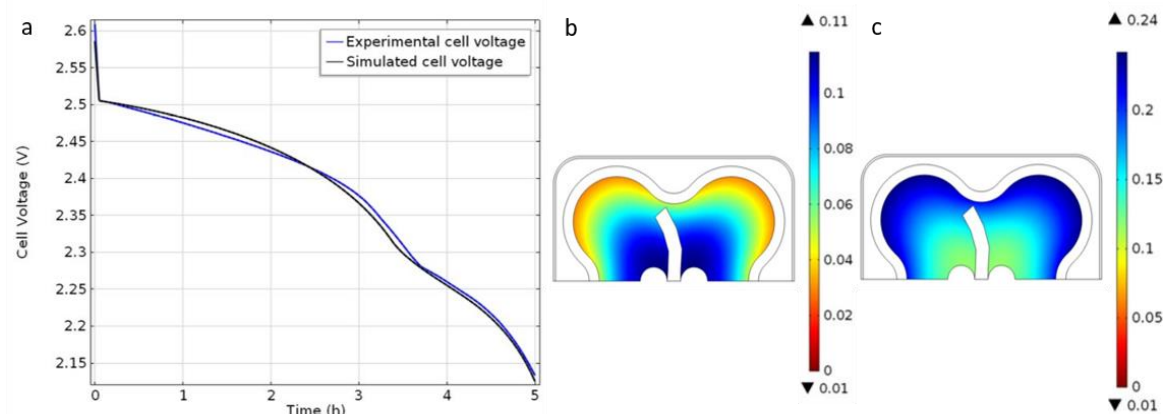
Figure 2-5: a) Modeled and experimental discharge curve at 8 A for a commercial sodium-nickel-chloride battery cell with nickel and iron in the cathode compartment[9]; b) Volume fraction of $NiCl_2$ within the cathode compartment at 50 % state of charge[9]; c) Volume fraction of NaCl within the cathode compartment at 50 % state of charge[9]. Pictures taken with permission from ref. 9.

Modelling results based on the "macroscopic porous electrode theory" not only were in good agreement with experimental data, they also contributed to a better understanding

of the reaction front hypothesis[10-12], describing the inhomogeneous propagation of the charge and discharge reaction in the cathode compartment. The study confirmed that over-potentials in the cathode compartment significantly increase during charge and discharge. This leads to a relocation of the charge transfer reaction to areas, where the reaction proceeds with the lowest possible overpotential. However, due to the approximations made in the "macroscopic porous electrode theory", the study could not provide guidelines on how to modify the cell geometry or the microstructure of the cathode to improve the rate capabilities of sodium-nickel-chloride batteries.

2.3.2 Implementation of multi-physics model for sodium symmetric cell

An example of practical application of the governing equations for electrochemical processes is given in the following section. As a first step towards the development of a complete multi-physics model, a three-dimensional representation of a sodium symmetric cell was implemented using the finite volume method and a commercial COMSOL solver to solve the governing equations. The model consists of a cylindrical Na-β''-alumina electrolyte disc with a thickness of 3 mm coated on both sides with 2 mm metallic sodium sandwiched between two titanium electrodes (see figure 2-6a). A sodium-ion conductivity of 0.2 S/cm at 300 °C was measured for the Na-β''-alumina using electrochemical impedance spectroscopy.[1] For the electronic conductivity of sodium metal and titanium, a value of 10^5 S/cm was assumed.[13] Furthermore, 100% faradaic efficiency leads to mass conservation by Faraday's law (equation 11) and charge conservation requires that the electronic current in the nickel and sodium matches the ionic current in the Na-β''-alumina electrolyte (equation 12).

$$\Delta m_{Na,\ c} = -\Delta m_{Na,a} = \frac{QM}{zF} \qquad \text{Equation 11}$$

$$i_1 = \sigma \, \nabla \cdot \varphi_1 = i_2 = \kappa \, \nabla \cdot \varphi_2 \qquad \text{Equation 12}$$

For operating temperatures between 250 - 300 °C the overpotential for the charge transfer reaction is assumed to be negligible[8], a linearized version of the Butler-Volmer equation was implemented to describe charge transfer at the interface between sodium metal and Na-β''-Al$_2$O$_3$ electrolyte with a symmetric exchange current density set to 5 A/cm^2 and a charge transfer coefficient of 0.5 following ref. 13. As the equilibrium potential (E^0) is equal for both sodium electrodes, it can be cancelled out.

$$j = j_0 \frac{\alpha zF}{RT}(\varphi_1 - \varphi_2) \qquad \text{Equation 13}$$

Additional interfacial resistances, e.g. between sodium metal and the nickel electrode were neglected. The boundary conditions were defined analogously to experiment with one electrode set to ground and the opposite to a current density of ± 32 mA/cm^2.

Figure 2-6b shows the calculated voltage curve of this model with an applied current ± 32 mA/cm^2. At a total overpotential of ± 0.05 V the resulting polarization indicates a significant difference to the measured value of ± 0.08 V. Analysis revealed that the non-negligible resistance contribution of 320 mΩ of the preload spring to the total cell resistance to be responsible for this deviation. This motivated the addition of nickel wire, connecting the piston to the steel flange, for future experiments. This result also justifies the approximation and selected parameter values for the charge transfer kinetics and the neglected interfacial resistances.
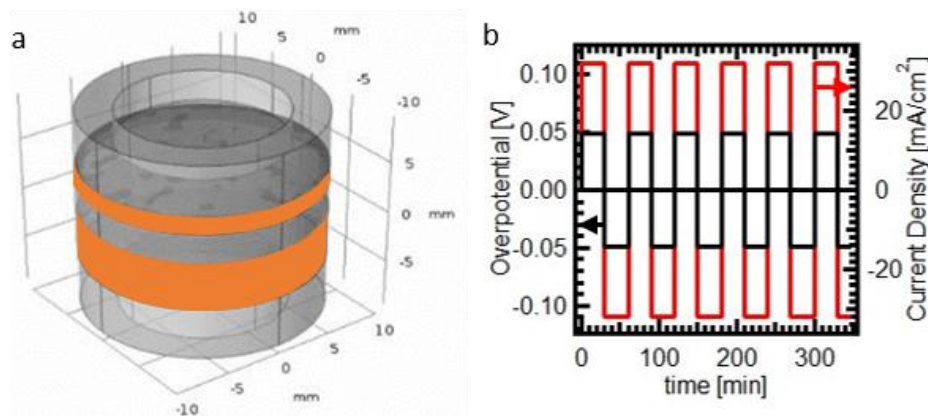
Figure 2-6: a) Multi-physics model of sodium symmetric cell with sodium electrodes in orange; b) Overpotential evolution for simulated symmetric cell at ± 32 mA/cm^2.

2.3.3 Towards a multi-physics model of the positive electrode composite

Before the multi-physics cell model can be expanded to include the exact representation of the positive electrode of the sodium-nickel-chloride battery, the relevant species and processes of the de-/chlorination reaction of nickel (and iron) in NaAlCl$_4$ at 300 °C need to be identified, and the corresponding kinetic parameters need to be assessed. Consequentially, the de-/chlorination reaction of nickel and iron with dedicated experiments had to be studied first. The results are discussed in detail in chapter 4, where the rate-limiting processes are quantified and ascribed to the prevailing transport mechanism. The discovered de-/chlorination mechanisms of nickel and iron, described in chapter 4 and are of pivotal importance for the development of a high-fidelity multi-physics battery model.

2.4 Electrochemical measurements

In order to investigate and characterize the negative and positive electrode of sodium-nickel-chloride batteries in the self-built high-temperature electrochemical cell, different electrochemical measurements and methods were applied. The following chapter gives a brief overview of these techniques as applied in chapters 3, 4, and 5.

2.4.1 Galvanostatic methods

In galvanostatic methods, a constant current is applied to an electrochemical system between working electrode (WE) and counter electrode (CE). The electrochemical cell has to provide the corresponding charge per unit time in order to maintain charge neutrality over the entire system considered. An applied current leads to a change in cell voltage and creates characteristic voltage traces for the probed system. Galvanostatic methods are therefore used to record the characteristic voltage behavior of an electrode for instance as function of current, state-of-charge, temperature or time. Galvanostats usually control the current applied via an external resistance. As the voltage of the electrochemical cell changes, that external resistance has to be adjusted and controlled in order to allow the current to be constant over time.

This method is exemplarily applied to probe the dendrite susceptibility of an electrolyte.[14] Dendrites are pointy, metallic deposits provoked by inhomogeneous electrochemical reduction (e.g. plating) of metal ions.[15–17] The critical current density (CCD) is the current density at which a dendrite penetrates the electrolyte, leading to an electronic short circuit in the electrochemical cell.[18] It is determined by a stepwise increase of constant current cycles until the cell voltage breaks down and an electronic short circuit established by dendrites. This method has been applied to study the dendrite susceptibility of the liquid sodium/Na-β"-alumina interface in chapter 3.[19]

For battery applications, galvanostatic methods are often used to measure the rate-capability of an electrode. In rate tests, the probed electrode is charged and discharged with constant current (CC). The amount of capacity retrieved during discharge at a given current represents the rate-capability and allows comparison to other electrodes. This method has been applied in chapter 4 and 5 to determine and compare the rate-capability of Ni-$NiCl_2$ and Fe-$FeCl_2$ electrodes.

For battery cycling, galvanostatic dis-/change is often combined with potentiostatic measurements, where cell voltage is kept constant at the end of dis-/charge cycles until a cut-off current is reached.

2.4.2 Voltammetric methods

Contrary to galvanostatic methods, voltammetric methods apply a potential difference between WE and CE to trigger a current response from an electrochemical system. The electrochemical cell has to provide the corresponding current in order to maintain the externally applied cell voltage. In linear sweep voltammetry, cell voltage is swept between a lower, upper boundary voltage (E_λ) and back at a constant scan rate, as shown in figure 2-7 (left). This external voltage stimulus triggers a dynamic current response, which allows investigation of different electrochemical processes inside the cell (figure 2-7, right).
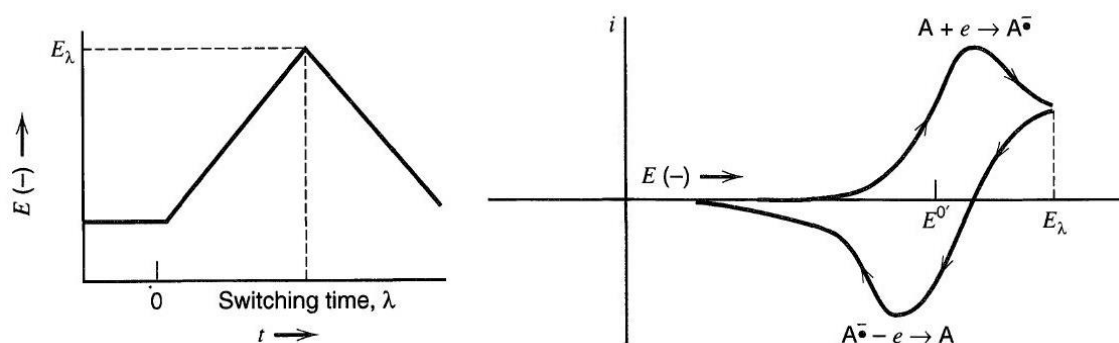
Figure 2-7: Linear sweep voltammetry with forced cell voltage evolution over time (left) and current response from the electrochemical system (right), taken with permission from ref. 5.

Cyclic voltammetry is a powerful method that can approximate the reversible potential (E^0) and assess the reversibility of an electrochemical reaction by comparison of the forward (oxidation) and backwards scan (reduction). The voltage traces can also be used to identify multiple sub-reaction steps, hinted by additional kinks and plateaus within a single oxidation or reduction reaction. After an oxidation or reduction process is triggered by exceeding the reversible potential (E^0), the current increases/decreases exponentially following the Butler-Volmer relation (equation 1). Further polarization leads to a linear current increase. This region is dominated by species transport and is described by Nernst-Planck relation (equation 5) for ionic species as well as by Ohm's law (equation 8) for electron conduction. Upon further polarization, the electrochemical system experiences current saturation (peaks in figure 2-7, right). At this point, the concentration of electrochemically active ionic species is completely depleted at the electrode interface, and every reactant is immediately consumed by the electrochemical reaction. However, oxidation continues at reduced currents above the peak potential, as electrochemically active ions are still present in the bulk of the electrolyte. The established concentration gradient leads to the limited flux of ionic species due to diffusion. This phenomenon can be described analytically via the solution of Fick's 2nd law with corresponding boundary conditions, here written for one-dimensional transport of species i along the x-axis.[5,20,21] The solution (equation 37) yields a relation

between current, diffusion constant and time. The derivation shown here follows the notation of Nicholson and Shain.[21]

Reversible reduction of oxidized species O to a reduced species R:

$$O + ne^- \leftrightarrow R \qquad \text{Equation 14 [21]}$$

Fick's 2nd law for oxidized species O:
$$\frac{\partial C_O}{\partial t} = D_O \frac{d^2 C_O}{\partial x^2} \qquad \text{Equation 15 [21]}$$

And for reduced species R:
$$\frac{\partial C_R}{\partial t} = D_R \frac{d^2 C_R}{\partial x^2} \qquad \text{Equation 16 [21]}$$

Boundary conditions:
$$t = 0, \ x \geq 0: \quad C_O = C_O^*; \ C_R = C_R^* \qquad \text{Equation 17 [21]}$$

$$t \geq 0, x \to \infty: \quad C_O \to C_O^*; \ C_R \to 0 \qquad \text{Equation 18 [21]}$$

$$t > 0, \ x = \infty:$$

$$D_O \frac{\partial C_O}{\partial x} = -D_R \frac{\partial C_R}{\partial x} \qquad \text{Equation 19 [21]}$$

$$\frac{C_O}{C_R} = exp^{(\frac{nF}{RT}(E - E^O))} \qquad \text{Equation 20 [21]}$$

With C_O, C_R being the concentration of species O and R [M]; D_O, D_R is the diffusion constant of species O and R [cm²/s]; t is time [s] and x [cm] is the length of the diffusion path. C_O^*, C_R^* are the bulk concentrations away from the electrode [mol/cm³]. n [-] is the number of electrons involved in the redox reaction.

$$0 < t \leq \lambda: E = E_i - vt \qquad \text{Equation 21 [21]}$$

$$0 \leq t: E = E_i - 2v\lambda + vt \qquad \text{Equation 22 [21]}$$

E is the potential of the electrode and E_i is the initial potential of the electrode at the beginning of the scan. v represents the scan rate and λ is the time at the upper voltage boundary of the scan. Re-arrangement yields:

$$\frac{C_O}{C_R} = \theta S_\lambda(t) \qquad \text{Equation 23 [21]}$$

With:

$$\theta = exp^{(\frac{nF}{RT}(E-E^0))}$$

Equation 24 [21]

$$S_\lambda(t) = \begin{cases} exp^{-at} & for\ t \leq \lambda \\ exp^{at-2a\lambda} & for\ t \geq \lambda \end{cases}$$

Equation 25 [21]

$$a = \frac{nFv}{RT}$$

Equation 26 [21]

For $t < \lambda$, equation 20 can be further simplified to:

$$\frac{c_O}{c_R} = \theta exp^{-at}$$

Equation 27 [21]

Laplace transformation of the equations 15-18 yields:

$$C_O(0,t) = C_O^* - \frac{1}{\sqrt{\pi D_O}} \int_0^t \frac{f(\tau)\partial\tau}{\sqrt{t-\tau}}$$

Equation 28 [21]

$$C_R(0,t) = \frac{1}{\sqrt{\pi D_R}} \int_0^t \frac{f(\tau)\partial\tau}{\sqrt{t-\tau}}$$

Equation 29 [21]

$$f(t) = D_O \left(\frac{\partial c_O}{\partial x}\right)_{x=0} = \frac{i}{nFA}$$

Equation 30 [21]

Combination of equation 23 with 28 and 29 results in:

$$\int_0^t \frac{f(\tau)\partial\tau}{\sqrt{t-\tau}} = \frac{C_O^*\sqrt{\pi D_O}}{1+\gamma\theta S_\lambda(t)}; \qquad \gamma = \sqrt{\frac{D_O}{D_R}}$$

Equation 31 [21]

As a relation of current and time is of interest equation 30 can be written as:

$$\int_0^{at} \frac{g(z)\partial z}{\sqrt{a}\sqrt{at-z}}; \qquad \tau = \frac{z}{a}; \quad f(t) = g(at)$$

Equation 32 [21]

To obtain a dimensionless expression of equation 32:

$$g(at) = C_O^*\sqrt{\pi D_O a}\ \chi(at)$$

Equation 33 [21]

$$\int_0^{at} \frac{\chi(at)\ \partial z}{\sqrt{at-z}} = \frac{1}{1+\gamma\theta S_{a\lambda}(at)}$$

Equation 34 [21]

From equations 20 and 23 yield the relation to the potential:

$$E = E^0 - \frac{RT}{nF}\ln(\gamma) + \frac{RT}{nF}\left(\ln(\gamma\theta) + \ln(S_{a\lambda}(at))\right)$$ Equation 35 [21]

$$E_{1/2} = E^0 + \frac{RT}{nF}\ln\left(\sqrt{\frac{D_R}{D_O}}\right)$$ Equation 36 [21]

Finally, combination of 30, 32, 33 gives the relation of current vs. concentration and diffusion coefficient and time:

$$i = nFAC_O^*\sqrt{\pi D_O a}\,\chi(at)$$ Equation 37 [21]

Solution of equation 33 provides a set of values of $\Pi^{0.5}{\cdot}\chi(at)$ as function of at or $n(E\text{-}E_{1/2})$, which are summarized in table 2-1. The results have been obtained numerically by summation series or numerical integral solution.[21–26]

$\dfrac{n(E - E_{1/2})}{RT/F}$	$n(E - E_{1/2})$ mV at 25°C	$\pi^{1/2}\chi(\sigma t)$	$\phi(\sigma t)$	$\dfrac{n(E - E_{1/2})}{RT/F}$	$n(E - E_{1/2})$ mV at 25°C	$\pi^{1/2}\chi(\sigma t)$	$\phi(\sigma t)$
4.67	120	0.009	0.008	−0.19	−5	0.400	0.548
3.89	100	0.020	0.019	−0.39	−10	0.418	0.596
3.11	80	0.042	0.041	−0.58	−15	0.432	0.641
2.34	60	0.084	0.087	−0.78	−20	0.441	0.685
1.95	50	0.117	0.124	−0.97	−25	0.445	0.725
1.75	45	0.138	0.146	−1.109	−28.50	0.4463	0.7516
1.56	40	0.160	0.173	−1.17	−30	0.446	0.763
1.36	35	0.185	0.208	−1.36	−35	0.443	0.796
1.17	30	0.211	0.236	−1.56	−40	0.438	0.826
0.97	25	0.240	0.273	−1.95	−50	0.421	0.875
0.78	20	0.269	0.314	−2.34	−60	0.399	0.912
0.58	15	0.298	0.357	−3.11	−80	0.353	0.957
0.39	10	0.328	0.403	−3.89	−100	0.312	0.980
0.19	5	0.355	0.451	−4.67	−120	0.280	0.991
0.00	0	0.380	0.499	−5.84	−150	0.245	0.997

Table 2-1: Numerical solution of equation 33 for different values of $\Pi^{0.5}{\cdot}\chi(at)$ as a function of at or n(E-E$_{1/2}$), table taken with permission from ref. 5.

During linear sweep voltammetry the condition for peak current (i_p) is met when the function $\Pi^{0.5}{\cdot}\chi(at)$ reaches its maximum at 0.4463. Therefore, equation 37 can be rewritten, substituting $\Pi^{0.5}{\cdot}\chi(at)$ with the numerical value 0.4463 and with help of equation 26. This special representation is also called Radles-Sevcik equation (38). It is of special relevance, as it allows the derivation of the diffusion constant of active species, D_O when bulk concentration, C_O^*, surface area A and scan rate, υ is known. This relation has been used in chapter

4 to characterize the rate-limiting diffusion process in Ni-NiCl$_2$ and Fe-FeCl$_2$ electrodes upon oxidation and reduction.

Radles-Sevcik equation: $$i_p = 0.4463 nFAC_O^* \sqrt{D_O \frac{nFv}{RT}}$$ Equation 38 [5]

References

[1]   M. Bay, M. V. F. Heinz, R. Figi, C. Schreiner, D. Basso, N. Zanon, U. F. Vogt, C. Battaglia, *Impact of liquid phase formation on microstructure and conductivity of Li-stabilized Na-β"-alumina Ccramics*, ACS Appl. Energy Mater., 2018, *2*, 687.

[2]   F. C. Nix, D. MacNair, *The thermal expansion of pure metals: Copper, gold, aluminum, nickel, and iron*, Phys. Rev., 1941, *60*, 597.

[3]   W. J. Campbell, C. Grain, *Thermal expansion of alpha-alumina*, Adv. X-ray Anal., 1961, *5*, 244.

[4]   J. Newman, K. E. Thomas-Alyea, *Electrochemical systems*, ISBN: 0-471-47756-7, John Wiley & Sons, Inc, 2004.

[5]   L. R. Faulkner, A. J. Bard, *Electrochemical methods fundamentals and applications*, ISBN: 0-471-04372-9, Wiley, 2001.

[6]   C. H. Hamann, W. Vielstrich, *Elektrochmie*, ISBN: 3-527-31066-5, Wiley, Weinheim, 2004.

[7]   J. Newman, W. Tiedemann, *Porous-electrode theory with battery applications*, AIChE J., 1975, *21*, 25.

[8]   M. Sudoh, J. Newman, *Mathematical modeling of the sodium/iron chloride battery*, J. Electrochem. Soc., 1990, *137*, 876.

[9]   R. Christin, M. Cugnet, N. Zanon, G. Crugnola, P. Mailley, *Multi-physics modeling of a Na-NiCl2 commercial cell*, ECS Trans., 2015, *66*, 3.

[10]   J. L. Sudworth, *The sodium/nickel chloride (ZEBRA) battery*, J. Power Sources, 2001, *100*, 149.

[11]   J. Rijssenbeek, H. Wiegman, D. Hall, C. Chuah, G. Balasubramanian, C. Brady, *Sodium-metal-halide batteries in diesel-battery hybrid telecom applications*, INTELEC, Int. Telecommun. Energy Conf., 2011.

[12]   C. Kortenbruck, R. Gilles, A. Senyshyn, V. Zinth, M. Hofmann, C. von Lüders, O. Dolotko, M. Mühlbauer, S. Seidlmayer, N. Paul, *Battery research as progress pacemaker*, Neutron News, 2015, *26*, 29.

[13]   R. Christin, PhD thesis: Modélisation multiphysique de cellules sodium chlorure de nickel, Université Grenobles Alpes, 2015.

[14]   M. C. Bay, M. Wang, R. Grissa, M. V. F. Heinz, J. Sakamoto, C. Battaglia, *Sodium plating from Na-β"-alumina ceramics at room temperature, paving the way for fast-charging all-solid-state batteries*, Adv. Energy Mater., 2020, *10*, 201902889.

[15]   L. Fan, S. Wei, S. Li, Q. Li, Y. Lu, *Recent progress of the solid-state electrolytes for high-energy metal-based batteries*, Adv. Energy Mater., 2018, *8*, 1.

[16]   B. Liu, J. G. Zhang, W. Xu, *Advancing lithium metal batteries*, 2018, *2*, 833.

[17]   Y. Guo, H. Li, T. Zhai, *Reviving lithium-metal anodes for next-generation high-energy batteries*, Adv. Mater., 2017, *29*, 1.

[18] A. Sharafi, H. M. Meyer, J. Nanda, J. Wolfenstine, J. Sakamoto, *Characterizing the Li-Li$_7$La$_3$Zr$_2$O$_{12}$ interface stability and kinetics as a function of temperature and current density*, J. Power Sources, 2016, *302*, 135.

[19] D. Landmann, G. Graeber, S. Haussener, C. Battaglia, *Sodium plating and stripping from Na-β''-alumina ceramics beyond 1000 mA/cm^2*, Mater. Today Energy, 2020, *18,* 100515.

[20] J. E. B. Randles, *A cathode ray polarograph. Part II: The current-voltage curves*, Trans. Faraday Soc., 1948, *44*, 327.

[21] R. S. Nicholson, I. Shain, *Correction: Theory of stationary electrode polarography: Single scan and cyclic methods applied to reversible, irreversible, and kinetic systems*, Anal. Chem., 1964, *36*, 706.

[22] A. Sevcik, *Oscillographic polarography with periodical triangular voltage*, Collect. Czech. Chem. Commun., 1948, *13*, 349.

[23] W. H. Reinmuth, *Nernst-controlled currents in hanging-drop polarography*, J. Am. Chem. Soc., 1957, *79*, 6358.

[24] H. Matsuda, Y. Ayabe, *Zur Theorie der Randles-Sevcikschen Kathodenstrahl-Polarographie*, Zeitschrift für Elektrochemie, 1955, *59*, 494.

[25] J. C. Myland, K. B. Oldham, *An analytical expression for the current-voltage relationship during reversible cyclic voltammetry*, J. Electroanal. Chem., 1983, *153*, 43.

[26] A. C. Ramamurthy, S. K. Rangarajan, *A gaussian quadrature analysis of linear sweep voltammetry*, Electrochim. Acta, 1981, *26*, 111.

3. Sodium plating and stripping from Na-β"-alumina ceramics beyond 1000 mA/cm² *

*The following chapter has been published as a journal article: Daniel Landmann, Gustav Graeber, Meike V. F. Heinz, Sophia Haussener, Corsin Battaglia, Sodium plating and stripping from Na-β"-alumina ceramics beyond 1000 mA/cm², Materials Today Energy, 2020, 18, 100515.

In this study, we assess the rate capability of the liquid sodium electrode as deployed in sodium-nickel-chloride batteries. The home-built electrochemical cell is here equipped with two sodium electrodes in symmetric cell configuration. This setup allows the determination of achievable stripping and plating currents for different porous carbon coatings and operating temperatures.

Author contributions

D.L. conceived the idea for this study and designed the experiments together with M.H. and C.B. D.L. designed the electrochemical cell and performed the experiments in an argon filled glovebox with liquid sodium electrodes in symmetric configuration. D.L. analyzed the data, prepared the figures, and wrote the manuscript. G.G. edited the videos. G.G., M.H., S.H., and C.B. critically reviewed and edited the manuscript. All coauthors read, commented, and approved the final manuscript.

Abstract

Dendrite formation limits the cycle life of lithium and sodium metal anodes and remains a major challenge for their integration into next-generation batteries, even when replacing the liquid electrolyte by a solid electrolyte. Voids forming in solid metal anodes at the interface to a solid electrolyte upon stripping cause current constrictions upon plating and promote dendrite formation. Recent studies showed that alkali metal creep is the primary mechanism for replenishing the voids at room temperature. Here we investigate plating and stripping of liquid sodium metal from a carbon-coated ceramic Na-β"-alumina electrolyte at 250 °C, thereby eliminating creep-related mass transport limitations. We demonstrate extremely high current densities of up to 2600 mA/cm^2 and cumulative plating capacities of >10 Ah/cm^2 at 1000 mA/cm^2 without dendrite formation. Our results demonstrate that liquid metal anodes can be paired with solid electrolytes, providing a practical solution to suppress dendrite formation at high current densities.

3.1 Introduction

Lithium and sodium metal anodes are considered the 'holy grail' for lithium and sodium batteries, as they provide the lowest chemical potential and high volumetric capacity (-3.04 V vs SHE and 2062 mAh/cm^3 for lithium and -2.71 V vs SHE and 1129 mAh/cm^3 for sodium at room temperature).[1–5] However, the realisation of reversible plating and stripping without dendrite formation over many cycles remains a major challenge for both liquid and solid electrolytes.[6,7] The US Department of Energy currently sets the fast charging goal for lithium metal anodes at a cumulatively cycled capacity of 10 Ah/cm^2 at a cycling rate of 10 mA/cm^2, ideally with no excess of (non-cycled) lithium in the cell.[8] So far, most studies have focused on plating and stripping at room temperature.

Much progress has been made in recent years in controlling the interface between lithium and sodium metal anodes and the electrolyte. In particular, it was shown that the critical current density for dendrite formation with solid electrolytes scales with interfacial resistance.[9–11] The latter can be reduced by thermal treatment of the electrolyte surface or by applying interfacial coatings.[12–19] However, even when the interfacial resistance becomes negligible ($<10\ \Omega cm^2$), it is not yet possible to sustain a cycling rate of 10 mA/cm^2 over an extended period without dendrite formation. Some of us recently compared plating and stripping of lithium vs sodium metal below their melting temperature from ceramic electrolytes under otherwise identical experimental conditions and observed that the critical current density for sodium is about one order of magnitude higher than for lithium, leading to the hypothesis that the mechanical properties of lithium and sodium are governing dendrite formation.[10] Based on the pressure dependence of stripping, Ref. 20, 21 concluded that lithium and sodium metal creep (or cold flow) behavior rather than lithium and sodium diffusion is the primary mechanism for replenishing the voids forming in lithium and sodium metal anodes at the interface to the solid electrolyte interface upon stripping. Avoiding the formation of such voids during stripping is key to suppress dendrite formation during plating.

To circumvent creep-related mass transport limitations, we investigate plating and stripping of sodium above its melting temperature from the archetypical Na-β''-alumina solid electrolyte. Carbon coatings are applied to prevent dewetting of liquid sodium from the sodiophobic Na-β''-alumina surface. We demonstrate that plating and stripping is possible at extremely high current densities of 2600 mA/cm^2 and cumulative plated capacities of 10 Ah/cm^2 at 250 °C without dendrite formation. Thus, employing a liquid sodium metal anode as in commercial sodium-sulfur (NaS) and sodium-nickel-chloride (Na-NiCl$_2$) batteries is very effective in preventing dendrite formation. Furthermore, we perform open-cell experiments to assess the amount of sodium stored within the porous carbon coating and determine the retrievable amount of sodium during stripping. We show that these coatings efficiently supply sodium to the Na-β''-alumina surface, minimizing the excess of active material in the electrode. We further characterize how coating thickness and operating temperature affect the rate performance of the liquid sodium metal anode.

3.2 Results and discussion
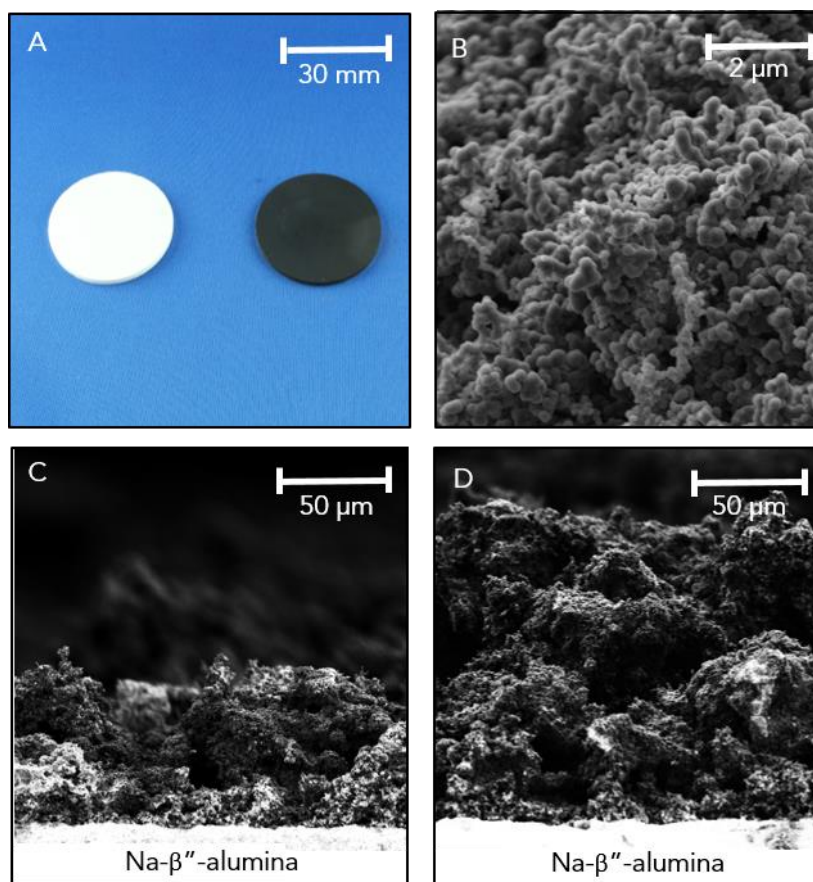
Figure 3-1: Materials A) Photograph of sintered Na-β''-alumina disks without (left) and with (right) sprayed porous carbon coating. B) Magnified SEM image of the porous structure of the coating with primary carbon particles. C) and D) Cross-sectional SEM images of the porous carbon coatings onto Na-β ''-alumina disks with 50 and 200 μm thickness, respectively.

Figure 3-1A shows an uncoated (left) and a carbon-coated (right) Na-β''-alumina electrolyte disk. The carbon coating serves three functions: (1) it acts as a porous electrode that contacts the electrolyte in the absence of sodium, (2) it prevents dewetting of liquid sodium from the sodiophobic Na-β''-alumina surface, and (3) it stores and supplies liquid sodium in and from its pores during cell operation at elevated temperatures. Such coatings are also employed in high temperature Na-NiCl$_2$ batteries to ensure sodium coverage of the entire electrolyte area at all state-of-charge.[22] Cross-sectional scanning electron microscopy (SEM) images of the carbon coating reveal a porous structure, comprising carbon particles with a typical size of 0.1 μm (figure 3-1B). Depending on the number of spray passages applied, average coating thicknesses of approximately 50 and 200 μm with a relative thickness variation of ± 15% were obtained (figure 3-1C and D). From the weight difference before and after coating application, the film thickness from SEM images, and assuming a bulk

density of 2.5 g/cm^3 (40 wt% carbon, 60 wt% sodium hexametaphosphate), a coating po-
rosity of ~80% is deduced.
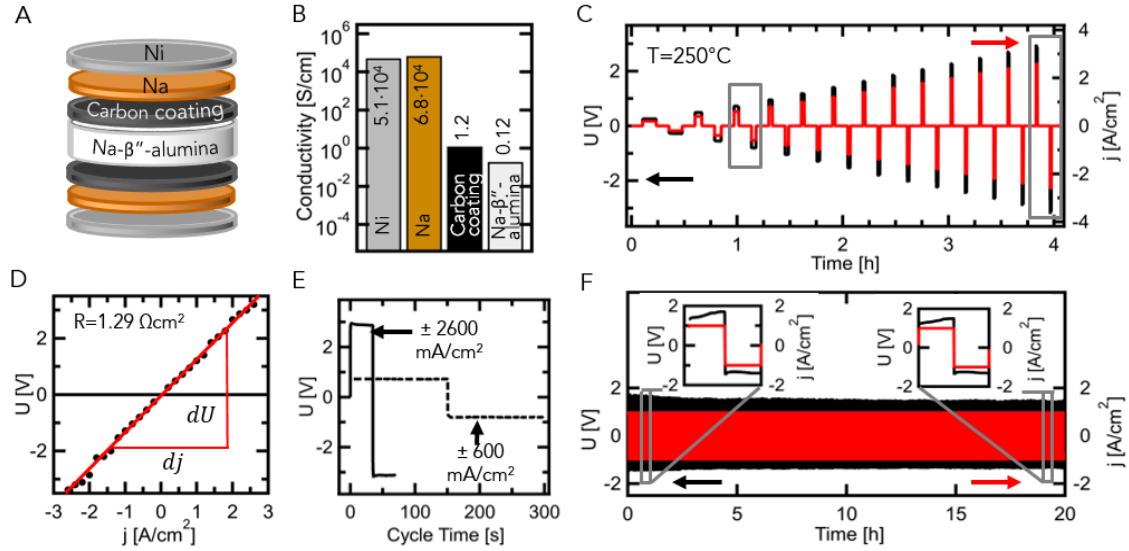
Figure 3-2: Symmetric cell results at 250 °C with 50 µm thick carbon coatings. A) Schematic of the symmetric cell. B) Electronic conductivity of nickel, liquid sodium, and carbon coatings compared to the ionic conductivity of Na-β''-alumina at 250 °C. C) Plating/stripping cycles with stepwise increase (200 mA/cm^2) of applied current density j (red line) up to 2600 mA/cm^2, and corresponding voltage U response of the cell (black line). D) Corresponding cell voltage U as a function of current density j, showing a linear relationship and constant cell resistance of 1.29 Ωcm^2. E) Magnified view of plating/ stripping cycles at 2600 and 600 mA/cm^2, respectively. F) Cumulative plating of 10 Ah/cm^2 at 1000 mA/cm^2 (400 cycles).

A schematic of the symmetrical cell design is shown in figure 3-2A and figure 3-7. The cell consists of the carbon-coated Na-β''-alumina solid electrolyte disk, sandwiched between two sodium foils and cylindrical nickel current collectors. Figure 3-2B compares the electronic and ionic conductivity of the cell components at 250 °C. The electronic conductivity of the carbon coating of 1.2 S/cm is only one order of magnitude higher than the ionic conductivity of the Na-β''-alumina electrolyte (0.12 S/cm, Ref. 26), while the conductivity of liquid sodium and the nickel current collector are four to five orders of magnitude higher.[24,25] While the cell components (figure 3-2A) are generally coupled in series, the conductivity of the carbon coating is only of relevance in the absence of sodium. When liquid sodium starts to fill its pores upon plating, the internal resistance of the cell is dominated by the resistance of the Na-β''-alumina electrolyte and passive cell components.

We first cycled the cell galvanostatically at a temperature of 250 °C, transferring 25 mAh/cm^2 per half cycle. The current density was increased stepwise from 200 mA/cm^2 to 2600 mA/cm^2 for each plating/stripping cycle (figure 3-2C). Due to the fast charge transfer

kinetics at the interface between the Na-β''-alumina electrolyte and the sodium metal electrodes, the voltage in figure 3-2*Figure 3-2*D remains linearly dependent on the current density up to the highest value of 2600 mA/cm^2. This exceeds practical current densities for batteries by at least one order of magnitude (e.g. in a Na-NiCl$_2$ cell with 40 Ah and 200 cm^2 electrolyte area, the current density during 1C pulse operation reaches 200 mA/cm^2 (ref. 27), for lithium-ion batteries the current density rarely exceeds 10 mA/cm^2).[8] Using Ohm's law, we extract a cell resistance of 1.3 Ωcm^2. Taking into account the ionic conductivity of the Na-β''-alumina electrolyte (figure 3-2B), it contributes about 0.8 Ωcm^2, while the remaining contribution stems mainly from the connectors and connection cables. Information on cell impedance evolution after cell assembly and cycling can be found in figure 3-8A (supporting information). Note that high current densities of e.g. 2600 mA/cm^2 generate a considerable amount of Joule heating (56 W per cm^3 of electrolyte). Consequently, the cell temperature was stabilized for each measurement to 250 °C to ensure that the cell resistance can be extracted from figure 3-2D. Stabilizing the cell thermally at even higher current densities was increasingly difficult. Nevertheless, the cycling data (figure 3-2C) indicates no signs of dendrite formation or short circuits, even at current densities of 2600 mA/cm^2. Figure 3-2E shows a magnified view of the cycle at 2600 mA/cm^2. At such high current density, we initially observe a slight increase in cell voltage, which then stabilizes after the first 5 seconds (figure 3-2E, solid line). For current densities of 600 mA/cm^2 and lower (figure 3-2E, dashed line), the voltage stabilizes immediately.

Figure 3-2F shows 400 consecutive plating/stripping cycles at 1000 mA/cm^2, transferring 25 mAh/cm^2 per half cycle at a temperature of 250 °C (20 h). The cumulative amount of sodium plated at each electrode amounts to 10 Ah/cm^2. The insets of figure 3-2F show single cycles after 1 h and 19 h of plating/stripping. Both cell voltage traces show a slight increase during the half cycle at positive currents, indicating a slight change in active electrode area. This behavior is not seen for half cycles at negative currents. We ascribe this to insufficient sodium supply upon stripping from the top-side compartment, caused by sodium loss within the cell (e.g. squeezed out behind the nickel current collector). While managing the substantial volume changes of the sodium anode in our test cell is challenging, technical solutions based on metal shims are available in commercial Na-NiCl$_2$ batteries.[22] The entire cycling of the symmetric cell over 1400 cycles, including run-in cycles and end of life (due to voltage limitations) is shown in figure 3-8B (supporting information).

The evolution of galvanostatic overpotential traces during plating and stripping in symmetric cells was discussed in detail in ref. 28 for solid lithium metal electrodes operated near room temperature, which are prone to dendrite formation at current densities on the order of 10 mA/cm^2. Cells with solid lithium (and sodium) metal electrodes tend to exhibit a much more pronounced "peaking" behavior at the start of each half cycle, which was associated with the initial activation barrier for nucleation on the cathode.[28–32] However, we do not observe such behavior for liquid sodium electrodes with graphite coating, indicating that

dendrite formation does not play a role, even at current densities of 2600 mA/cm^2 or cumulative plating capacities of 10 Ah/cm^2.
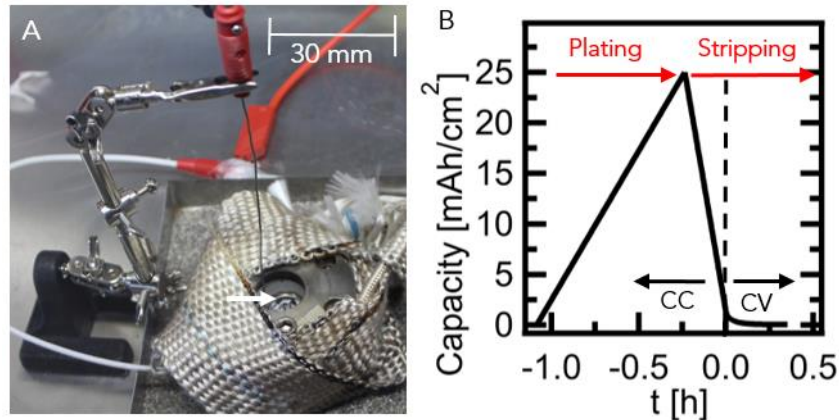
Figure 3-3: Open cell set up A) Photograph of the open cell providing optical access to the top-side carbon coating. B) Plating and stripping cycle applied to all open cell experiments: 25 mAh/cm^2 plated at 30 mA/cm^2, followed by CC stripping varying from 10 to 600 mA/cm^2 and subsequent CV soaking step at 2.5 V (dotted line).

To investigate sodium filling into and extraction from the porous carbon coating in more detail, we employed an open cell design with optical access to the top-side carbon coating (figure 3-3A*Figure 3-3*, white arrow). A nickel ring electrode replaced the top-side cylindrical current collector and the top-side sodium foil was eliminated to allow visual access by a camera. Due to the high conductivity of the porous carbon coating of 1.2 S/cm at 250 °C (figure 3-3B), the current distribution remains relatively uniform across the surface, especially once the pores are filled with liquid sodium metal. Thermography on the open cell was conducted to confirm accurate temperature readings of the build-in thermocouple and even temperature distribution across the entire electrolyte surface in the open configuration (figure 3-9). Figure 3-3B illustrates the cycling protocol applied to the open cells. At the beginning of each cycle, the top-side carbon coating is filled by plating 25 mAh/cm^2 of liquid sodium, corresponding to a nominal (dense) liquid sodium metal thickness of 242 µm, taking into account the volumetric capacity of liquid sodium metal of 1035 mAh/cm^3 at 250 °C.[33] Plating is performed at a current density of 30 mA/cm^2. Sodium extraction from the carbon coating is evaluated at constant current (CC) densities (10 mA/cm^2 to 600 mA/cm^2) until a cell potential of 2.5 V is reached. Subsequently, the cell is soaked at constant voltage (CV) of 2.5 V until the current density falls below 0.1 mA/cm^2.
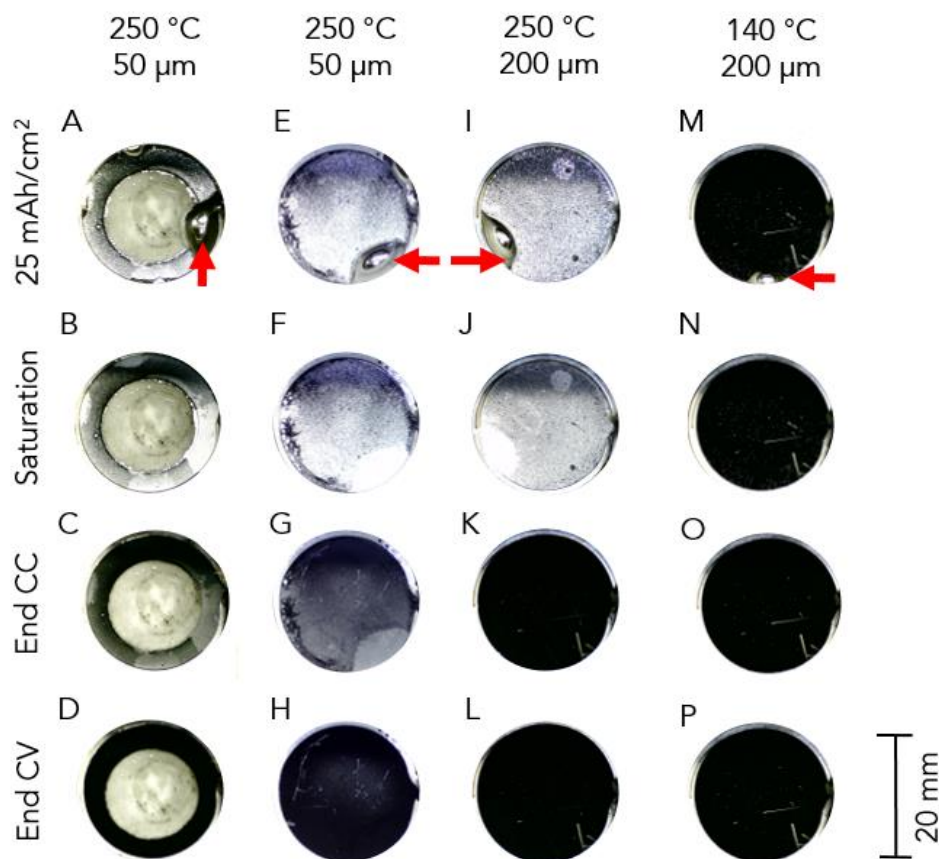
Figure 3-4: Top-view photographs of the open cell showing the carbon-coated Na-β"-alumina surface during liquid sodium metal stripping A-D) 50 μm thick coating on outer ring, with center area uncoated. E-H) 50 μm thick coating covering full Na-β"-alumina area. I-L) and M-P) 200 μm thick coating covering full Na-β"-alumina area measured at 250 °C and 140 °C, respectively. CC stripping at 100 mA/cm² with 25 mAh/cm² of sodium initially plated.

In figure 3-4, we show examples of top-view photographs of different open cell experiments taken during the sodium stripping process at 100 mA/cm² (see figure 3-10 in the supporting information for enlarged views of figure 3-4J, N). For each experiment, we depict the situation after initial plating of 25 mAh/cm², at the end of CC stripping, and at the end of CV stripping, according to the corresponding electrochemical data. After the initial plating, excess sodium is contained in large drops on top of the coating (red arrows). We visually identify when these large sodium drops are consumed upon stripping (figure 3-4B, F, J, N), which we refer to as saturation of the carbon coating. The remaining capacity at saturation thus corresponds to the amount of sodium that can be stored in the pores of the carbon coating and in the carbon itself.

In the first column (figure 3-4A-D), we illustrate the phobicity of the Na-β"-alumina surface to liquid sodium metal at 250°C. In this cell, the 50 μm thick carbon coating on the top-side was applied only to a 4 mm wide outer ring of the Na-β"-alumina disk, leaving the center

uncoated. After plating of 25 mAh/cm^2, corresponding to a nominal sodium metal thickness of 377 µm on the coated ring area, the liquid sodium metal remains confined to the coated area of the Na-β"-alumina disk. Due to poor wetting of liquid sodium metal on Na-β"-alumina, the uncoated center remains free from sodium (figure 3-4A). The large drop adopts a convex shape towards the center to minimize its contact area with the uncoated, sodiophobic Na-β"-alumina surface. Instead, wetting of the nickel ring electrode is favored, as indicated by the spreading of the large drop along the ring electrode.

The second and third column (figure 3-4E-H, I-L) show the corresponding cell with 50 µm and 200 µm thick carbon coatings, covering the entire Na-β"-alumina disk surface. Here, plating of 25 mAh/cm^2 corresponds to a nominal sodium metal thickness of 242 µm. In all experiments at 250 °C, small sodium droplets in and on the carbon coating lead to a metallic shine of the electrode after plating (figure 3-4A, E, I). This is in contrast to the situation at 140 °C depicted in the forth column (figure 3-4M-P), where the carbon coating appears mainly black. Excess sodium contained in large drops after plating of 25 mAh/cm^2 features a smaller footprint at 140 °C compared to 250 °C, indicating reduced wetting of the carbon coating by liquid sodium at the lower temperature. Despite the different visual appearance at 250 °C and 140 °C, the 200 µm thick carbon coating contains a similar amount of sodium at saturation (11 mAh/cm^2 and 9.5 mAh/cm^2, respectively, figure 3-4J, N). The capacity at saturation scales with thickness, but also with the area of the coating (2 mAh/cm^2, figure 3-4B, and 2.5 mAh/cm^2, figure 3-4F). Thus, the carbon coating holds 5 mAh/cm^2 of liquid sodium per 100 µm coating thickness in all cases shown in figure 3-4. Taking into account the volumetric capacity of liquid sodium metal[33], this corresponds to a filling of the porous carbon coating of ~65 vol%.

Upon continued galvanostatic stripping, sodium is gradually removed from the carbon coating. At the end of the CC step, the metallic shine of sodium is partially visible through the 50 µm coating at 250 °C (figure 3-4C, G), while the 200 µm coating appears black (figure 3-4K, O). For the thinner coating, brighter areas remain where large drops were located before (figure 3-4C, G), indicating inhomogeneous transport through the carbon coating. However, sodium is extracted also from these regions during the CV step (figure 3-4D, H).
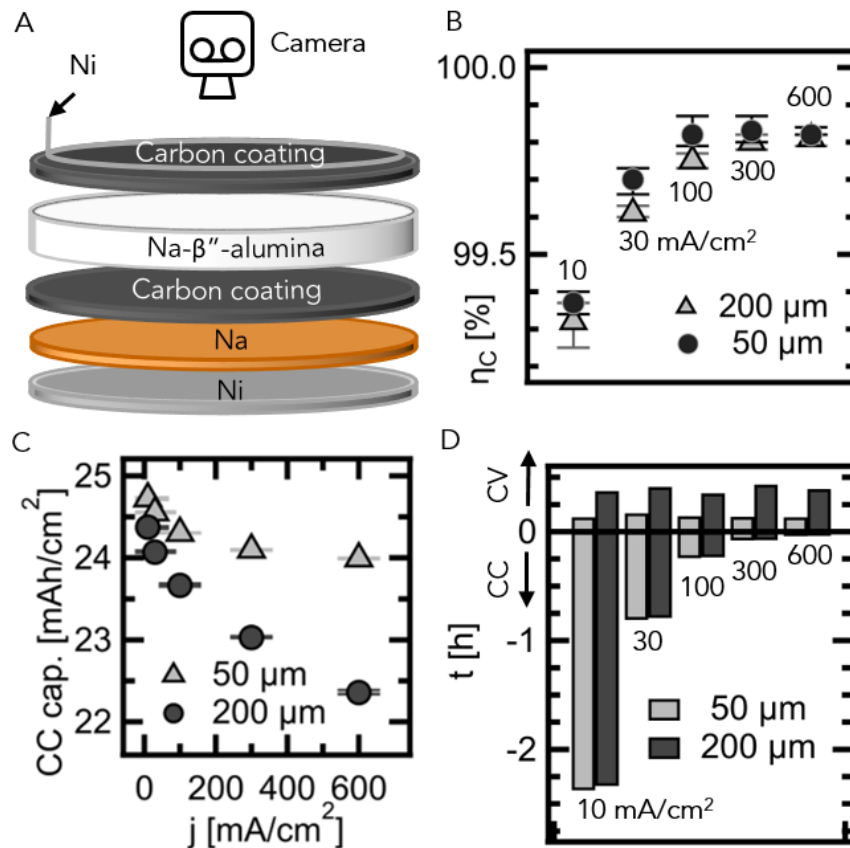
Figure 3-5: Open cell experiments at 250°C A) Schematic of the open cell allowing visual access to the top electrode. B) Coulombic efficiency, η_C at each CC stripping rate for 50 μm and 200 μm thick carbon coatings. C) CC stripping capacity as a function of CC stripping rate and coating thickness. D) Stripping time t for the CC and CV step as a function of CC stripping rate and coating thickness.

Figure 3-5 summarizes the electrochemical results obtained with the open cell during stripping at 250 °C as a function of coating thickness and current density (see figure 3-11 for an overview on cell voltage and capacity evolution with time). A schematic of the open cell is shown in figure 3-5A. Figure 3-5B shows the Coulombic efficiency of the open cell with thin and thick coatings for CC stripping at current densities ranging from 10 to 600 mA/cm^2, followed by CV soaking at 2.5 V until the current drops to 0.1 mA/cm^2. The maximum variation over five consecutive cycles is given for each current density by the error bars. At low stripping current densities of 10 mA/cm^2, the Coulombic efficiency is 99.2%. We attribute this to slow, irreversible chemical oxidation of the highly reactive liquid sodium surface by residues in the argon glovebox atmosphere during the long cycle time of 2.8 hours. For higher stripping current densities of 300 and 600 mA/cm^2 resulting in much shorter cycle times, an excellent Coulombic efficiency of 99.8% is achieved, demonstrating that the carbon coating is an effective solution for supplying liquid sodium metal to the sodiophobic Na-β''-alumina surface at 250 °C. Comparison of the results for the 50 and 200 μm thick

coating in figure 3-5B shows that the coating thickness does not significantly affect the Coulombic efficiency.

In figure 3-5C, we display the capacity retrieved from the carbon coating at CC only (not including the constant voltage capacity, see figure 3-11 for detailed stripping curves and Coulombic efficiency without CV soaking). Comparison of the results for the 50 and 200 μm thick coating reveals that the capacity retrieved during the CC step is strongly dependent on the carbon coating thickness. Especially at high CC densities, up to 1.64 mAh/cm^2 more capacity is retrieved with the 50 μm thick coating than with the 200 μm thick coating. We ascribe this to the increased flow resistance of liquid sodium in the thicker porous coating. Specifically at 600 mA/cm^2, 96% of the capacity is retrieved under constant current stripping with the 50 μm thick coating, while only 90% of the capacity is accessible with the 200 μm thick coating.

Figure 3-5D compares the CC and CV stripping times, t, for the two coating thicknesses at different CC stripping rates. The CC stripping time is linearly dependent on the CC stripping rate. The CC stripping time for the 200 μm coating is slightly shorter than for the 50 μm coating due to the lower CC capacity extracted with the thicker coating (see figure 3-5C). The CV stripping time is not significantly affected by the CC stripping current density, although the capacity extracted at CV differs significantly at high CC (compare with figure 3-5B). The 50 μm thick coating accelerates the CV step by a factor of 3 compared to the 200 μm thick coating, because of reduced flow resistance in the porous coating.
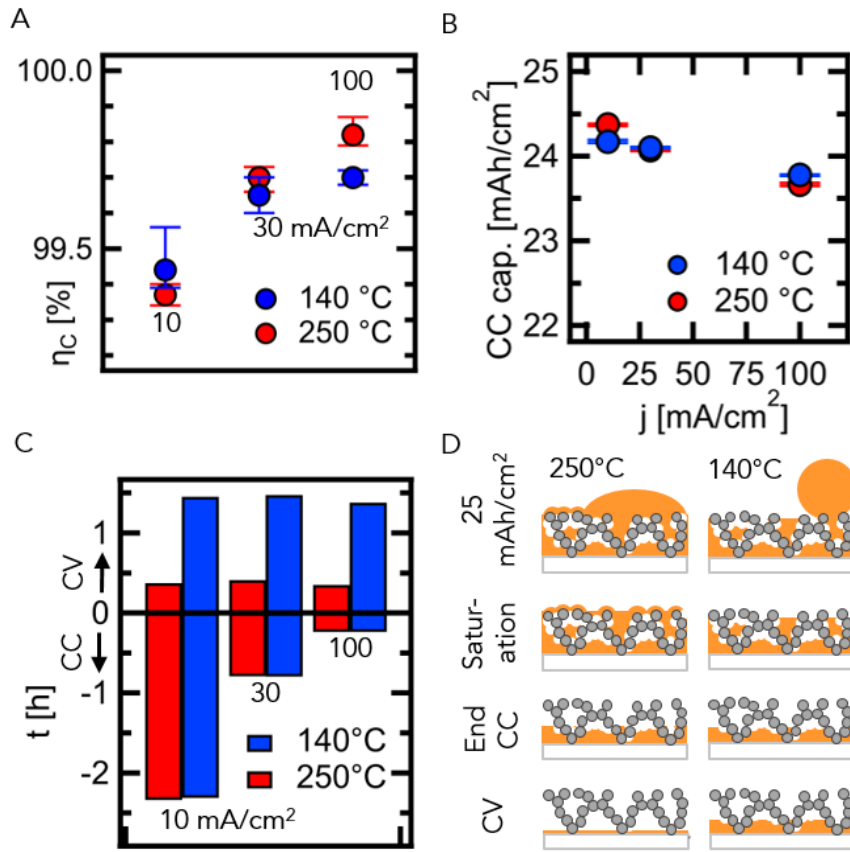
Figure 3-6: The effect of temperature on the stripping behavior for 200 µm coatings at 140 °C and 250 °C A) Coulombic efficiency η_C for different CC stripping rates. B) CC stripping capacity as a function of CC stripping rate. C) CC and CV stripping time t as a function of CC stripping rate. D) Illustration of the observed stripping behavior of liquid sodium metal (orange color) in porous carbon films (grey spheres) at 140 and 250 °C.

In figure 3-6, we investigate the effect of temperature on the stripping behavior with the 200 µm thick coating. Coulombic efficiency and CC retrievable capacity shown in figure 3-6A and figure 3-6B are affected only slightly by temperature. However, the CV stripping time shown in figure 3-6C increases by almost a factor of 4, when the temperature is reduced from 250 to 140 °C. We ascribe the increase in CV stripping time to the 20% increase in dynamic viscosity of liquid sodium when reducing the temperature to 140 °C [34], resulting in an increase in flow resistance in the porous coating. Detailed stripping curves for 10, 30 and 100 mA/cm^2 can be found in figure 3-12.

Figure 3-6D depicts schematically the situation at 250 and 140 °C. At 250 °C, numerous small sodium droplets cover the top of the carbon coating, some of which coalesce into a large, millimeter-sized drop with good wetting to the coating. In contrast, at 140 °C, few small sodium droplets are visible on the top of the carbon coating and the plated sodium appears as a single large drop with poor wetting to the coating. At both temperatures, the large drop is consumed during CC stripping. At saturation, small sodium droplets remain

visible on top of the coating at 250 °C, while very few are visible at 140 °C. Despite the different surface appearance, sodium filling within the coating and CC capacity is similar. Extraction of sodium remaining in the pores of the carbon coating and the carbon itself during the CV stripping step requires more time at 140 °C due to the increase in flow resistance resulting from the increase in sodium viscosity.

3.3 Conclusion

In summary, we investigated the plating and stripping behavior of liquid sodium from ceramic Na-β''-alumina electrolytes in symmetric closed and asymmetric open cell configurations. Critical for the operation of liquid sodium electrodes is the porous carbon coating applied to the Na-β''-alumina electrolyte. Besides acting as a porous electrode providing electrons to the Na-β''-alumina surface, the porous carbon coating serves as reservoir to store and supply liquid sodium to the Na-β''-alumina surface and allows wetting of the sodiophobic Na-β''-alumina surface. On one hand, the storage capacity increases with the coating thickness (approximately 5 mAh/cm^2 per 100 μm coating thickness). On the other hand, thinner carbon coatings enable higher CC current rates and reduce the CV soaking time by minimizing the flow resistance of liquid sodium in the porous carbon coating.

For practical applications, the sodium in the porous carbon coating should not be depleted completely during cycling to avoid additional run-in cycles. Our results show that for a 50 μm thick carbon coating that can hold up to 2.5 mAh/cm^2 of liquid sodium in its pores at saturation, CC stripping at 600 mAh/cm^2 can be maintained down to a filling level of 1 mAh/cm^2. For a 25 mAh/cm^2 sodium metal anode, this corresponds to a small sodium excess of 4%. When considering a sodium metal anode with 5 mAh/cm^2, which is an areal charge density typical for a lithium-ion battery, the excess is on the order of 20%, which is still a very low value compared to other alkali metal anodes reported in literature.[8] Reducing the temperature from 250 °C to 140 °C mainly prolongs the CV soaking time, but does not affect the CC stripping capacity and time substantially.

No dendrite formation is observed for liquid sodium metal anodes up to current densities of 2600 mAh/cm^2 and 10 Ah/cm^2 cumulative plated capacity at 250 °C. This indicates that dendrite formation is less related to the properties of the Na-β''-alumina electrolyte, but rather to the properties of the sodium metal anode. Thus, battery operation at increased temperatures is an efficient means enabling enhanced charge and discharge rates. For room-temperature applications, controlling the mechanical properties of solid alkali metal anodes, e.g. by alloying with another component, may hold the key for suppressing dendrites and enabling the commercialization of solid alkali metal anodes in next-generation batteries.

3.4 Methods

Na-β"-alumina disks with a thickness of 1 mm (symmetric cell) or 1.7 mm (open cells) and 35 mm diameter were sintered at 1600 °C for 5 min from powders following ref. 23 and joined to two α-alumina rings using a glass paste. To prevent dewetting of liquid sodium from the Na-β"-alumina surface, a porous coating consisting of carbon black particles (7 wt%) and sodium hexametaphosphate (11 wt%) was applied by spray coating (2-8 passages) from a dispersion in isopropanol (55 wt%) and water (27 wt%) followed by drying in air at 280 °C. The coating thickness was varied between 50 and 200 μm on the top electrode, and was fixed to 50 μm at the bottom electrode. Scanning electron microscopy images were taken on a Hitachi S4800. The electronic conductivity of the carbon coatings was measured using a Keithley 2000 multimeter and 10 mm wide platinum electrodes sputtered onto the Na-β"-alumina disks at a distance of 2, 5, and 15 mm using the transfer length method on a hot plate at 250 °C. The conductivity of the Na-β"-alumina disks was measured by electrochemical impedance spectroscopy in four-point-probe configuration inside a tube furnace using a Zahner IM6 impedance analyser.[23] Electrochemical cells with spring-loaded cylindrical nickel current collectors and an active area of 3.14 cm^2 were assembled in an argon-filled glovebox based on the ceramic Na-β"-alumina electrolyte disk and α-alumina rings (figure 3-7). A type K thermocouple was inserted at the interface between α-alumina and Na-β"-alumina for accurate cell temperature determination. Sodium metal foils with a purity of 99.9% and an areal mass of 0.16 g/cm^2 (0.5 g) were inserted between the Na-β"-alumina and the current collectors.

To monitor sodium plating and stripping visually with a camera (DNT Digi Micro Scale, 1920x1020 pixels, 10 s picture interval), an open cell was assembled by replacing the cylindrical top current collector by a nickel ring electrode. Thermography was conducted with a Hotfind LX camera. In a separate calibration experiment, the radiative emissivity of the carbon coating was determined to be 0.85 at a temperature of 250 °C. In this calibration experiment, the surface temperature of a carbon coated hotplate was accurately measured with a type K thermocouple, while simultaneously thermographic images of the hot plate surface were taken. The radiative emissivity of the coating was finally determined by internally adjusting the emissivity settings of the thermography camera until the surface temperature measurements matched between the thermocouple measurement and the thermography measurement. Cell heating for all experiments was realized via a resistive coil heater wrapped around the cell, while cell temperature was controlled via a feedforward controller. Stripping and plating experiments were conducted in a glovebox under argon atmosphere with H_2O and O_2 levels below 0.1 ppm. Prior to electrochemical and direct visual characterization, each cell passed run-in cycles with 25 mAh/cm^2 of charge transferred until cell resistance dropped below 1.8 Ωcm^2 for a maximum time of 30 h. For each current density, five entire plating and stripping cycles were performed to evaluate the Coulombic efficiency. Cells were cycled with a Biologic SP-150 attached to a 20 A booster.

Acknowledgments

3.5 Supporting information
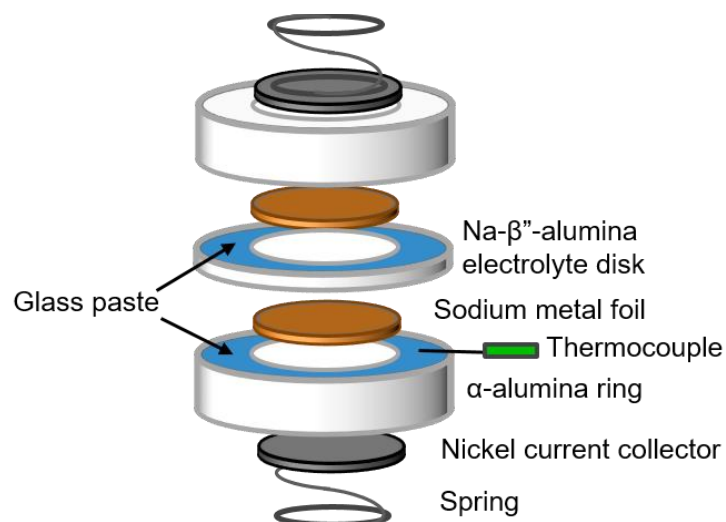
Figure 3-7: Schematic of closed cell.
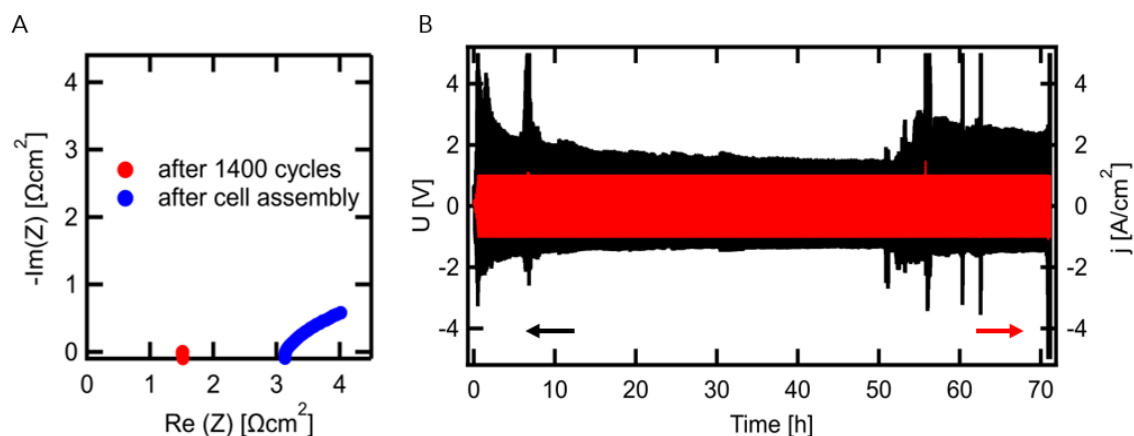
Figure 3-8: Symmetric cell cycling at 1000 mA/cm2 and 250 °C. A) Electrochemical imped-ance spectroscopy of closed symmetric cell after cell assembly (blue) and after cycling at 1000 A/cm² (red) showing negligible interfacial resistance between cell components and confirm the overall cell resistance of 1.4 Ωcm². B) Overpotential U (black) as function of current density j (red) showing run in cycles (until 30 h), cycling (30-50 h), and cell failure due to sodium depletion (50-70 h).
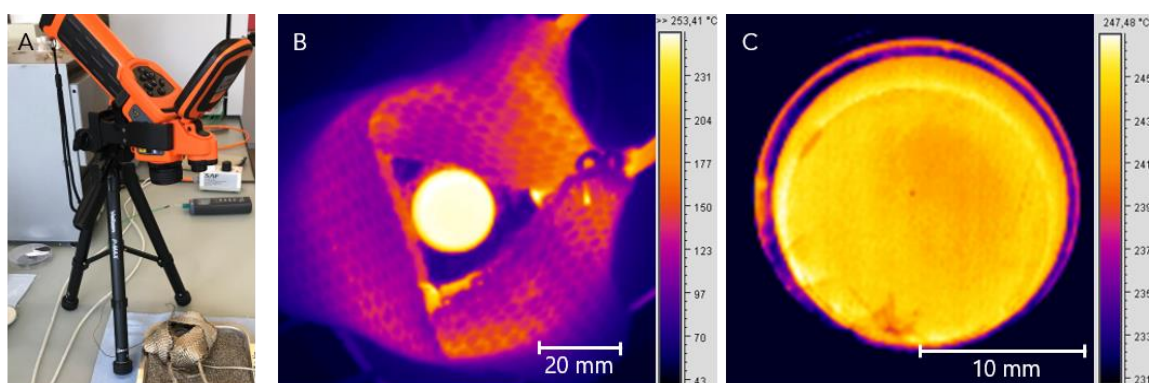
Figure 3-9: Thermography of open cell at 250 °C. A) Set-up: Open cell with thermography camera. B) Top-view on open cell showing highest temperatures on the exposed carbon coating. C) Zoom on cell opening showing an effective coating surface temperature of 245°C (set point: 250 °C) with a temperature difference < 5 K across the entire exposed surface.
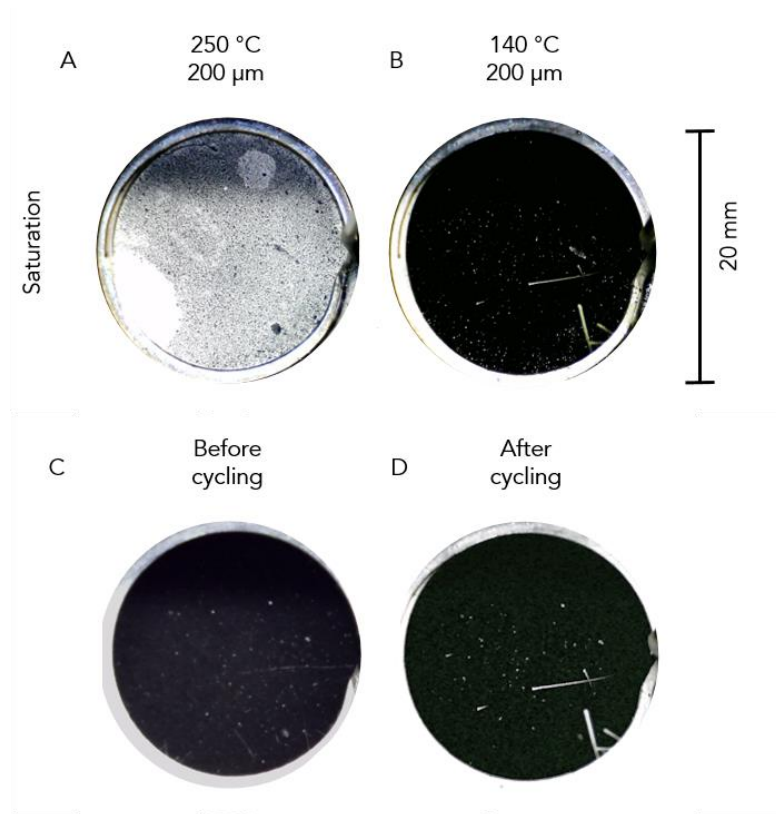
Figure 3-10: Top-view photographs of the open cell showing the 200 μm thick carbon coating on Na-β"-alumina surface. Figure 3-10A, B show saturation during liquid sodium metal stripping at 100 mA/cm2 at 250 °C (A) and 140 °C (B), respectively. Appearance of pristine (C) and cycled coating (D) after 70 cycles with 25 mAh/cm² capacity transferred and current densities and temperatures ranging from 10 – 600 mA/cm² and 140 – 250 °C respectively, showing no cracks or delamination of coating.
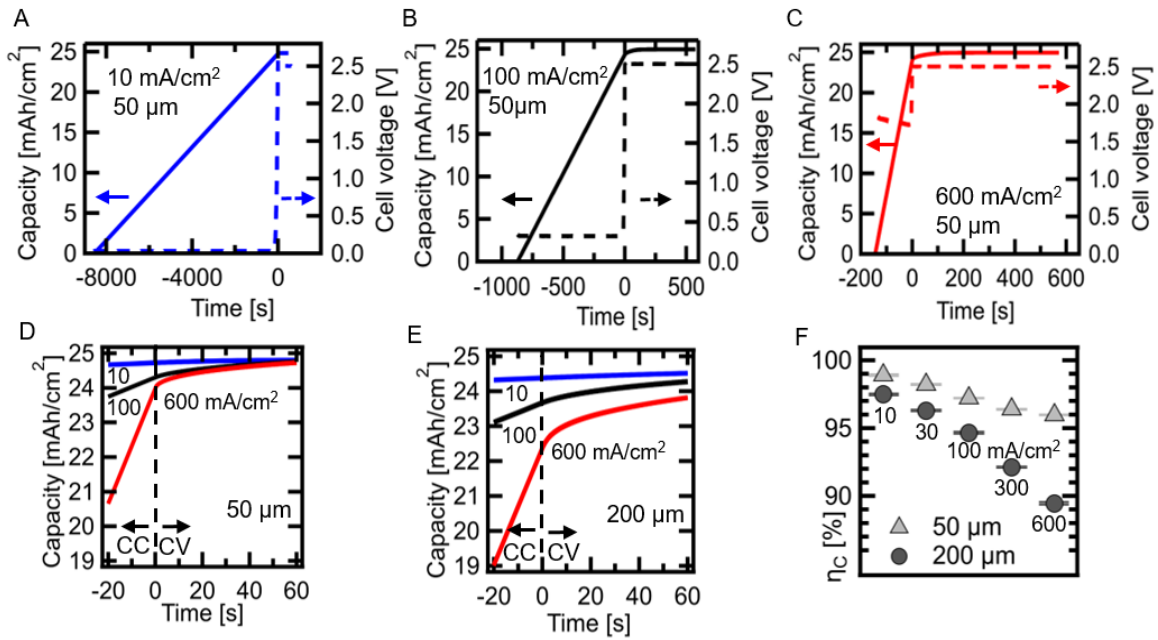
Figure 3-11: Open cell capacity retention for 50 and 200 µm coating. A, B, C) Capacity and cell voltage for complete stripping process as function of time for 50 µm thick carbon coating at 250 °C and current densities of 10 , 100, 600 mA/cm². D) Same capacity data, zoomed in to show details of the transition between constant current (CC) and constant voltage (CV) stripping. E) Capacity as function of time, zoomed-in to transition between CC and CV stripping, for 200 µm thick carbon coatings at 250 °C. F) Coulombic efficiency without constant voltage step for 50 and 200 µm thick carbon coatings.
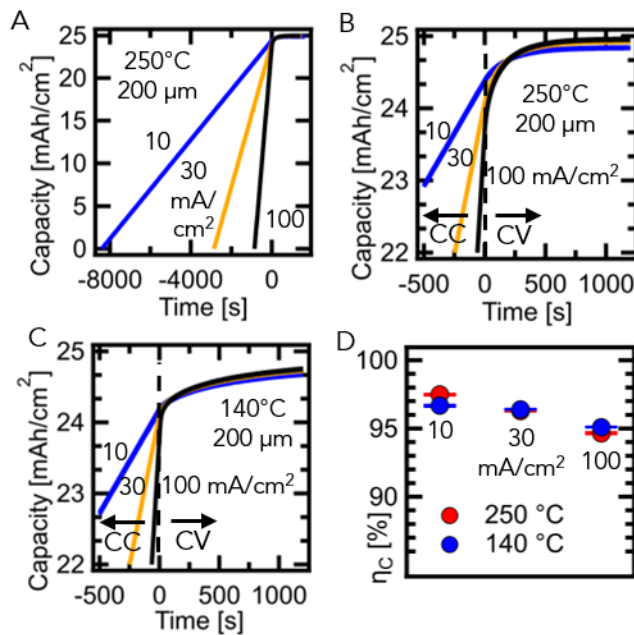
Figure 3-12: Open cell capacity retention for 250 and 140 °C. A) Capacity for complete stripping process as function of time for 200 µm thick carbon coating at 250 °C, Capacity as

function of time for different CC stripping rates with 200 µm thick carbon coatings at 250 (B) and 140 °C (C), D) Coulombic efficiency without constant voltage step for 140 and 250 °C for the 200 µm thick carbon coating.

References

[1]   Winter, M., Barnett, B., and Xu, K. (2018). Before Li-ion batteries. Chem. Rev. *118*, 11433–11456.

[2]   Luo, W., and Hu, L. (2015). Na metal anode: "holy grail" for room-temperature Na-ion batteries? ACS Cent. Sci. *1*, 420–422.

[3]   Lin, D., Liu, Y., and Cui, Y. (2017). Reviving the lithium metal anode for high-energy batteries. Nat. Nanotechnol. *12*, 194–206.

[4]   Seh, Z.W., Sun, J., Sun, Y., and Cui, Y. (2015). A highly reversible room-temperature sodium metal anode. ACS Cent. Sci. *1*, 449–455.

[5]   Lee, B., Paek, E., Mitlin, D., and Lee, S.W. (2019). Sodium metal anodes: emerging solutions to dendrite growth. Chem. Rev. *119*, 5416–5460.

[6]   Liu, B., Zhang, J.G., and Xu, W. (2018). Advancing lithium metal batteries. Joule *2*, 833–845.

[7]   Shen, Y., Zhang, Y., Han, S., Wang, J., Peng, Z., and Chen, L. (2018). Unlocking the energy capabilities of lithium metal electrode with solid-state electrolytes. Joule *2*, 1674–1689.

[8]   Albertus, P., Babinec, S., Litzelman, S., and Newman, A. (2018). Status and challenges in enabling the lithium metal electrode for high-energy and low-cost rechargeable batteries. Nat. Energy *3*, 16–21.

[9]   Sharafi, A., Kazyak, E., Davis, A.L., Yu, S., Thompson, T., Siegel, D.J., Dasgupta, N.P., and Sakamoto, J. (2017). Surface chemistry mechanism of ultra-low interfacial resistance in the solid-state electrolyte Li7La3Zr2O12. Chem. Mater. *29*, 7961–7968.

[10]   Bay, M.C., Wang, M., Grissa, R., Heinz, M.V.F., Sakamoto, J., and Battaglia, C. (2020). Sodium plating from Na-β"-alumina ceramics at room temperature, paving the way for fast-charging all-solid-state batteries. Adv. Energy Mater. *10*, 1–8.

[11]   Sharafi, A., Meyer, H.M., Nanda, J., Wolfenstine, J., and Sakamoto, J. (2016). Characterizing the Li-Li7La3Zr2O12 interface stability and kinetics as a function of temperature and current density. J. Power Sources *302*, 135–139.

[12]   Han, X., Gong, Y., Fu, K., He, X., Hitz, G.T., Dai, J., Pearse, A., Liu, B., Wang, H., Rubloff, G., et al. (2017). Negating interfacial impedance in garnet-based solid-state Li metal batteries. Nat. Mater. *16*, 572–579.

[13]   Reed, D., Coffey, G., Mast, E., Canfield, N., Mansurov, J., Lu, X., and Sprenkle, V. (2013). Wetting of sodium on β"-Al2O3/YSZ composites for low temperature planar sodium-metal-halide batteries. J. Power Sources *227*, 94–100.

[14] Jin, D., Choi, S., Jang, W., Soon, A., Kim, J., Moon, H., Lee, W., Lee, Y., Son, S., Park, Y.-C., et al. (2019). Bismuth islands for low-temperature sodium-beta-alumina batteries. ACS Appl. Mater. Interfaces *11*, 2917–2924.

[15] Lu, X., Li, G., Kim, J.Y., Mei, D., Lemmon, J.P., Sprenkle, V.L., and Liu, J. (2014). Liquid-metal electrode to enable ultra-low temperature sodium-beta alumina batteries for renewable energy storage. Nat. Commun. *5*, 1–8.

[16] Luo, W., Gong, Y., Zhu, Y., Li, Y., Yao, Y., Zhang, Y., Fu, K.K., Pastel, G., Lin, C.F., Mo, Y., et al. (2017). Reducing interfacial resistance between garnet-structured solid-state electrolyte and Li-metal anode by a germanium layer. Adv. Mater. *29*, 1–7.

[17] Tsai, C.L., Roddatis, V., Chandran, C.V., Ma, Q., Uhlenbruck, S., Bram, M., Heitjans, P., and Guillon, O. (2016). Li7La3Zr2O12 interface modification for Li dendrite prevention. ACS Appl. Mater. Interfaces *8*, 10617–10626.

[18] Wang, J., Wang, H., Xie, J., Yang, A., Pei, A., Wu, C.L., Shi, F., Liu, Y., Lin, D., Gong, Y., et al. (2018). Fundamental study on the wetting property of liquid lithium. Energy Storage Mater. *14*, 345–350.

[19] Tian, Y., Sun, Y., Hannah, D.C., Xiao, Y., Liu, H., Chapman, K.W., Bo, S.H., and Ceder, G. (2019). Reactivity-guided interface design in Na metal solid-state batteries. Joule *3*, 1037–1050.

[20] Kasemchainan, J., Zekoll, S., Spencer Jolly, D., Ning, Z., Hartley, G.O., Marrow, J., and Bruce, P.G. (2019). Critical stripping current leads to dendrite formation on plating in lithium anode solid electrolyte cells. Nat. Mater. *18*, 1105–1111.

[21] Wang, M.J., Choudhury, R., and Sakamoto, J. (2019). Characterizing the Li-solid-electrolyte interface dynamics as a function of stack pressure and current density. Joule *3*, 2165–2178.

[22] Sudworth, J.L. (2001). The sodium/nickel chloride (ZEBRA) battery. J. Power Sources *100*, 149–163.

[23] Bay, M., Heinz, M.V.F., Figi, R., Schreiner, C., Basso, D., Zanon, N., Vogt, U.F., and Battaglia, C. (2018). Impact of liquid phase formation on microstructure and conductivity of Li-stabilized Na-β"-alumina ceramics. ACS Appl. Energy Mater. *2*, 687–693.

[24] Ho, C.Y., Ackerman, M.W., Wu, K.Y., Havill, T.N., Bogaard, R.H., Matula, R.A., Oh, S.G., and James, H.M. (1983). Electrical resistivity of ten selected binary alloy systems. J. Phys. Chem. Ref. Data *12*, 183–322.

[25] J.F. Freedman; Yale University (1960). Electrical resistivity of liquid sodium, liquid lithium, and dilute liquid sodium. J. Chem. Phys. *34*.

[26] Bay, M., Heinz, M.V.F., Linte, C., German, A., Blugan, G., Battaglia, C., and Vogt, U.F. (2020). Impact of sintering conditions and zirconia addition on flexural strength and ion conductivity of Na-β"-alumina ceramics. Mater. Today Commun. *in Press*.

[27] Heinz, V.F.M., Graeber, G., Landmann, D., and Battaglia, C. (2020). Pressure management and cell design in solid-electrolyte batteries, at the example of a sodium-nickel-chloride battery. J. Power Sources *465*.

[28] Wood, K.N., Kazyak, E., Chadwick, A.F., Chen, K.H., Zhang, J.G., Thornton, K., and Dasgupta, N.P. (2016). Dendrites and pits: untangling the complex behavior of lithium metal anodes through operando video microscopy. ACS Cent. Sci. *2*, 790–801.

[29] Chen, K.H., Wood, K.N., Kazyak, E., Lepage, W.S., Davis, A.L., Sanchez, A.J., and Dasgupta, N.P. (2017). Dead lithium: Mass transport effects on voltage, capacity, and failure of lithium metal anodes. J. Mater. Chem. A *5*, 11671–11681.

[30] Heine, J., Krüger, S., Hartnig, C., Wietelmann, U., Winter, M., and Bieker, P. (2014). Coated lithium powder (CLiP) electrodes for lithium-metal batteries. Adv. Energy Mater. *4*, 1–7.

[31] Bieker, G., Winter, M., and Bieker, P. (2015). Electrochemical in situ investigations of SEI and dendrite formation on the lithium metal anode. Phys. Chem. Chem. Phys. *17*, 8670–8679.

[32] Lin, D., Liu, Y., Liang, Z., Lee, H.W., Sun, J., Wang, H., Yan, K., Xie, J., and Cui, Y. (2016). Layered reduced graphene oxide with nanoscale interlayer gaps as a stable host for lithium metal anodes. Nat. Nanotechnol. *11*, 626–632.

[33] Huijben, M.J., van Hasselt, J.P., van der Weg, K., and van der Lugt, W. (1976). Density of liquid sodium-potassium and potassium-rubidium alloys. Scr. Metall. *10*, 571–574.

[34] Chiong, Y.S. (1936). Viscosity of liquid sodium and potassium. Proc. R. Soc. London. Ser. A - Math. Phys. Sci. *157*, 264–277.

4. Elucidation of the rate-limiting processes in high-temperature sodium-metal-chloride batteries [*]

Submitted

In this fundamental study, we investigate de-/chlorination mechanisms of nickel and iron in sodium tetrachloroaluminate at 300 °C to unveil rate-limiting processes at the positive electrode of sodium-nickel-chloride batteries. The home-built electrochemical cell takes over the negative electrode assessed and characterized in chapter 3 and uses planar nickel and iron positive electrodes.

Author contributions

D.L. conceived the idea for this study and designed the experiments together with M.H., P.S., and C.B. E.S. prepared most of the Na-β"-alumina electrolytes for the experiments. D.L. designed the electrochemical cell and performed the experiments with planar electrodes. D.L. analyzed the data, prepared the figures, and wrote the manuscript. M.H., P.S., and C.B. critically reviewed and edited the manuscript. All coauthors read, commented, and approved the final manuscript.

Abstract

Sodium-metal chloride batteries are considered a sustainable and safe alternative to lithium-ion batteries for large-scale stationary electricity storage. Although competitive in terms of energy density, the charge and discharge rate capability of sodium-metal chloride batteries can currently not rival with lithium-ion batteries. Several studies identified transition-metal-ion migration through the metal chloride conversion layer on the positive electrode as the rate-limiting step, limiting charge and discharge rates in sodium-metal chloride batteries. Here we reinvestigate the rate-limiting processes during electrochemical nickel and iron chlorination in planar model electrode geometry in liquid sodium tetrachloroaluminate electrolyte at 300 °C. Analysis of cyclic voltammetry data via the Randles-Sevcik equation reveals a diffusion-controlled process during oxidation with a diffusion coefficient of $2.3 \cdot 10^{-3}$ cm^2/s for the nickel electrode and an upper bound of $1.2 \cdot 10^{-5}$ cm^2/s for the diffusion coefficient for the iron electrode. Post-mortem analysis of the electrodes via scanning electron microscopy at different degrees of chlorination, corresponding to different states of charge, shows that chlorination of the nickel electrode proceeds via uniform oxidation of nickel and the formation of NiCl$_2$ platelets on the surface of the electrode. In contrast, the chlorination of the iron electrodes proceeds via stress-induced cracking, resulting in non-uniform iron oxidation and the pulverization of the iron electrode. Our results demonstrate that transition-metal-ion diffusion in the tetrachloroaluminate electrolyte rather than across the metal chloride layer is limiting the rate capability of planar nickel and iron electrodes. We also discuss the transition from planar model electrodes to porous high-capacity electrodes, where sodium-ion migration along the tortuous path in the porous electrode can become the rate-limiting process depending on state of charge and cycling rate. In addition to sodium-ion conductivity, it is thus also important to improve transition-metal-ion diffusion in the tetrachloroaluminate electrolyte, preferably by enhancing

transition-metal-ion mobility. Increasing transition-metal-ion solubility in the tetrachloro-aluminate electrolyte represents an alternative approach but tends to compromise long-term cycling stability. These mechanistic insights are important to derive guidelines for the design of competitive next-generation sodium-metal chloride batteries with improved rate performance.

4.1 Introduction

Sodium-metal chloride batteries, typically operated at 300 °C, have a proven track record for backup power applications, but also represent a promising option for large-scale stationary electricity storage due to the absence of critical raw materials, such as lithium and cobalt.[1–9] These batteries employ a solid ceramic Na-β"-alumina electrolyte in combination with a molten inorganic tetrachloroaluminate ($NaAlCl_4$) electrolyte, improving operational safety compared to state-of-the-art lithium-ion batteries.[10–12] However, while the energy density of sodium-metal chloride batteries is relatively high (e.g. 140 Wh/kg, 280 Wh/l on cell level), the charge and discharge rate capability of sodium-metal chlorides batteries needs to be improved to be competitive with lithium-ion batteries.[5,13]

Sodium-metal chloride batteries are assembled in the discharged state. This avoids the handling of sodium metal, which forms the negative electrode, during cell assembly. Liquid sodium is generated electrochemically during the first charge. Oxidation and reduction of sodium metal (Na $\Leftrightarrow$ Na$^+$ + e$^-$) at temperatures above the melting point is extremely fast, enabling current densities beyond 1000 mA/cm^2 without significant overpotential.[14] It is thus the positive electrode, which limits the overall battery performance. The positive electrode is a composite, comprising mainly nickel, iron, and sodium chloride in the discharged state. The porous positive electrode is immersed in molten $NaAlCl_4$ electrolyte, separated from the sodium metal negative electrode by the ceramic Na-β"-alumina electrolyte. During dis-/charge cycling at 300 °C, the following half-cell conversion reactions take place[1,3,4,9,15]:

Fe + 2NaCl $\Leftrightarrow$ FeCl$_2$ + 2Na$^+$ (2.33 V vs. Na/Na$^+$)   Reaction 6

Ni + 2NaCl $\Leftrightarrow$ NiCl$_2$ + 2Na$^+$ (2.58 V vs. Na/Na$^+$)   Reaction 7
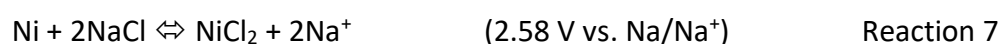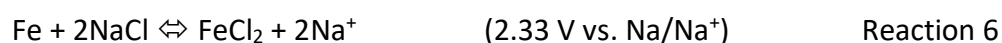
State-of-the-art commercial sodium-metal chloride cells derive the majority of their capacity from the de-/chlorination of nickel,[4,16] which provides a higher cell potential and higher cycling stability compared to the de-/chlorination of iron.[17] During charge (reaction 6,7), sodium-ions migrate from the positive to the negative electrode, and vice versa during discharge. Commercial cells feature a capacity of 38 Ah per cell, corresponding to an area specific capacity of approximately 150 mAh/cm^2, and a porous positive electrode composite thickness of up to 18 mm,[5,18] supporting continuous dis-/charging at 75 mA/cm^2

(C/2).[19] While pulsed dis-/charge at higher current density is possible, the target for next-generation sodium-metal chloride batteries is 150 mA/cm^2 continuous dis-/charge (1C). For comparison, high-energy lithium-ion batteries feature capacities of only up to 4-5 mAh/cm^2, and electrodes with a thickness on the order of only 0.1 mm, explaining their currently still superior rate capability.[20]

A recent study on sodium-metal chloride cells identified the transport of Na$^+$ ions as a rate-limiting process in state-of-the-art porous positive electrode composites, even for a relatively lower area specific capacity of 50 mAh/cm^2.[16] The self-limiting nature of the conversion reaction of nickel and iron to nickel chloride and iron chloride causes local passivation[21]. As a result, de-/chlorination proceeds along a reaction front away from the Na-β"-alumina electrolyte, deeper into the positive electrode.[18] Because iron is oxidized at a lower potential than nickel, the iron chlorination reaction front is spatially separated from (and precedes) the nickel chlorination reaction front. However, not all factors contributing to the dynamic evolution of cell resistance as a function of state of charge and dis-/charge rate are yet understood. Studies on planar, non-porous model electrodes identified diffusional rate-limitations for the de-/chlorination of iron and nickel in NaAlCl$_4$. De-/chlorination is generally assumed to take place in a continuous, core-shell conversion layer.[17,21–24] The diffusional transport limitations were assigned to the transport of Cl$^-$ or metal ions through the metal chloride conversion layer, either through pores,[17,21–23], or by ion transport through the metal chloride itself.[24]

The aim of this study is to separate and isolate the different rate-limiting processes which determine the cell resistance as a function of state of charge. In particular, we focus here on deconvoluting the de-/chlorination processes of nickel and iron from microstructural effects of the porous electrodes (porosity, tortuosity, etc.) employing planar model electrodes. Combining electrochemical cell characterization with a detailed post-mortem scanning electron microscopy analysis of the electrodes, we identify the rate-limiting process during de-/chlorination and determine the diffusion coefficient of nickel and iron-ions in molten NaAlCl$_4$ electrolyte. These parameters can be employed directly in numerical models for optimizing the microstructure of the porous electrodes and derive guidelines for designing next-generation sodium-metal chloride batteries with improved rate performance.

4.2 Results and discussion
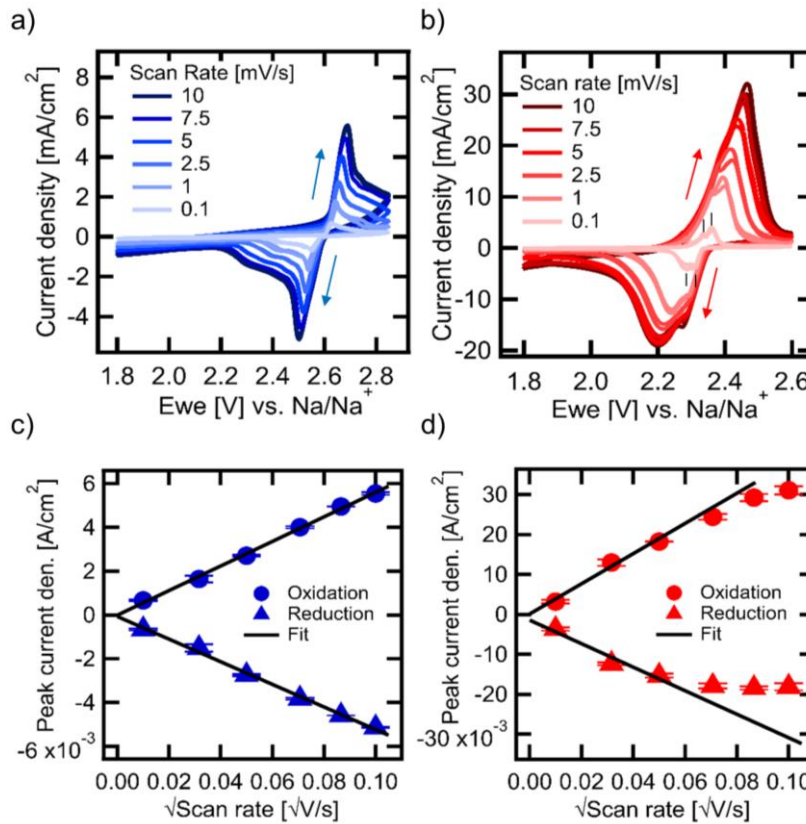
Figure 4-1: Cyclic voltammetry of a) Na/Ni-NiCl₂ and b) Na/Fe-FeCl cells with planar Ni and Fe electrodes at scan rates from 0.1 to 10 mV/s and corresponding Randles-Sevcik plots in c) and d).

In figure. 4-1a, we show the cyclic voltammetry (CV) response of a Na/Ni-NiCl₂ cell with a planar nickel electrode for scan rates ranging from 0.1 to 10 mV/s at 300 °C. The voltage scan from 1.8 to 2.85 V and from 2.85 back to 1.8 V vs. Na/Na⁺ results in a relatively symmetric current response centered around a voltage of 2.59 V vs. Na/Na⁺ at 300 °C. The upper cut-off voltage was limited to 2.85 V vs Na/Na⁺ to prevent decomposition of NaAlCl₄ electrolyte at 3.05 V.[25] Repeated cycling at a fixed scan rate within this voltage window results in a reversible current response (two overlapping voltage scans shown for each scan rate). At a scan rate of 10 mV/s, oxidation and reduction current feature each a sharp current maximum at around 2.66 V and 2.52 V, respectively, which move towards 2.59 V with decreasing scan rate (figure. 4-7a). In scan direction, the current density rises rapidly towards the current maxima, but then falls offs relatively slowly, as de-/chlorination proceeds at higher overpotentials, due to either i) thickening of the chlorinated layer at the electrode surface and/or ii) reduced area of accessible unreacted electrode surface. Analysis of the CV response at 0.1 mV/s in a Tafel plot in figure 4-7b (SI) allows estimation of the exchange current density, which is on the order of 0.2 mA/cm². Identification of a linear regime in

the Tafel plots is difficult because the current density at this scan rate is still limited by cell resistance. Nevertheless, a reasonable estimate is obtained by assuming an anodic transfer coefficient of 0.5, reflecting a reversible electrochemical reaction.[26]

Compared to the Na/Ni-NiCl$_2$ cell, the CV response for the Na/Fe-FeCl$_2$ cell shown in figure 4-1b reveals much higher maximum current densities for the corresponding scan rates (note the different *y*-axis scale). The upper voltage cut-off was set to 2.6 V vs. Na/Na$^+$ to prevent the formation of FeCl$_3$ species at 2.75 V.[4,24] The oxidation current density of the Fe-FeCl$_2$ electrode is dominated by a strong maximum consisting of two overlapping peaks, more clearly resolved at lower scan rates (up to 1 mV/s, figure 4-7c). We attribute the first current peak at 2.34 V vs. Na/Na$^+$ to the formation of Na$_6$FeCl$_8$, and the second one at 2.36 V vs. Na/Na$^+$ to the formation of FeCl$_2$, as previously reported.[27] The oxidation and reduction current response is again relatively symmetric and centered around a voltage of 2.33 V vs. Na/Na$^+$ at 300 °C and reversible at fixed scan rate (two overlapping voltage scans shown for each scan rate). In scan direction, the current density rises rapidly towards the current maxima, but then drops more rapidly than for the Na/Ni-NiCl$_2$ cell in both scan directions, indicating that de-/chlorination proceeds possibly via a different mechanism (see discussion below). Analysis of the CV response at 0.1 mV/s in a Tafel plot in figure 4-7d indicates an exchange current density, which is on the order of 2 mA/cm^2, i.e., a factor of 10 higher than for the Na/Ni-NiCl$_2$ cell, indicating a much faster de-/chlorination mechanism.

In order to quantify the rate-limiting process, current density maxima extracted from the CV-scans in figure 4-1a and b are plotted against the square root of the scan rate in figure 4-1c and d. Due to the extremely high rate capability previously demonstrated for the sodium metal negative electrode in the same cell, but in symmetric electrode configuration[14], the peak current densities are solely assigned to the rate-limiting process in the positive electrode. For a purely diffusion-limited process, the maximum current densities obey Fick's laws of diffusion. The Randles-Sevcik equation represents a solution to Fick's 2nd law for the special case when the concentration of the active species is zero at the electrode surface and constant in the electrolyte and predicts a linear relationship between maximum current density and the square root of the scan rate.[28] Inspection of figure 4-1c and d shows that the Na/Ni-NiCl$_2$ cell displays a very linear behavior for oxidation and reduction, while the Na/Fe-FeCl$_2$ cell displays a slight deviation from the linear behavior, especially during reduction, where maximum current densities stagnate above 5 mV/s.

From the slopes of the Randles-Sevcik plots and the nickel-ion solubility of 2.1·10^{-6} mol/cm^3 in NaAlCl$_4$ [29,30], we can extract the diffusion coefficient of the rate-limiting process in the Na/Ni-NiCl$_2$ cell yielding 2.3·10^{-3} cm^2/s for oxidation and 1.9·10^{-3} cm^2/s for reduction. Details of the calculation are provided in the supplementary information. Although the Randles-Sevcik plots of the Na/Fe-FeCl$_2$ do not exhibit a linear behavior over the full scan rate range, we get a comparative value from a linear fit restricted to the lowest three scan

rates, yielding an upper bound for the diffusion coefficient of $1.2 \cdot 10^{-5}$ cm^2/s during oxidation and $7.2 \cdot 10^{-6}$ cm^2/s during reduction of iron employing a value of $2.0 \cdot 10^{-4}$ mol/cm^3 for the iron-ion solubility in NaAlCl$_4$ [27,30]. These upper bound values obtained for iron are more than two orders of magnitude smaller than the ones obtained for nickel! At first, this result seems counterintuitive, as the exchange current density estimated for iron is a factor of 10 higher than for nickel. This apparent contradiction can be reconciled by noting that the slope of the Randles-Sevcik equation shows a linear dependence on the concentration but only a square root dependence on the diffusion coefficient (see equations in supplementary information). Thus, our data shows that the faster de-/chlorination in the iron system is due to the higher solubility of iron in NaAlCl$_4$ compared to nickel, compensating the lower diffusion coefficient of iron-ions compared to nickel-ions in NaAlCl$_4$ (or in the chloride layer).
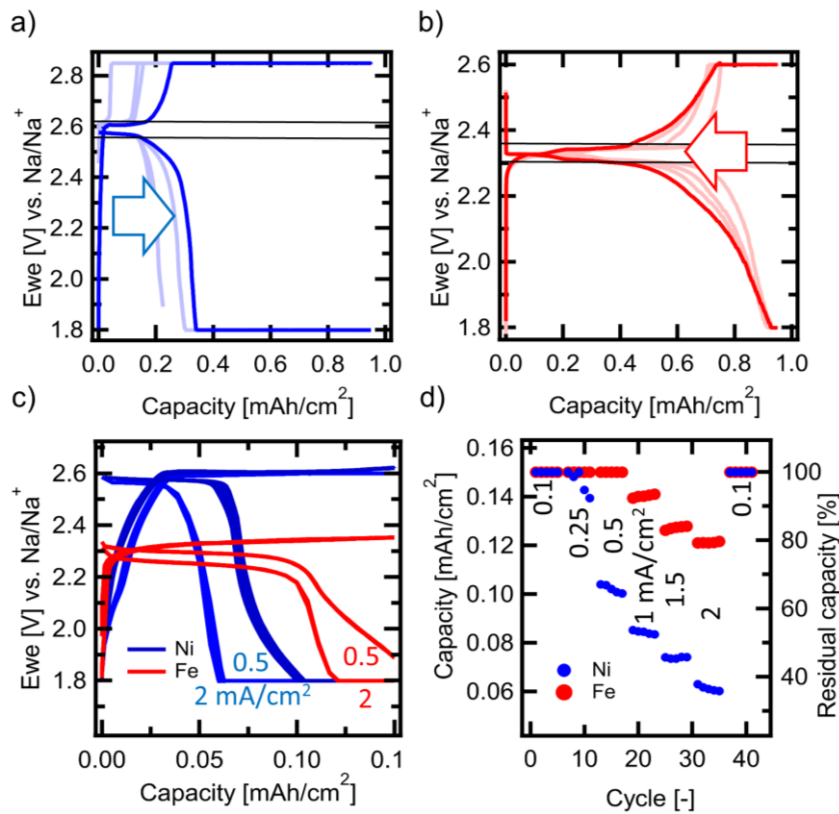
Figure 4-2: Evolution of cell voltage during galvanostatic run-in cycling of the planar a) Ni-NiCl$_2$ and b) Fe-FeCl$_2$ electrode (pale red and blue curves show run-in cycles). c) Capacity limited cycling of planar Ni-NiCl$_2$ and Fe-FeCl$_2$ electrodes with 0.15 mAh/cm^2, at discharge current densities of 0.5 and 2 mA/cm^2, respectively. d) Rate test of planar Ni-NiCl$_2$ and Fe-FeCl$_2$ electrodes.

Figure 4-2a and b compares galvanostatic dis-/charge cycling of Na/Ni-NiCl$_2$ and Na/Fe-FeCl$_2$ cells with planar model electrodes at ±0.5 mA/cm^2. When the upper cut-off voltage of 2.85 and 2.6 V, respectively, is reached upon charge, the cells were held at this voltage until the current density dropped to 0.05 mA/cm^2. Analogously, when the lower cut-off

voltage of 1.8 V is reached upon discharge, the cells were held at this voltage until the current density dropped to -0.05 mA/cm^2. While the galvanostatically accessible discharge capacity increases slowly during the first four cycles for the Na/Ni-NiCl$_2$ cell from 0.22 to 0.35 mAh/cm^2, the Na/Fe-FeCl$_2$ cell delivers a value of 0.95 mAh/cm^2 already in the first cycle. This corresponds to the conversion of a ~1.2 μm thick nickel or iron layer on the planar electrodes. For both types of model electrodes, the capacities accessed in these experiments substantially exceed the local degree of chlorination employed in porous high-capacity cathodes. There, the cell voltage is maintained at a relatively low value, as the reaction front propagates deeper into the porous electrode, continuously accessing additional, unreacted electrode surface. Thus, state-of-the-art commercial sodium-metal-chloride batteries generally restrict cycling to only 0.04 mAh/cm^2 with respect to the porous electrode surface area, corresponding to conversion of a ~50 nm thick nickel or iron layer.[16]

During galvanostatic charging, the cell voltage for the planar model electrode geometry increases due to either i) thickening of the chlorinated layer at the electrode surface and/or ii) reduced area of accessible unreacted electrode surface. It is important to remind ourselves that for porous electrodes, the cell voltage can be maintained at a relatively low value, because iii) the reaction front propagates deeper into the porous electrode continuously 'supplying' additional unreacted electrode surface. Consequently, in porous electrodes, the local degree of chlorination never reaches 0.95 mAh/cm^2 per porous electrode area, which would lead to a breakdown of the electronic nickel/iron backbone of the porous electrode and rapid capacity fading due to loss of electronic contact of a fraction of the active electrode material to the current collector. Reversible, stable cycling of the planar model electrodes is achieved when limiting the capacity to 0.15 mAh/cm^2 (i.e. the conversion of a ~200 nm thick nickel or iron layer). This corresponds to an increase in cell voltage of ± 0.03 V.

Figure 4-2c compares galvanostatic dis-/charge cycling of Na/Ni-NiCl$_2$ and Na/Fe-FeCl$_2$ cells with planar model electrodes and at a capacity limited to 0.15 mAh/cm^2. During charge, a current density of 0.5 mA/cm^2 was applied, while during discharge a current density of 0.5 and 2 mA/cm^2 was employed. For each current density, 5 cycles are shown in figure 4-2c exhibiting excellent cycling stability. Figure 4-2d shows data of a rate test for which the current density was increased from 0.1 mA/cm^2 to 2 mA/cm^2. The rate test was concluded returning to 0.1 mA/cm^2 resulting in the same capacity as during the first cycles at 0.1 mA/cm^2, confirming that the electrodes do not degrade. While both electrodes are able to retrieve 100% of the initial capacity at 0.1 mA/cm^2, this value drops to 81% for the Fe-FeCl$_2$ and to 41% for the Ni-NiCl$_2$ electrode at 2 mA/cm^2. Thus, the rate test confirms a significantly higher rate capability of the Fe-FeCl$_2$ electrode compared to the Ni-NiCl$_2$ electrode.
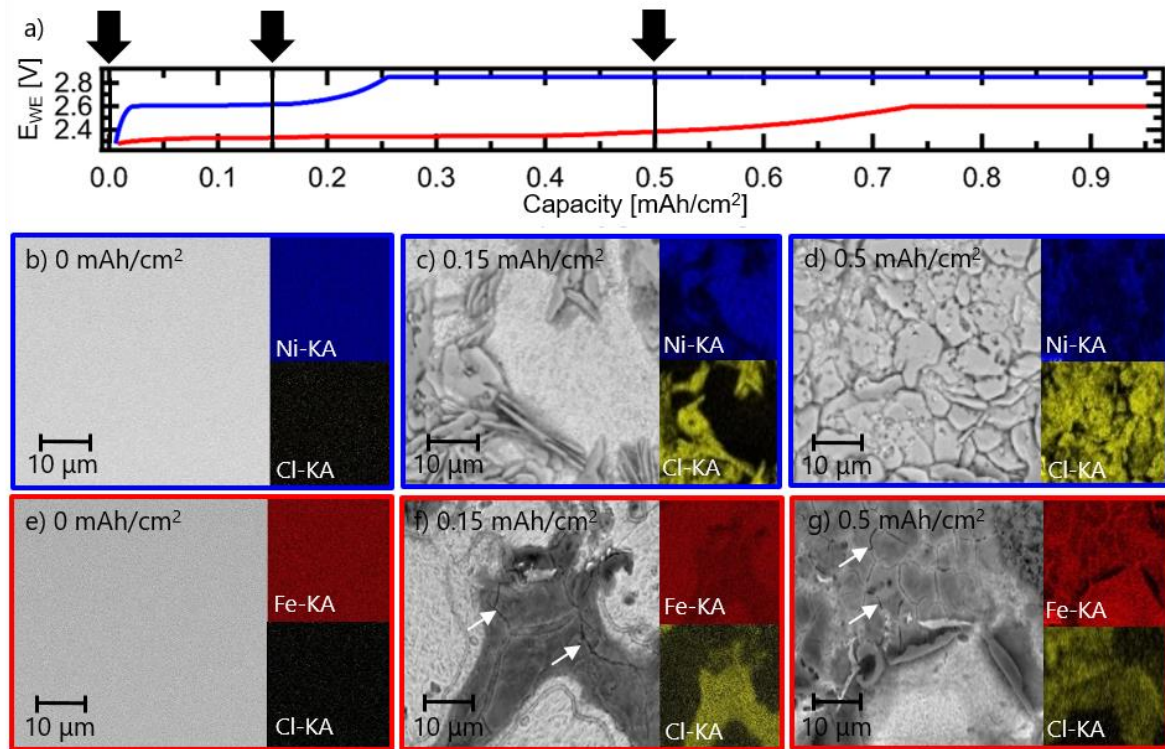
Figure 4-3: Post-mortem analysis of Ni-NiCl₂ and Fe-FeCl₂ electrodes at different degrees of chlorination, after three cycles at 0.5 mA/cm² and 300 °C. a) Charge curve for Ni-NiCl₂ (blue) and Fe-FeCl₂ (red) with arrows indicating the corresponding capacity at which the SEM images was taken. b) Pristine Ni electrode. c) Ni-NiCl₂ electrode at 0.15 mAh/cm². d) Ni-NiCl₂ electrode at 0.5 mAh/cm². e) Pristine Fe electrode. f) Fe-FeCl₂ electrode at 0.15 mAh/cm². g) Fe-FeCl₂ electrode at 0.5 mAh/cm².

Figure 4-3 links the electrochemical behavior of the Ni-NiCl₂ and Fe-FeCl₂ electrodes at a current density of 0.5 mA/cm² to the corresponding surface morphology and composition at different degrees of chlorination. We performed scanning electron microscopy (SEM) and energy-dispersive x-ray spectroscopy (EDS) mapping on electrodes extracted from disassembled cells after NaAlCl₄ removal. Figure 4-3a shows the cell voltage of Na/Ni-NiCl₂ and Na/Fe-FeCl₂ cells during charge at 0.5 mA/cm², with arrows indicating the capacity at which the SEM images were taken.

Comparison of figure 4-3b and 4-3c shows that chlorination of the pristine, smoothly polished nickel electrode leads to immediate surface roughening already at 0.15 mAh/cm². At this stage of chlorination, the surface of the nickel electrode features thin crystalline NiCl₂ platelets (length 10-20 µm, thickness ~1 µm), consistent with the layered structure of the R-3m space group,[31] growing out of the electrode surface. The presence of crystalline NiCl₂ is confirmed by the X-ray diffraction (XRD) pattern of the Ni-NiCl₂ electrode shown in figure 4-8. Thus, NiCl₂ does not form in a conformal, core-shell-style layer on the nickel electrode, but segregates out of the electrolyte when the concentration of nickel-ions exceeds to solubility limit in the molten NaAlCl₄. At this degree of chlorination, the NiCl₂ crystals do not

yet fully cover the surface of the nickel electrode (~50% surface coverage) as confirmed by the EDS maps in the inset. Full surface coverage is observed at 0.5 mAh/cm^2 shown in figure 4-3d. Upon discharge, $NiCl_2$ crystals dissolve into the $NaAlCl_4$ electrolyte while nickel-ions are plated back onto the electrode surface resulting in a granular surface morphology with a typical feature size on the order of 1 μm (not shown).[32] As the chlorine ion concentration in the $NaAlCl_4$ exceeds the solubility limit, NaCl crystals are segregated out of solution and sediment on the nickel electrode surface (not shown).

The evolution of the iron electrode upon chlorination is shown in figure 4-3e-g. In contrast to the nickel electrode, no $FeCl_2$ platelets are observed on the iron electrode surface. Instead, we observe a uniform $FeCl_2$ conversion layer and a number of cracks on the electrode surface (white arrows in figure 4-3f and g). The lower crystallinity is supported by the XRD pattern of the Fe-$FeCl_2$ electrode, showing broader $FeCl_2$ peaks with lower signal to background ratio than those for Ni-$NiCl_2$ electrode (figure 4-9). After chlorination to 0.5 mAh/cm^2, most of the iron electrode surface is converted to $FeCl_2$, but along the cracks there are still areas with non-converted iron apparent in EDS maps of the iron electrode. These cracks in the iron electrode may form due to the build-up of stress caused by the formation of the $FeCl_2$ layer.
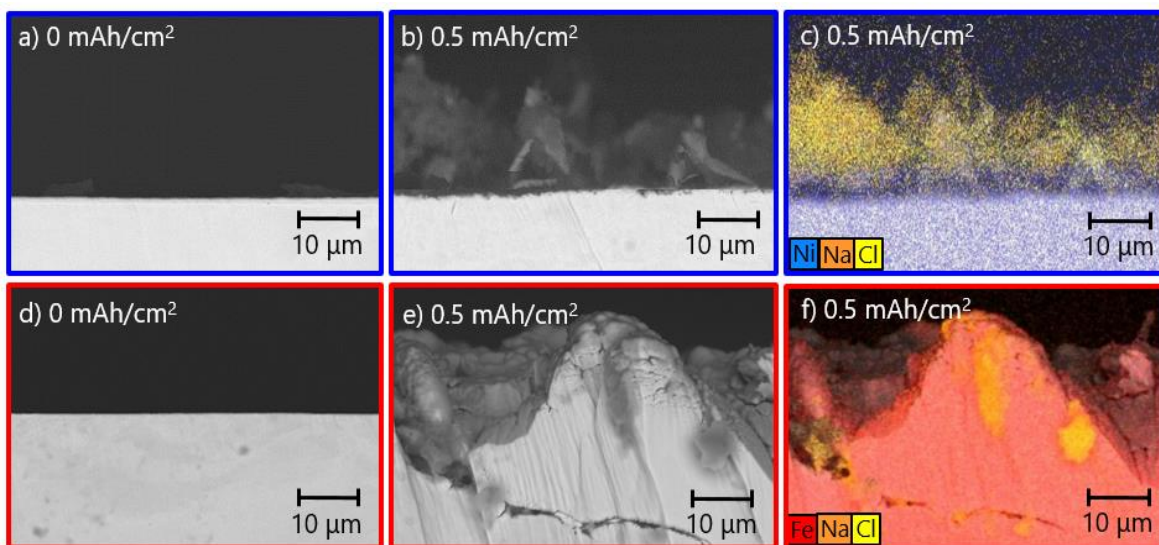
Figure 4-4: SEM images and EDS maps of ion-milled cross-sections of Ni-NiCl$_2$ and Fe-FeCl$_2$ electrodes. a) Pristine nickel electrode. b) Ni-NiCl$_2$ electrode at 0.5 mAh/cm^2. c) EDS map of Ni-NiCl$_2$ electrode at 0.5 mAh/cm^2. d) Pristine iron electrode. e) Fe-FeCl$_2$ electrode at 0.15 mAh/cm^2. f) EDS map of Fe-FeCl$_2$ electrode at 0.5 mAh/cm^2.

To confirm this hypothesis, we further investigated the chlorination behavior of the Ni-NiCl$_2$ and Fe-FeCl$_2$ electrode by imaging ion-milled cross-sections of the pristine and chlorinated electrodes shown in figure 4-4. After chlorination to 0.5 mAh/cm^2, the Ni-NiCl$_2$ electrode maintains a relatively planar nickel surface with a surface roughness < 1 μm, but

grows a > 10 μm thick layer of randomly oriented $NiCl_2$ platelets on top. The EDS map in figure 4-4c indicates that chlorination does not take place in the bulk of the nickel electrode. Separated Ni, Na, and Cl EDS maps can be found in figure 4-10 in the supplementary information. The situation is completely different for the $Fe-FeCl_2$ electrode, which exhibits a very rough electrode surface after chlorination to 0.5 mAh/cm^2 with long cracks, penetrating deep into the electrode bulk. The EDS map in figure 4-4f confirms that chlorination does not take place in the bulk of the iron electrode, but consumes the iron electrode along the cracks leading also to the cracking off of larger iron pieces. This explains the poor cycling stability observed for $Na/Fe-FeCl_2$ cells with porous electrodes, as electrode pulverization causes a loss of electronic contact of active electrode material to the current collector.[17,27] Separated Fe, Na, and Cl EDS maps can be found in figure 4-11 in the supplementary information.

In summary, our analysis shows that chlorination of the nickel electrode proceeds via uniform oxidation of nickel and the formation of $NiCl_2$ platelets (figure 4-5a-c). In contrast, the chlorination of the iron electrodes proceeds via stress-induced cracking, resulting in non-uniform iron oxidation and the pulverization of the iron electrode (see figure 4-5d-f). Stress-induced corrosion is a classical scenario, described also for many other electrode/electrolyte systems.[33–35] Our analysis explains the faster dis-/charge kinetics and higher rate capability observed for the iron electrode in figure 4-1d and 4-2d as crack formation 'supplies' continuously fresh iron surface for chlorination as shown in figure 4-5e, f).
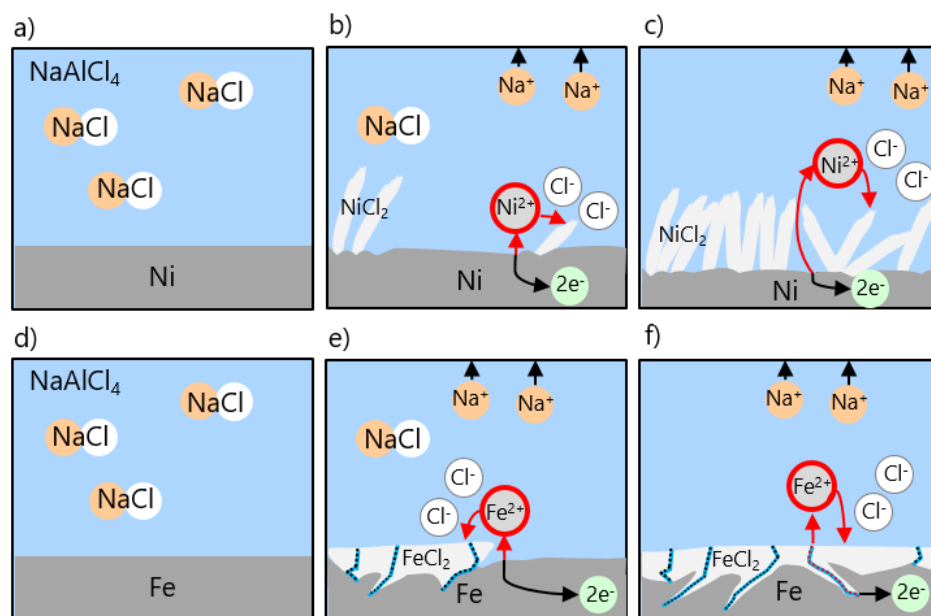
Figure 4-5: Sketch comparing chlorination of (a-c) nickel and (d-f) iron electrode at 0, 0.15, 0.5 mA/cm^2 state of charge.

Our results further demonstrate that metal-ion diffusion and metal-ion solubility in the molten $NaAlCl_4$ electrolyte rather than transport across the metal chloride layer are limiting the rate capability of planar nickel and iron electrodes.[24] This has important implications

for the design of porous high-capacity electrodes. Increasing the mobility of metal ions improves peak current density only as the square root of the diffusion coefficient. It is thus more effective to increase metal-ion solubility in the molten $NaAlCl_4$ electrolyte, which improves peak current density linearly. However, increasing the metal-ion solubility also leads to more rapid dissolution of the oxidized electrode, which can lead to a breakdown of the electronic backbone of the porous electrode and accelerate capacity fading due to loss of electronic contact of a fraction of the active electrode material to the current collector. Note that this phenomenon is independent of crack-induced electrode pulverization, which represents an additional mechanism responsible for capacity fading in iron electrodes.

Metal-ion diffusion and solubility become important, when the path for sodium-ions is short and does not dominate the cell resistance and does not limit the current density. On charge, this is the case at low state of charge in porous electrodes, when the (oxidation) reaction front is situated in the vicinity of the Na-β"-alumina electrolyte. As the reaction fronts proceeds away from the Na-β"-alumina electrolyte during charging, the path length for sodium-ions is increasing and consequently reaches a point, where the resistance contribution associated with the sodium-ion transport will limit the current density. The effective path length for sodium-ions strongly depends on the microstructure of the porous electrode (porosity, tortuosity, etc.). When designing the microstructure of a porous electrode, it is also important to take into account how the initial microstructure evolves during cycling (e.g. platelet vs crack formation). A multi-physics model based on an exact geometrical representation of the porous electrode would allow the design of tailored microstructures for different electrode compositions and dis-/charge profiles.

On discharge, metal ions are plated onto the electrode. In principle, plating can result in local depletion of metal ions in the electrolyte, if metal chloride dissolution is not fast enough. However, because the values extracted from figure 4-1c and d for the diffusion coefficients are comparable for oxidation and reduction, we conclude that the limiting factor is metal-ion diffusion in the molten $NaAlCl_4$ electrolyte rather than the rate of metal chloride dissolution.

Commercial sodium-metal chloride batteries employ a combination of nickel and iron in the positive electrode to circumvent sodium-ion transport limitations in the porous positive electrode, especially under pulsed current load. From our analysis we can further conclude that addition of iron is useful to enhance the battery's rate capability by adding faster iron-ion diffusion to the slower nickel-ion diffusion. This is especially relevant at low state of charge when charging and high state of charge when discharging, when the reaction front is located in the vicinity of the Na-β"-alumina electrolyte, and no sodium-ion limitation is expected.

4.3 Conclusion

In summary, we reinvestigated de-/chlorination of planar Ni-NiCl$_2$ and Fe-FeCl$_2$ electrodes in molten NaAlCl$_4$ electrolyte. Despite the larger diffusion coefficient of nickel-ions compared to iron-ions in NaAlCl$_4$, we observed a higher rate capability for the Fe-FeCl$_2$ electrode compared to the Ni-NiCl$_2$ electrode, which can be explained by the higher solubility of iron-ions in NaAlCl$_4$ and stress-induced crack formation in the iron electrode, continuously 'supplying' fresh iron for chlorination. However, both factors also tend to accelerate capacity fading. We also observed that the nickel electrode is consumed uniformly and NiCl$_2$ growth in platelets, while the iron electrode is consumed non-uniformly and FeCl$_2$ growth as a layer.

Mechanistic insights into the de-/chlorination of Ni-NiCl$_2$ and Fe-FeCl$_2$ electrodes gained in this study allow the design of improved positive electrodes with reduced charge and discharge times and therefore the competition with state-of-the-art lithium-ion batteries. This may hold the key for the breakthrough of sodium-nickel-chloride batteries for large-scale electricity storage.

4.4 Methods

A sketch and photographs of the self-built high-temperature cell used in the experiments are shown in figure 4-6 Na-β"-alumina disks with a thickness of 1 mm and 35 mm diameter were sintered at 1600 °C for 5 min from powders following ref. 36 and glued to two α-alumina rings using a glass paste. To prevent dewetting of liquid sodium from the Na-β"-alumina surface on the negative electrode, a porous carbon coating was applied following the procedure described in ref. 14. For the positive electrode 20 mm diameter nickel (Ni201, 99.2%) and iron (Armco, 99.85%) were first polished (P2500, P4000) in isopropanol and then in inert argon atmosphere (P4000). 300 mg sodium NaAlCl$_4$ (Sigma Aldrich, 99.99%) and 10 mg NaCl (JuraSel, 99.8%) powders have been mixed to ensure NaCl saturation of the NaAlCl$_4$ at all times. Full cells with an active area of 3.14 cm^2 were assembled in an argon-filled glovebox. A type K thermocouple was inserted at the interface between α-alumina and Na-β"-alumina for precise temperature determination. Sodium metal foils with a purity of 99.9% and an area specific mass of 0.16 g/cm^2 (0.5 g) were inserted at the negative electrode.

Cell heating for all experiments was realized via a resistive coil heater embedded in a self-built glass fibre heating jacket. All experiments have been conducted at 300 °C, while cell temperature was controlled via a feed-forward controller. Cell cycling was conducted in a glovebox under argon atmosphere with H$_2$O and O$_2$ levels below 0.1 ppm. For cyclic voltammetry measurements each cell passed one sweep at each voltage scan rate for run-in. For galvanostatic measurements prior to electrochemical and post-mortem analysis, each cell passed three run-in cycles with the corresponding area specific capacity (0.15, 0.5, 0.95

mAh/cm^2) at 0.5 mAh/cm^2 with an upper cut-off voltage at 2.85 V vs. Na/Na$^+$ for nickel, 2.6 V vs. Na/Na$^+$, 0.05 mA/cm^2 and a lower cut-off voltage of 1.8 V, 0.05 mA/cm^2. During rate tests, the cells were charged (chlorinated) at 0.5 mA/cm^2 up to 0.15 mAh/cm^2 and discharged (de-chlorinated) in the range of 0.1-2 mA/cm^2. All cells were cycled with a Biologic VSP 3e potentiostat.

Scanning electron microscopy images (SEM) and energy-dispersive x-ray spectroscopy (EDS) maps were taken after cell disassembly and removal of sodium tetrachloroaluminate (NaAlCl$_4$) in isopropanol with a table top Hitachi TM3030Plus. X-ray diffraction patterns were taken with a PANanalytical X`Pert PRO MRD. Cross sections of the electrodes were prepared by sawing and ion polishing employing a Hitachi IM4000 Plus ion miller.

Acknowledgements

4.5   Supporting information
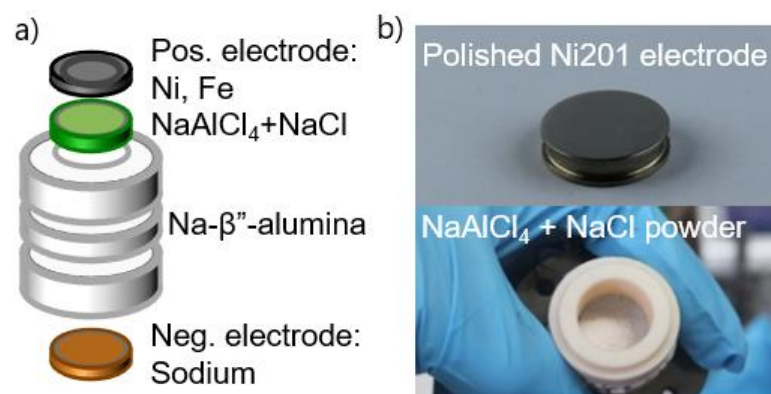
Figure 4-6: Electrochemical cell. a) Schematic image of cell. b) Image of pristine, polished nickel electrode and cell assembly filled with NaCl and TCA powder.
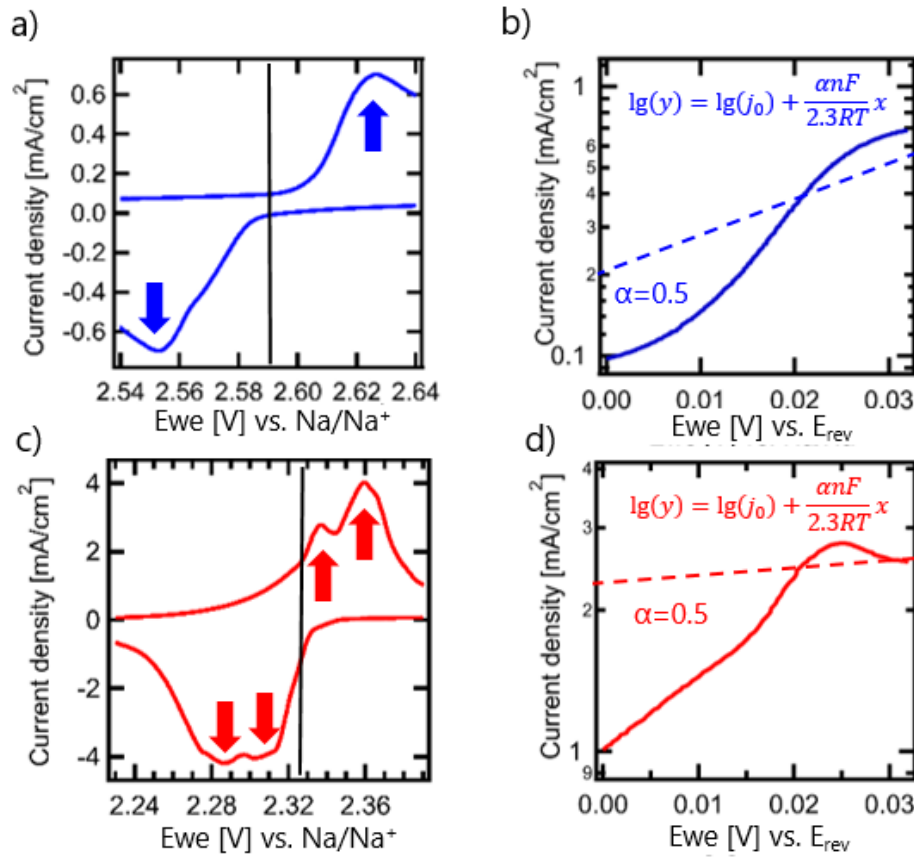
Figure 4-7: Cyclic voltammetry results at 0.1 mV/s for Ni-NiCl₂ (blue) and Fe-FeCl₂ (red). a) Current response of Na/Ni-NiCl₂ cell with single peaks upon oxidation and reduction with a reversible potential of E_{rev}= 2.59 V vs. Na/Na⁺ at 300°C. b) Tafel-plot for Ni-NiCl₂ electrode with a reversible potential (E_{rev}) of 2.59 V vs. Na/Na⁺. The dashed line represents an anodic transfer coefficient of 0.5 resulting in an exchange current density on the order of ~ 0.2 mA/cm² c) Current response of Na/Fe-FeCl₂ cell with two peaks upon oxidation and reduction with a reversible potential of E_{rev}= 2.33 V vs. Na/Na⁺ at 300°C. b) Tafel-plot for Fe-FeCl₂ electrode with a reversible potential (E_{rev}) of 2.33 V vs. Na/Na⁺. The dashed line represents an anodic transfer coefficient of 0.5 resulting in an exchange current density of about ~ 2 mA/cm².

Calculation of diffusion constants:
From Faulkner & Bard (pp.231)[28]:

$$i_{peak} = 0.4463(\frac{F^3}{RT})^{1/2}n^{\frac{3}{2}}AD_0^{\frac{1}{2}}c_0v^{\frac{1}{2}}$$

$$j_{peak} = (0.4463(\frac{F^3}{RT})^{1/2}n^{\frac{3}{2}}D_0^{\frac{1}{2}}c_0) \cdot v^{\frac{1}{2}}$$

$$j_{peak} \propto |a| \cdot v^{\frac{1}{2}} ; |a| = \left(0.4463\left(\frac{F^3}{RT}\right)^{\frac{1}{2}}n^{\frac{3}{2}}D_0^{\frac{1}{2}}c_0\right) \rightarrow D_0 = \left(\frac{|a|}{0.4463\left(\frac{F^3}{RT}\right)^{\frac{1}{2}}n^{\frac{3}{2}}c_0}\right)^2$$

i_{peak}: Peak current [A]

j_{peak}: Peak current density [A/cm^2]

F: Faraday constant: 96485 [C/mol]

R: Universal gas constant: 8.314 [J/mol K]

T: Temperature: 573.15 [K]

n: number of electrons involved: 2 [-]

D_0: Diffusion constant: [cm^2/s]

c_0: initial concentration[27, 29, 30]: $c_{0,Ni2+}$ = 2.1544 e-6 [mol/cm^3]; $c_{0,Fe2+}$ = 1.9998 e-4 [mol/cm^3]: $\rho_{TCA,300°C}$=1.59985 g/cm^3

v: scan rate: 0.0001-0.010 [V/s]

a: slope from Randles-Sevcik plot: a_{NiCl2} = $[\frac{A}{cm^2}(\frac{V}{s})^{-1/2}]$

$a_{Ni,ox}$:=0.056 $\frac{A}{cm^2}(\frac{V}{s})^{-1/2}$

$a_{Ni,red}$:=-0.052 $\frac{A}{cm^2}(\frac{V}{s})^{-1/2}$

$a_{Fe,ox}$:=0.378 $\frac{A}{cm^2}(\frac{V}{s})^{-1/2}$ (fit for first 3 points)

$a_{Fe,red}$:=-0.295 $\frac{A}{cm^2}(\frac{V}{s})^{-1/2}$ (fit for first 3 points)
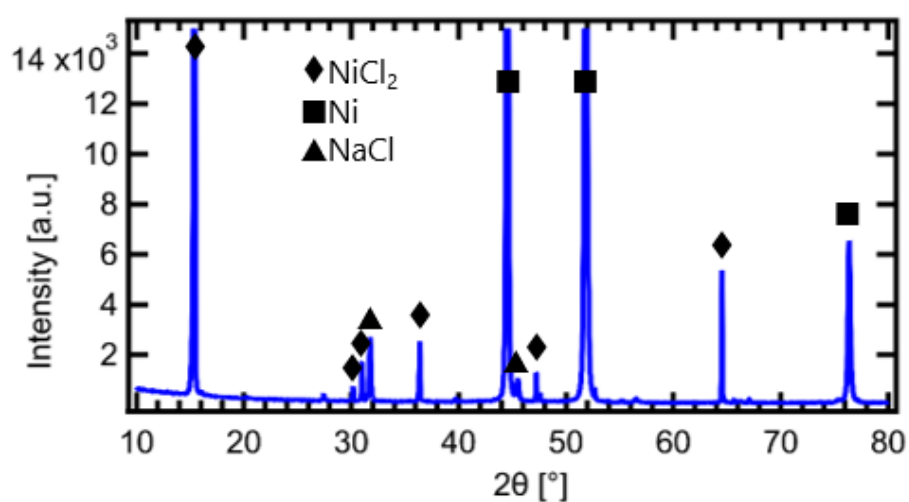
Figure 4-8: XRD pattern of Ni-NiCl₂ electrode at 0.5 mAh/cm² showing the presence of NaCl, Ni and crystalline NiCl₂.
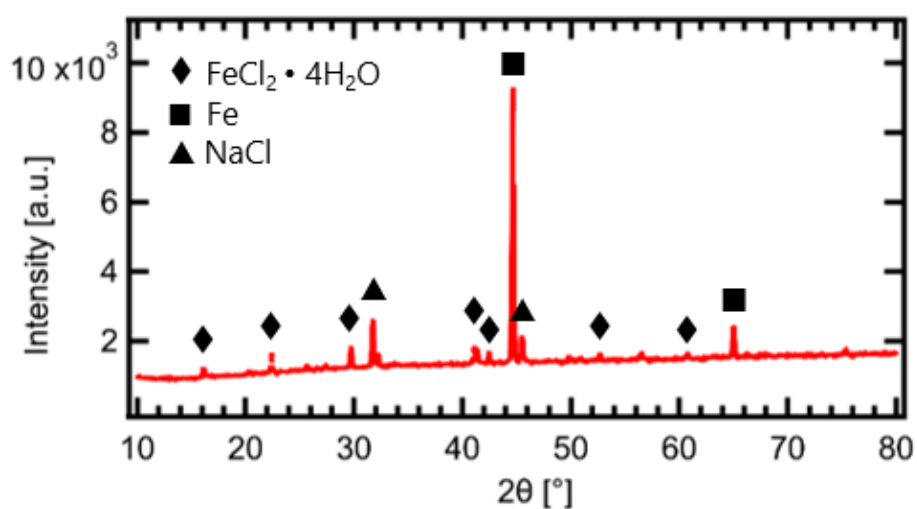
Figure 4-9: XRD pattern of Fe-FeCl₂ electrode at 0.5 mAh/cm² showing the presence of NaCl, Fe and amorphous, less-crystalline FeCl₂ · 4H₂O.
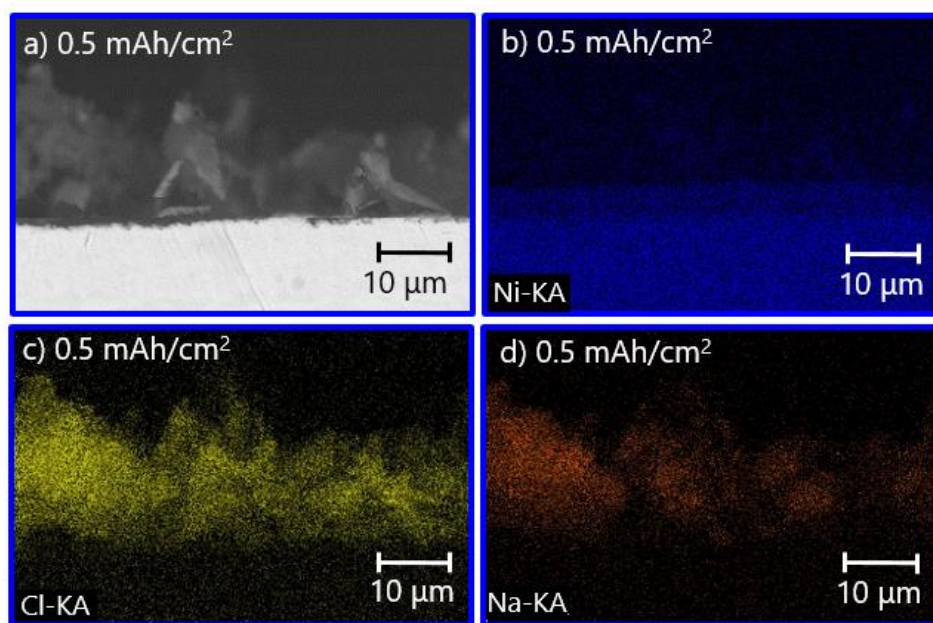
Figure 4-10: SEM image and EDS maps of ion-milled cross-sections of Ni-NiCl$_2$ electrode at 0.5 mAh/cm^2. a) SEM image. b) EDS Ni-KA. c) EDS Cl-KA. d) EDS Na-KA.
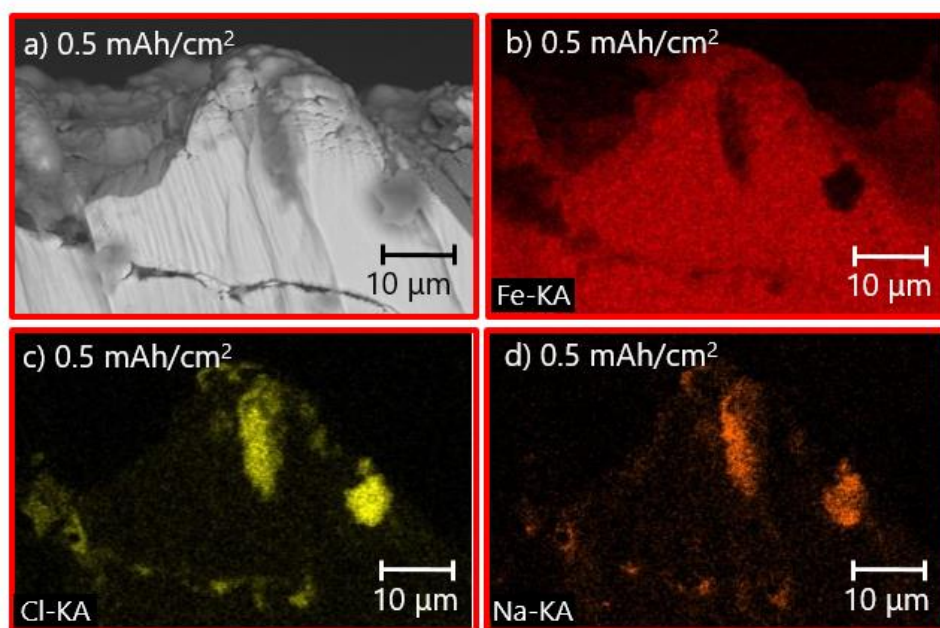
Figure 4-11: SEM image and EDS maps of ion-milled cross-sections of Fe-FeCl$_2$ electrode at 0.5 mAh/cm^2. a) SEM image. b) EDS Fe-KA. c) EDS Cl-KA. d) EDS Na-KA.

References

[1]   J. Coetzer, *A new high energy density battery system*, J. Power Sources, 1986, *18*, 377.

[2]   J. Coetzer, M. M. Thackeray, Patent: *Cathode for an electrochemical cell and an electrochemical cell*, US 4288506, 1978.

[3]   J. L. Sudworth, *Zebra batteries*, J. Power Sources, 1994, *51*, 105.

[4]   J. L. Sudworth, *The sodium/nickel chloride (ZEBRA) battery*, J. Power Sources, 2001, *100*, 149.

[5]   R. Benato, N. Cosciani, G. Crugnola, S. Dambone, G. Lodi, C. Parmeggiani, M. Todeschini, *Sodium-nickel-chloride battery technology for large-scale stationary storage in the high voltage network*, J. Power Sources, 2015, *293*, 127.

[6]   G. Li, X. Lu, J. Y. Kim, V. V Viswanathan, K. D. Meinhardt, M. H. Engelhard, V. L. Sprenkle, *An advanced Na − FeCl$_2$ ZEBRA battery for stationary energy storage application*, Adv. Energy Mater., 2015, *5*, 1.

[7]   X. Lu, G. Li, J. Y. Kim, D. Mei, J. P. Lemmon, V. L. Sprenkle, J. Liu, *Liquid-metal electrode to enable ultra-low temperature sodium-beta alumina batteries for renewable energy storage*, Nat. Commun., 2014, *5*, 1.

[8]   G. Li, X. Lu, J. Y. Kim, K. D. Meinhardt, H. J. Chang, N. L. Canfield, V. L. Sprenkle, *Advanced intermediate temperature sodium–nickel chloride batteries with ultra-high energy density*, Nat. Commun., 2016, *7*, 1.

[9]   C. H. Dustmann, *Advances in ZEBRA batteries*, J. Power Sources, 2004, *127*, 85.

[10]   R. Benato, S. D. Sessa, G. Crugnola, M. Todeschini, N. Zanon, S. Zin, *Sodium-nickel-chloride (Na-NiCl$_2$) battery safety tests for stationary electrochemical energy storage,* 2016 AEIT International Annual Conference, AEIT, 2016, pp. 1–5.

[11]   R. Manzoni, *Sodium-nickel-chloride batteries in transportation applications*, 2015 International Conference on Electrical Systems for Aircraft, Railway, Ship Propulsion and Road Vehicles (ESARS), IEEE, 2015, pp. 1–6.

[12]   D. Trickett, Report: *Current status of health and safety issues of sodium / metal chloride (ZEBRA) batteries*, 1998, URL: https://www.osti.gov/servlets/purl/7101, Date accessed: 3 Spetember, 2021.

[13]   V. Zinth, J. E. Soc, V. Zinth, M. Schulz, S. Seidlmayer, N. Zanon, R. Gilles, M. Hofmann, *Neutron tomography and radiography on a sodium-metal-halide cell under operating conditions*, J. Electrochem. Soc., 2016, *163*.

[14]   D. Landmann, G. Graeber, S. Haussener, C. Battaglia, *Sodium plating and stripping from Na-β"-alumina ceramics beyond 1000 mA/cm2*, Mater. Today Energy, 2020, *18,* 100515.

[15]   R. J. Bones, J. Coetzer, R. C. Galloway, D. A. Teagle, *A sodium / iron (II) chloride cell with a beta alumina electrolyte*, J. Electrochem. Soc., 1987, *134*, 2379.

[16]   G. Graeber, D. Landmann, E. Svaluto-ferro, F. Vagliani, D. Basso, A. Turconi, M. V. F. Heinz, C. Battaglia, *Rational cathode design for high-power sodium-metal chloride batteries*, Adv. Funct. Mater., 2021, *2106367*.

[17]   B. V Ratnakumar, S. Di Stefano, G. Halpert, *Electrochemistry of metal chloride cathodes in sodium batteries*, J. Electrochem. Soc., 1990, *137*, 2991.

[18]   V. Zinth, J. E. Soc, V. Zinth, S. Seidlmayer, N. Zanon, G. Crugnola, M. Schulz, R. Gilles, M. Hofmann, *In situ spatially resolved neutron diffraction of a sodium-metal-halide battery*, J. Electrochem. Soc., 2015, *162*.

[19]   FZ SoNick SA, FZSoNick TL range data sheet, URL: https://www.fzsonick.com/applications, Date accessed: 6.9.2021

[20]   H. Li, *Practical evaluation of Li-Ion batteries*, Joule, 2019, *3*, 911.

[21]   J. Prakash, L. Redey, D. R. Vissers, *Morphological considerations of the nickel chloride electrodes for zebra batteries*, J. Power Sources, 1999, *84*, 63.

[22]   S. E. Rock, D. E. Simpson, M. C. Turk, J. T. Rijssenbeek, G. D. Zappi, D. Roy, *Nucleation controlled mechanism of cathode discharge in a Ni / NiCl2 molten salt half-cell battery*, J. Electrochem. Soc., 2016, *163*, 2282.

[23]   J. Prakash, L. Redey, D. R. Vissers, *Electrochemical behavior of nonporous Ni/NiCl$_2$ electrodes in chloroaluminate melts*, J. Electrochem. Soc., 2000, *147*, 502.

[24]   X. Zhan, M. E. Bowden, X. Lu, J. F. Bonnett, T. Lemmon, D. M. Reed, V. L. Sprenkle, G. Li, *A low-cost durable Na-FeCl$_2$ battery with ultrahigh rate capability*, Adv. Energy Mater., 2020, *10*, 1.

[25]   C. H. Dustmann, *ZEBRA battery meets USABC goals*, J. Power Sources, 1998, *72*, 27.

[26]   C. H. Hamann, W. Vielstrich, *Elektrochmie*, ISBN: 3-527-31066-5, Wiley, Weinheim, 2004.

[27]   J. L. Coetzer, G. D. Wald, S. W. Orchard, *Mechanism of the cathode reaction in sodium-ferrous chloride secondary cells*, J. Appl. Electrochem., 1993, *23*, 790.

[28]   L. R. Faulkner, A. J. Bard, *Electrochemical methods fundamentals and applications*, ISBN: 0-471-04372-9, Wiley, 2001.

[29]   M. G. Macmillan, B. Cleaver, *Solubility of nickel chloride in molten sodium tetrachloroaluminate saturated with sodium chloride over the temperature range*, J. Chem. Soc. Faraday Trans., 1993, *89*, 3817.

[30]   R. W. Berg, H. A. Hjuler, J. Niels, *Density of molten NaAlCl4 a reinvestigation*, J. Chem. Eng. Data, 1983, *28*, 251.

[31]   A. Ferrari, A. Braibanti, G. Bigliardi, *Refinement of the crystal structure of NiCl$_2$ and of unit-cell parameters of some anhydrous chlorides of divalent metals*, Acta Crystallogr., 1963, *16*, 846.

[32]   K. Ando, N. Tachikawa, N. Serizawa, Y. Katayama, *Electrochemical behavior of a Ni chlorocomplex in a Lewis basic ionic liquid containing chloride ion*, J. Electrochem. Soc., 2020, *167*.

[33]   J. Flis, M. Ziomek-Moroz, *Effect of carbon on stress corrosion cracking and anodic oxidation of iron in NaOH solutions*, Corros. Sci., 2008, *50*, 1726.

[34]   A. Kawashima, H. Koji, T. Masumoto, *Stress corrosion cracking of amorphous iron base alloys*, Corros. Sci., 1976, *16*, 935.

[35]   D. A. Vermilyea, *Stress corrosion cracking of iron and nickel base alloys in sulfate solution at 289 °C*, Corros. NACE, 1973, *29*, 442.

[36]   M. Bay, M. V. F. Heinz, R. Figi, C. Schreiner, D. Basso, N. Zanon, U. F. Vogt, C. Battaglia, *Impact of liquid phase formation on microstructure and conductivity of Li-stabilized Na-β''-alumina ceramics*, ACS Appl. Energy Mater., 2018, *2*, 687.

5. Rational cathode design for high-power sodium-metal-chloride batteries[*]

Having understood the rate-limiting processes and fundamental de-/chlorination mechanism of planar nickel and iron electrodes, as presented in chapter 4, we investigate here the rate-limiting processes of a nickel-nickel-chloride porous positive electrode. Different electrode compositions with nickel/iron and pure nickel are probed in rate tests.

Author contributions:

G.G. conceived the idea for this study and designed the experiments together with D.L., M.H., and C.B. E.S. prepared most of the Na-β"-alumina electrolytes for the experiments. D.L. designed the electrochemical cell. F.V prepared the Ni/Fe and Ni granules used in this study. G.G. performed the experiments with porous electrodes. G.G. analyzed the data, prepared the figures, and wrote the manuscript. D.L., M.H., D.B., A.T., and C.B. critically reviewed and edited the manuscript. All coauthors read, commented, and approved the final manuscript.

Abstract

The transition from fossil fuels to renewable energy sources requires economic, high-performance electrochemical energy storage. High-temperature sodium-metal chloride batteries combine long cycle and calendar life, with high specific energy, no self-discharge, and minimum maintenance requirements, while employing abundant raw materials. However, large-scale deployment in mobility and stationary storage applications is currently hindered by high production cost of the complex, commercial tubular cells and limited rate capability. The present study introduces sodium-metal chloride cells with a simple, planar architecture that provide high specific power while maintaining the inherent high specific energy. Rational cathode design, considering critical transport processes and the effect of cathode composition on the cell resistance, enables the development of high-performance cells with average discharge power of 1022 W kg^{-1} and discharge energy per cycle of 258 Wh kg^{-1} on cathode composite level, shown over 140 cycles at an areal capacity of 50 mAh cm^{-2}. This corresponds to a 3.2C discharge over 80% of full charge. Compared to the best performing planar sodium-metal chloride cells with similar cycling stability and mass loading in the literature, the presented performance represents an increase in specific power by more than a factor of four, while also raising the specific energy by 74%.

5.1 Introduction

Transition from fossil fuels to renewable energy sources is imperative to reduce greenhouse gas emissions. Integrating renewable power generation based on solar and wind energy into the electricity grid requires scalable stationary energy storage solutions to match electricity production and demand. Similarly, for mobile applications, high-performance energy storage is required to provide alternatives for internal combustion engines burning fossil fuel.

High-temperature sodium-metal chloride batteries, also referred to as molten-salt batteries or Zebra batteries, are an excellent candidate for stationary energy storage since they provide long cycle and calendar life, require no maintenance, and employ abundant, non-critical raw materials without the need of Li or Co.[1–3] In principle, these qualities make them competitive with existing technologies such as lithium-ion or sodium-ion technology.[4,5] However, large-scale deployment of sodium-metal chloride batteries is currently hindered by high production cost of the commercial tubular cells. Therefore, in the present work, we study sodium-metal chloride cells with a planar architecture. A transition from the commercial tubular design toward a planar cell design can reduce complexity in cell manufacturing and drastically lower assembly cost, making the sodium-metal chloride technology economically favorable to a wider range of applications, while it also poses mechanical design challenges.[6] The feasibility of a planar cell design has been demonstrated for the past 15 years in numerous scientific publications.[7–19] Beyond these important considerations on the cell design (tubular vs. planar), it is the cathode composition and microstructure that is critical to the performance of a sodium-metal chloride cell. In contrast to lithium-ion batteries, which employ relatively thin electrodes (typically up to 100 μm),[20,21] sodium-metal chloride batteries apply a cathode with considerable thickness (few millimeters), which gives rise to an increasingly important cell resistance contribution as the electrochemical reaction front progresses through the thickness of the cathode.[2] As active cathode materials, previous studies on planar cell designs mostly focused on pure Ni cathodes and pure Fe cathodes,[7–19] steadily increasing the specific energy, reaching up to 405 Wh kg^{-1} on cathode composite level,[16] and prolonging cycle life up to 1000 cycles.[18] In further studies it was shown that the introduction of a mixed Fe/Ni cathode, where both Fe and Ni contribute to the cell capacity, can increase the power capability compared to cells with a pure Ni cathode.[2,22,23] Multiple reasons support the use of mixed Fe/Ni cathodes, with the overall idea of combining the advantages of both metals. While Ni provides a higher equilibrium potential, Fe is considerably cheaper than Ni, improving the economic competitiveness of sodium-metal chloride cells. Furthermore, it is known that the reaction kinetics of Fe are faster than Ni in sodium-metal chloride cells.[11] Finally, a mixed Fe/Ni cathode provides two possible electrochemical reactions that can be executed in parallel, thereby stabilizing the cell voltage in case of load peaks also at low state of charge (SOC).[2] Against this background it seems not surprising that for the past 20 years a mixed Fe/Ni

cathode has been employed in commercial tubular cells.[2,24] However, our current understanding on how the cathode composition affects the cell performance remains incomplete.

Irrespective of the cathode composition, to date literature on sodium-metal chloride batteries was not able to demonstrate planar cells that simultaneously show high specific power, high specific energy, good energy efficiency, and high cycling stability. Such batteries are especially desirable for stationary energy storage in the context of grid balancing, where high power is required, or also in mobile applications including electric vehicles. Furthermore, critical insight into the electrochemically limiting cathode processes is missing, which is the key for further performance enhancement.

In the present study, we investigate how the cathode composition affects the accessible power, energy, and energy efficiency in planar sodium-metal chloride cells. We compare planar cells with Fe/Ni cathodes to cells with pure Ni cathodes, and study the effective cell resistance as a function of SOC, thereby providing a mechanistic insight into the relevant cell reactions. The cell resistance is of fundamental importance since—at a defined current—it determines the available capacity within given voltage limitations, and it directly affects the energy efficiency of the cell. With our analysis, we provide experimental evidence for a reaction front mechanism within the cathode, which was previously postulated in the literature and investigated using neutron diffraction imaging technique.[2,25–27] From our electrochemical data, we derive how the location of the cell reactions moves along the depth of the cathode, from the solid electrolyte to the current collector. Finally, we compare our cycling results to previously reported planar sodium-metal chloride cells. Thereby we show how a rational cathode design regarding composition and microstructure is guided by a mechanistic understanding of electrochemical activity of species and transport processes and provides a pathway towards substantial performance enhancements in sodium-metal chloride batteries.

5.2   Results and discussion

For the present work, we developed planar sodium-metal chloride lab cells that we cycled at 300 °C, see Figure 5-1 and the Experimental Section for details. We compared two cathode compositions, namely mixed Fe/Ni cathodes and pure Ni cathodes.
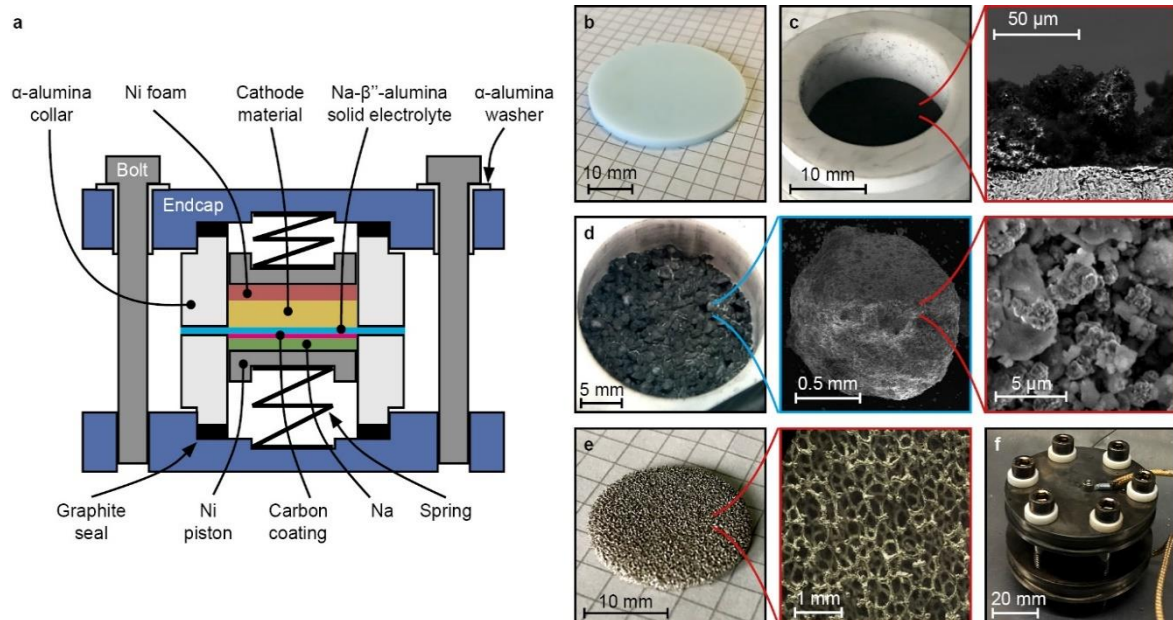
Figure 5-1: High-temperature planar sodium-metal chloride lab cell. a) Schematic, cross-sectional view. b) Photograph of a Na-β"-alumina solid electrolyte disc. c) Ceramic subassembly consisting of a Na-β"-alumina disc glued between two α-alumina collars, showing the carbon coating applied to the anode side. Inset: Cross-sectional scanning electron microscopy (SEM) image of the carbon coating (black) on the Na-β"-alumina disc (grey). d) Photograph of cathode compartment with cathode granules after NaAlCl₄-infiltration. Insets: SEM images of one cathode granule and its microstructure. e) Photograph of Ni foam serving as current collector and NaAlCl₄ reservoir in the cathode compartment. Inset: Open pore structure of the foam. f) Photograph of assembled cell. See experimental section for details.

We first discuss the performance of cells with a mixed Fe/Ni cathode. In figure 5-2a, we show the galvanostatic maiden charge of the Fe/Ni cell at 3 mA cm^{-2} (C-rate 0.05C). Analogous to previous studies, we define the theoretical capacity of the cell based on the electrochemical reactions of NaCl with the metal constituents in the cathode, namely Al, Fe and Ni. For the Fe/Ni cell, the upper cut-off voltage was fixed to 2.75 V to avoid undesired overcharge reactions (Fe + 3 NaAlCl$_4$ ⟷ FeCl$_3$ + 3 AlCl$_3$ + 3 Na at approximately 2.75 V). During maiden charge of the Fe/Ni cell, we distinguish three main reactions. Reaction 8: Oxidation of Al and formation of NaAlCl$_4$ and Na, given as:[28]

Al + 4 NaCl ⟷ NaAlCl$_4$ + 3 Na   at ~1.6 V (300 °C)   Reaction 8

This reaction is applied irreversibly in our system, taking place exclusively during maiden charge. Formation of molten $NaAlCl_4$ from NaCl at the cathode improves the distribution of $NaAlCl_4$ within the granules, leading to enhanced electrochemical activity of the cathode. We thus fix the lower cut-off voltage at 1.6 V. Since we are performing a capacity-limited cycling protocol (see details below), the upper and lower cut-off voltages are typically not reached. Based on the amount of Al in the cathode composition (see Experimental section), reaction 8 is limited to a maximum 15 mAh g^{-1}, until the entire Al content is consumed. Subsequently, in the Fe/Ni cells, reaction 9: Oxidation and chlorination of Fe is initiated:[28]

$Fe + 2\ NaCl \longleftrightarrow FeCl_2 + 2\ Na$ at 2.32 V (300 °C)   Reaction 9

Based on the amount of Fe in the Fe/Ni cathode, reaction 9 can provide a maximum of 63 mAh g^{-1}. At even higher cell voltage, we observe reaction 10: Oxidation and chlorination of Ni, given as:[2]

$Ni + 2\ NaCl \longleftrightarrow NiCl_2 + 2\ Na$ at 2.57 V (300 °C)   Reaction 10

The equilibrium potentials for reaction 9 and 10 were derived from dedicated experiments by determining the open-circuit voltage (OCV) versus SOC using a galvanostatic intermittent titration technique (GITT), refer to figure 5-8 for details.
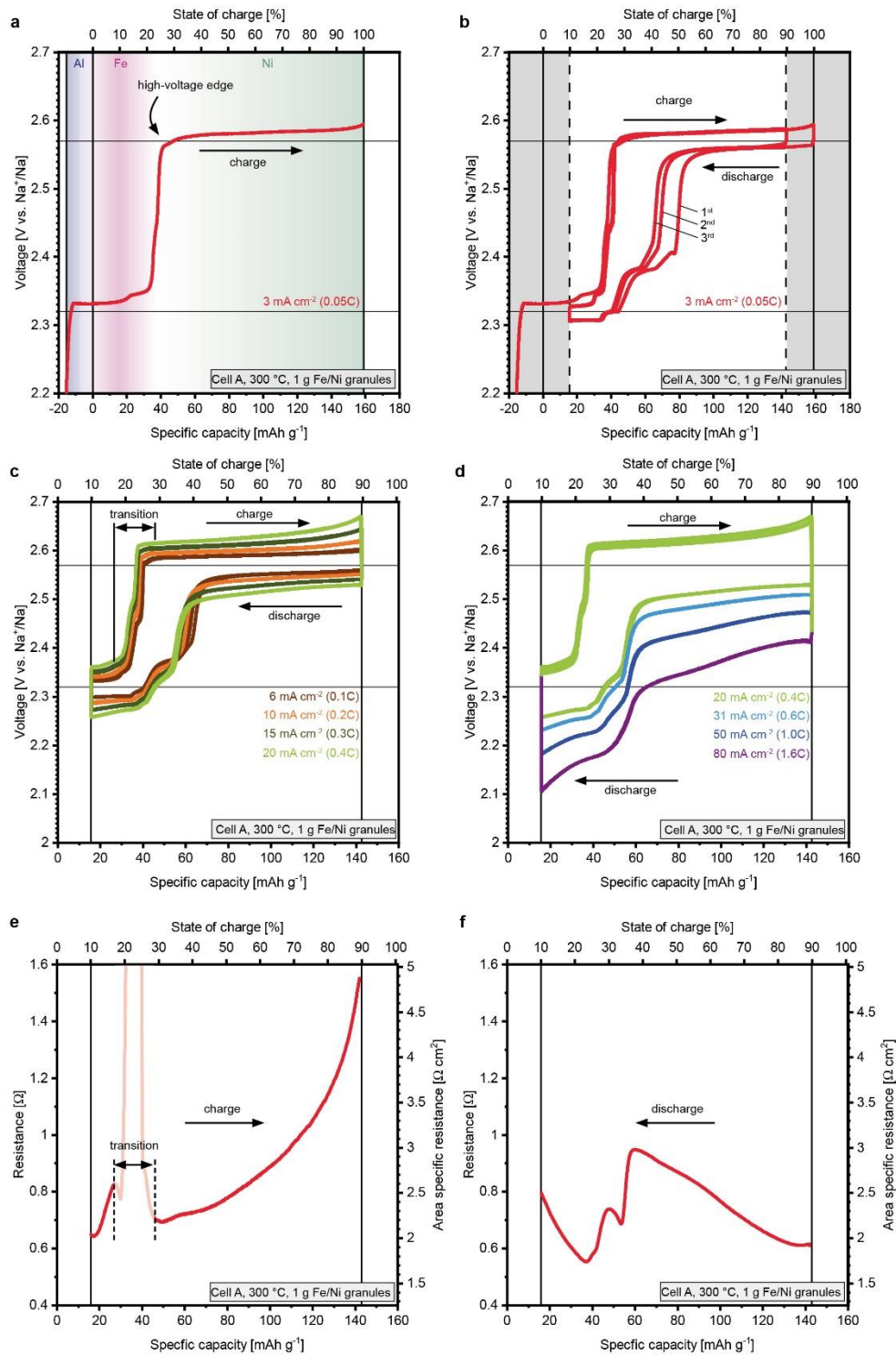
Figure 5-2: Galvanostatic cycling of planar sodium-metal chloride cells with mixed Fe/Ni cathode. a) Voltage vs. specific capacity during maiden charge, highlighting the three metal chlorination reactions (Al, Fe, and Ni). b) Voltage vs. specific capacity during the first three cycles. c) Symmetric rate test: Voltage vs. specific capacity; charge and discharge rates increase symmetrically from 6 mA cm⁻² to 20 mA cm⁻², three cycles per rate. Transition during charge from low-voltage to high-voltage plateau is highlighted. d) Discharge rate test: Voltage vs. specific capacity; charge rates are constant at 20 mA cm⁻², discharge rates increase

from 20 mA cm^{-2} to 80 mA cm^{-2}, three cycles per rate. e) Cell resistance during charge computed from charge curves in c). Within voltage transition region (15% to 30% SOC), accurate resistance computation is hindered by non-ohmic cell behavior, see figure 5-9. f) Cell resistance during discharge computed from discharge rate test in d).

In contrast to reaction 8 and 9, chlorination of Ni is not limited by the amount of Ni in the cathode. Instead, it is limited by the availability of NaCl in the cathode granules. Considering the amounts of NaCl consumed during reaction 8 and reaction 9 in the Fe/Ni cells, a capacity of 95 mAh g^{-1} is expected from Ni chlorination, before the entire NaCl content in the cathode granules is consumed. We consider the 15 mAh g^{-1} from reaction 8 as irreversible in our experiments, and assign it with negative values within the SOC window – see figure 5-2. In the Fe/Ni cells, the cumulative contributions from chlorination of Fe and Ni amount to a reversible theoretical capacity of 159 mAh g^{-1} (100% SOC), with 40% SOC available at 2.32 V (reaction 9), and 60% available at 2.57 V (reaction 10). As is common in state-of-the art literature on sodium-metal-chloride cells,[8,16] we consider the amount of granulated material added to the cathode (Ni, Fe, Al, NaCl and additives) when computing the gravimetric capacity, while the liquid secondary electrolyte NaAlCl$_4$, the Ni foam and Ni pistons are not included in the calculation – see supporting information note 1: Ni foam. Corresponding values on cell level depend on the specific cell design.[6] For the Fe/Ni cells, the theoretical capacity of 159 mAh g^{-1} translates into an areal capacity of 51 mAh cm^{-2} (based on the solid electrolyte surface) at a mass loading of 0.32 g cm^{-2}.

Inspection of figure 5-2 shows that the full theoretical capacity (corresponding to 100% SOC) can be obtained during the capacity-limited, galvanostatic maiden charge at voltages well below the upper cutoff voltage. For the Fe/Ni cells, we observe two pronounced voltage plateaus, featuring low overpotentials (+10 mV) compared to the equilibrium potentials, with the low-voltage plateau associated with Fe chlorination at low SOC, and the high-voltage plateau associated with Ni chlorination at high SOC. However, the high voltage edge (defined as the onset and ending of the high-voltage plateau during charge and discharge, respectively) occurs at a lower SOC (25% SOC) than theoretically possible (40% SOC), considering the iron content of the cathode. Chlorination of the remaining iron requires higher overpotentials, and takes place together with Ni chlorination in the high-voltage plateau.

In the subsequent cycles shown together with the maiden cycle in figure 5-2b, we restrict the SOC window to a lower limit of 10% SOC, and to an upper limit of 90% SOC, providing a cycled capacity of 127 mAh g^{-1}. Despite the low current density applied (3 mA cm^{-2}, 0.05C), we observe a pronounced hysteresis in the voltage profile of the Fe/Ni cells between charge and discharge, manifesting itself in a shift of the high-voltage edge to higher SOC during discharge. The hysteresis results in substantially lower cell voltages during discharge than during charge at intermediate SOC (between 25% and 50% SOC), thereby reducing the roundtrip energy efficiency (further discussion below). During the second and third discharge, the high-voltage edge gradually moves to lower SOC (from 55% to 40% SOC). We

ascribe this evolution of the discharge voltage profile to run-in processes within the cathode. Run-in processes can include a stabilization of the Fe/Ni cathode microstructure, where cycling enables a redistribution and improved contacting of the Fe and Ni particles forming the electronic backbone.[29,30] These effects are superimposed with the cell response to the SOC window reduction from the full SOC window in the first cycle down to 10% to 90% SOC in the following cycles. Changing the SOC window results in other locations of the cathode to participate in the electrochemical reactions[2] (see also discussion on reaction front mechanism below). Furthermore, we observe that the transition from the low-voltage Fe to the high-voltage Ni plateau takes place via different steps, indicating several intermediate processes. Based on literature, these steps can be related to a contribution of additives (e.g. $FeS + 2\,NaCl + Ni \leftrightarrow FeCl_2 + NiS + 2\,Na$ at 2.37 V and $Ni + 2\,NaF \leftrightarrow NiF_2 + 2\,Na$ at 2.39 V)[2,22] and to the formation of intermediate phases (e.g. Na_6FeCl_8).[10,26] Interestingly, we can distinguish two intermediate plateaus during charge, while during discharge there are three separate kinks in the transition region between low- and high-voltage plateau. During charge, these intermediate plateaus are shorter and the voltage trace makes a steeper transition between the low- and the high-voltage plateau, indicating substantial overpotentials. As a result, the intermediate reactions mainly take place in the high-voltage plateau during charge, together with the chlorination of Ni. During discharge, the individual plateaus are differentiated according to their reaction potentials. In the future, further investigation is required to fully resolve the details of these transition reactions. Figure 5-2c shows the voltage profiles of the Fe/Ni cell during a subsequent rate test, where we increase the charge and discharge rates symmetrically in four steps from 6 mA cm^{-2} (0.1C) to 20 mA cm^{-2} (0.4C). For each current density, we perform three cycles. The corresponding voltage profiles overlay almost ideally at each current density, indicating no further microstructural changes in the cathode. However, the increasing C-rates affect the characteristics of the hysteresis observed in the voltage profiles during charge and discharge. In particular, both in charge and discharge, the high-voltage edge shifts to lower SOC with increasing C-rates (by about 5 mAh g^{-1} between 0.1C and 0.4C). During charge, the shift of the high-voltage edge can be understood based on the increasing overpotentials associated with increasing charge currents. The higher the charge current, the higher the overpotentials, and the earlier (at lower SOC) the high-voltage plateau is reached, where Ni chlorination is enabled. Our cycling data in figure 5-2c shows that, in the subsequent discharge, more $NiCl_2$ is available for dechlorination, which enables a longer discharge on the high-voltage plateau, resulting in the observed shift of the high-voltage edge to lower SOC. This leads to the intriguing insight, that in Fe/Ni cells the ratio of Ni and Fe species undergoing oxidation/reduction depends on the current density applied during charge, and higher amounts of Ni are chlorinated at higher charge rates.

In figure 5-2d, we maintain a constant charge rate of 20 mA cm^{-2} (0.4C) to respect the upper cut-off voltage, but further increase the discharge rate in four steps from 20 mA cm^{-2} (0.4C), up to 80 mA cm^{-2} (1.6C). Again, three cycles per rate are performed, resulting in overlying

voltage profiles, indicating a stable cathode microstructure. In contrast to figure 5-2c, the high-voltage edge is no longer subject to a shift during discharge at the different rates, since the constant charge rates lead to the same degree of Ni chlorination, confirming the conclusion above. For the highest discharge rates of 1.6C, the cell voltage falls to values of around 2.1 V. Remarkably, we find that the voltage traces during charge shown in figure 5-2c and the voltage traces during discharge shown in figure 5-2d follow an almost ideal linear (ohmic) relation with the applied currents (see figure 5-9). Only in the transition region between low-voltage and high-voltage plateau (highlighted in figure 5-2c) deviations from linearity between the voltage traces reach values above 1% (see figure 5-9). Thus, non-linear polarization resistances are negligible, and we can derive the relevant effective cell resistances for charge and discharge in our cells based on a simple linear interpolation, as described in more detail in the supporting information note 2: Resistance Computation. We present the computed cell resistance during charge and discharge as a function of SOC in figure 5-2e-f, respectively. In both cases, we identify a base resistance of around 0.6 Ω (1.9 Ωcm^2), which is present independently of SOC. The base resistance comprises the resistances related to passive cell components, Na-β"-alumina solid electrolyte, and even anode processes, which did not show an SOC-dependency in a previous study.[31] Thus, we can ascribe the SOC-dependent, variable resistance contributions as observed both for charge and discharge in figure 5-2e-f to cathode processes.
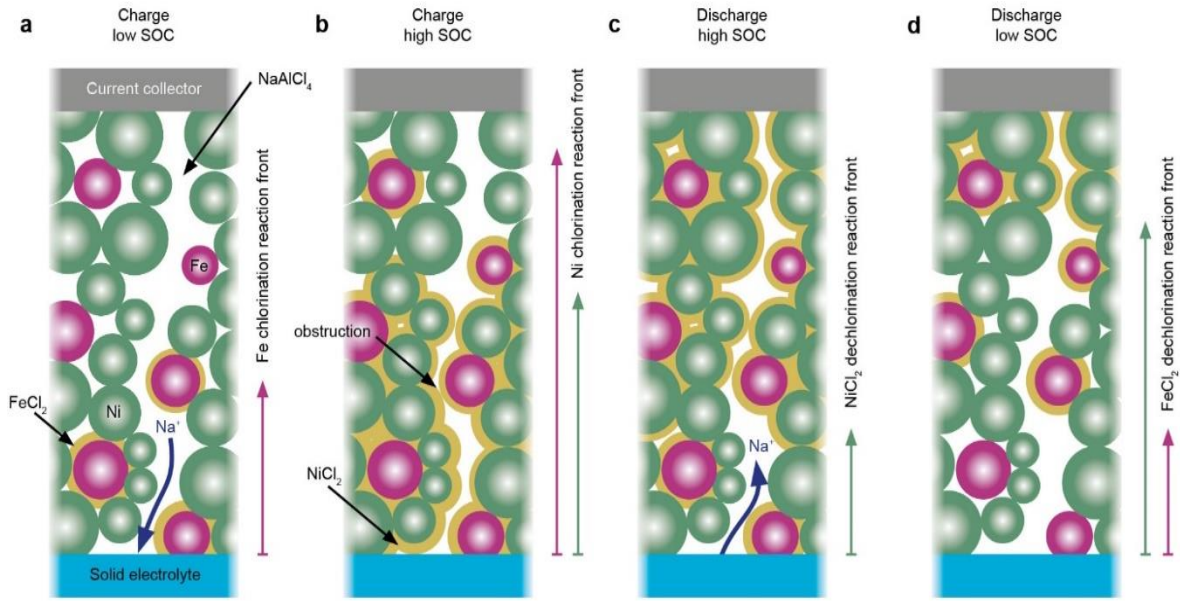
Figure 5-3: Schematics of the reaction front mechanism in the Fe/Ni cathode. a) Progressing Fe chlorination reaction front during charge at an early stage of the charge process at e.g. 15% SOC, also highlighting the transport path of Na ions through the liquid NaAlCl₄ secondary electrolyte. b) Progressing Fe and Ni chlorination reaction fronts during charge at a late stage of the charge process at e.g. 70% SOC highlighting the formation of obstructions to the ionic transport. c) Progressing NiCl₂ dechlorination reaction front during discharge at an early stage of the discharge process at e.g. 70% SOC. d) Progressing NiCl₂ and FeCl₂ dechlorination reaction fronts during discharge at a late stage of the discharge process at e.g. 15%. SOC. Dissolution (a,b) and precipitation (c,d) of NaCl crystals are not shown to improve readability.

In figure 5-3, we show schematics of the cathode chlorination and dechlorination processes during charge and discharge explaining these SOC-dependent resistance contributions from the Fe/Ni cathode. The cathode is composed of a porous percolating network of the Ni and Fe particles. The channels in the network are filled with the liquid NaAlCl₄ secondary electrolyte ensuring the transport of Na ions. For Fe/Ni cells, during charge at low SOC (figure 5-3a), Fe chlorination starts from the Na-β''-alumina solid electrolyte interface, and progresses across the cathode towards the current collector. The initiation of the reaction front directly at the Na-β''-alumina solid electrolyte interface and its movement into the depth of the cathode were experimentally shown with high spatial resolution using neutron diffraction technique.[26] The more the Fe chlorination reaction front advances, the longer the transport path for the Na ions through the liquid NaAlCl₄ secondary electrolyte from the reaction site to the Na-β''-alumina solid electrolyte, which results in increasing cell resistance (figure 5-2e, 10-15 % SOC). Exclusively the Na ions have to travel from the reaction site to the Na-β''-alumina solid electrolyte interface, while the Fe-ions, the Ni-ions and the

Cl ions required for the reactions are evenly distributed over the entire depth of the cathode. Towards the end of Fe chlorination, the overpotentials rise substantially, which we ascribe to limited accessibility of the remaining Fe in the cathode microstructure, resulting in a rapid rise in cell resistance, as seen in figure 5-2e at 20-25% SOC. The high cell resistance for Fe chlorination in this transition region, together with a contribution of additives, is seen as a main cause for the hysteresis observed in the charge/discharge behavior in Fe/Ni cells. At a later stage, the transport resistances required to continue Fe chlorination result in an increase of the cell potential to above the equilibrium potential of Ni chlorination, which is then initiated, thereby reducing the cell resistance, as seen in figure 5-2e at 30% SOC. During charge at high SOC (figure 5-3b), Ni chlorination starts from the Na-β''-alumina solid electrolyte interface, and progresses across the cathode towards the current collector. The more the Ni chlorination reaction front advances into the cathode, the longer the transport paths for the Na ions through the liquid $NaAlCl_4$ secondary electrolyte, which results in a continuous increase in cell resistance, as seen in figure 5-2e from 30% to 90% SOC. However, the resistance increases non-linearly. This can be associated with the volumetric expansion of the Fe and Ni due to the metal chlorination. In fact, chlorinating Fe and Ni to $FeCl_2$ and $NiCl_2$ results in a volume increase by more than a factor of two and the formation of lamellar structures in the cathode that occupy a considerable amount of space as was shown via SEM on charged cells.[32] This can result in obstructions that further increase the required transport path for the Na ions (figure 5-3b). A tailored cathode porosity that can accommodate this volumetric expansion and prevent obstructions to cause even further increases in cell resistance is critically important. To illustrate this fact, we performed dedicated experiments, where we compare granulated cathode material to a non-granulated cathode pellet (see supporting information note 3: Granulation, and figure 5-10). These experiments showed that only a granulated cathode can ensure effective ionic transport, thereby reducing overpotentials to an acceptable level.

During discharge, dechlorination starts with $NiCl_2$, but again proceeds from the Na-β''-alumina solid electrolyte interface, across the cathode, towards the current collector (figure 5-3c). While during charge, obstructions in the cathode related to the chlorination were hindering Na ion transport leading to a rise of the cell resistance beyond a linear increase, no such effect is observed during discharge. In fact, the dechlorination progresses away from the solid electrolyte and thereby simultaneously removes the obstructions. Therefore, as the $NiCl_2$ dechlorination front proceeds, the cell resistance rises linearly (figure 5-2f) until the cell voltage drops below the equilibrium potential of $FeCl_2$ dechlorination, which is then initiated (figure 5-3d). The initiation of $FeCl_2$ dechlorination reduces the effective cell resistance in figure 5-2f at 20% SOC. Within the transition region between the $NiCl_2$ dechlorination and $FeCl_2$ dechlorination, there is a small intermediate peak in the resistance profile at around 25% SOC, which we attribute to the fluorine added as an additive in the cathode granules as discussed above, where $Ni + 2\,NaF \leftrightarrow NiF_2 + 2\,Na$ at a cell voltage of 2.39 V.[22] In summary, this reaction front mechanism (figure 5-3) explains the non-

monotonic resistance behavior in figure 5-2e-f. These mechanistic insights enable us to understand why a mixed cathode with Fe and Ni can reduce the cell resistance in specific SOC domains, and how cathodes can be tailored to different demands in specific power and energy. Our analysis also demonstrates a strong increase in cathode resistance in the transition region, which originates from the two spatially separated reaction fronts (associated with Fe and Ni oxidation and reduction) propagating across the depth of the cathode compartment. This results in a hysteresis in the voltage traces of charge and discharge, reducing the energy efficiency in this SOC range. This has to be taken into account when deciding for or against the use of Fe in the cathode. Given the mixed consequences of using Fe in the cathode, it is natural to compare the obtained results to pure Ni cathodes.

We present the results for the Ni cells in figure 5-4. In the absence of Fe, only reaction 8 and reaction 10 occur, and no Fe overcharge reaction can take place. This allows setting the upper cut-off voltage to 3.05 V, above which decomposition of $NaAlCl_4$ would result.[3] Based on the cathode composition of the Ni cells (see Experimental section), we expect an irreversible capacity contribution based on reaction 8 of approximately 15 mAh g^{-1}, until the entire Al content is consumed. The remaining NaCl in the cathode could ideally provide a total reversible capacity of 169 mAh g^{-1} based on reaction 10. This theoretical capacity of 169 mAh g^{-1} for the studied Ni cells slightly exceeds the theoretical capacity of the Fe/Ni cells and translates into an areal capacity of 54 mAh cm^{-2} at a mass loading of 0.32 g cm^{-2}. For an easier comparison between the two cathode compositions, we define state of charge (SOC) based on the theoretical capacity of the Fe/Ni cells.

In figure 5-4a, we show the maiden charge of a Ni cell. In contrast to the Fe/Ni cells, we observe only a single voltage plateau associated with reaction 10. In figure 5-4b, we show the first three cycles of the Ni cell, compared to the data from the Fe/Ni cells. Also for the Ni cells, we limit the cycling window between 10% and 90% SOC. The Ni cell immediately shows a stable voltage response with overlying voltage traces. This supports that the change in discharge potentials in the Fe/Ni cells during the first three cycles stems from a redistribution of Fe in the cathode microstructure. A contribution of additives is not observed in the Ni cell, since the cell voltage remains above 2.39 V. Towards the end of discharge, the cell voltage begins to decrease, indicating increasing internal cell resistances. Interestingly, both charge and discharge voltage in the Ni plateau are higher for the Ni cell than for the Fe/Ni cell. Based on dedicated GITT measurements, we find a slightly higher OCV in the high-voltage plateau for the pure Ni-cell of 2.58 V, compared to the 2.57 V measured for the Fe/Ni cell (see figure 5-9). The presence of Fe has previously been reported to decrease the cell potential in the Ni plateau,[23] where it was ascribed to the presence of a $Ni_{1-x}Fe_xCl_2$.[26] Alternatively, it is also possible to consider a mixed electrode potential vs. Na^+/Na (see reaction 9).[33]
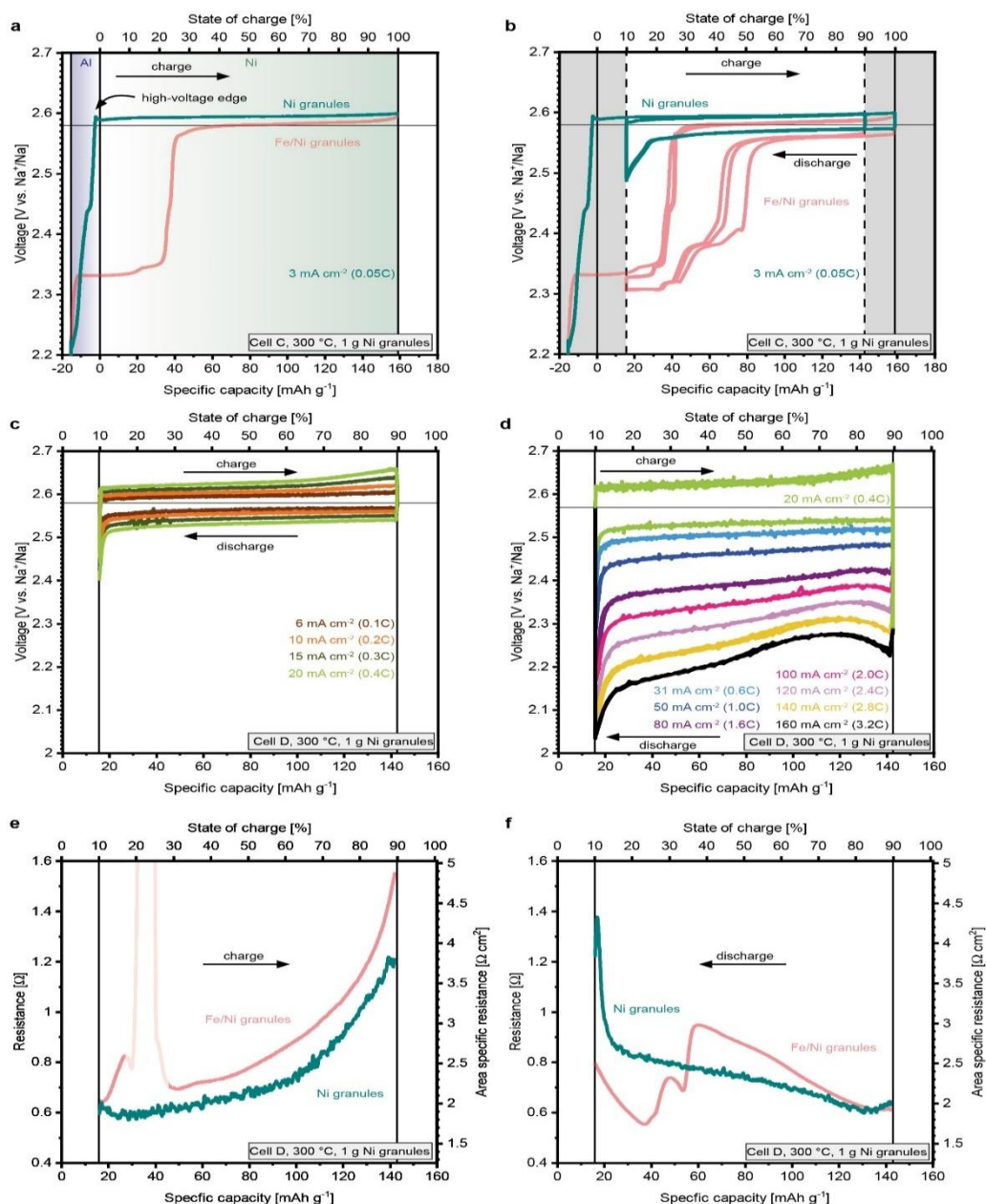
Figure 5-4: Galvanostatic cycling of planar sodium-metal chloride cells with Ni cathode. a) Voltage vs. capacity during maiden charge, highlighting the two metal chlorination reactions (Al and Ni). b) Voltage vs. capacity during the first three cycles. c) Symmetric rate test: Voltage vs. specific capacity; charge and discharge rates increase symmetrically from 6 mA cm^{-2} to 20 mA cm^{-2}, three cycles per rate. d) Discharge rate test: Voltage vs. specific capacity; charge rates are constant at 20 mA cm^{-2}, while discharge rates increase from 20 mA cm^{-2} to 160 mA cm^{-2}, three cycles per rate. e) Cell resistance during charge computed from voltage traces in c). f) Cell resistance during discharge computed from voltage traces in d (considering 20 to 80 mA cm^{-2}). In a), b), e) and f), the corresponding data from the Fe/Ni cell is shown for reference.

In figure 5-4c-d, we show a rate test for the Ni cathode, which is mostly analogous to the Fe/Ni cells (figure 5-2). For the Ni cells, we observe no plateau shifts, since only reaction 10 is performed. Furthermore, as shown in figure 5-4d, the pure Ni cathodes enable even higher discharge rates than the Ni/Fe cells, allowing us to include four additional discharge rate steps ranging from 100 mA cm^{-2} (2C) up to 160 mA cm^{-2} (3.2C). Since only the high-voltage reaction 10 is performed, the potential stays comparably high also at low SOC, and for double the discharge rate we can still limit the potential drop to similar amounts as for the Fe/Ni cells (figure 5-2). Just like the Fe/Ni cells, also the Ni cells exhibit a linear (ohmic) relation with the applied currents during charge and discharge. For the Ni cells, the deviation from linearity remains below 0.2% during charge and only exceeds 0.5% at the very end of discharge (see figure 5-11). Therefore, also for the Ni cells, we can easily compute the cell resistances vs. SOC for charge and discharge (figure 5-4e-f). To facilitate comparison to the Fe/Ni cells, we compute the resistance based on the discharge traces between 20 and 80 mA cm^{-2}. In contrast to the Fe/Ni cells, the Ni cells show a monotonic increase in resistance as SOC increases during charge and as SOC decreases during discharge, since only a single electrochemical reaction is performed. Only in the very beginning of the charge and discharge, we see a minor dip in the resistance of the Ni cells that might be related to start-up processes due to the abrupt increase in current. This effect is especially relevant at high currents (figure 5-4c-d). Both at the end of charge and discharge, we find a steep increase in resistance related to limited accessibility of reaction sites, illustrating the benefit of the established capacity limitations. Cycling beyond these limits would be inefficient due to considerably increasing resistances.

Figure 5-5: Rate test summary. a)Fe/Ni cathode: Specific energy charged (open triangles) and discharged (open circles), as well as energy efficiency (solid squares) vs. cycle number for charge and discharge rates ranging from 6 mA cm⁻² (0.1C) to 80 mA cm⁻² (1.6C). Changes in specific energy charged between cycle 13 and 24 are related to a fluctuation in the cell temperature by about 5 °C. b) Ni cathode: Specific energy charged (open triangles) and discharged (open circles), as well as energy efficiency (solid squares) vs. cycle number for charge and discharge rates ranging from 6 mA cm⁻² (0.1C) to 160 mA cm⁻² (3.2C). c) Fe/Ni cathode: Specific charge (open triangles) and discharge power (open circles) vs. cycle number. d) Ni cathode: Specific charge (open triangles) and discharge power (open circles) vs. cycle number. The color code is the same as introduced in figure 5-2 and 5-4.

Figure 5-5: Rate test summary. a)Fe/Ni cathode: Specific energy charged (open triangles) and discharged (open circles), as well as energy efficiency (solid squares) vs. cycle number for charge and discharge rates ranging from 6 mA cm^{-2} (0.1C) to 80 mA cm^{-2} (1.6C). Changes in specific energy charged between cycle 13 and 24 are related to a fluctuation in the cell temperature by about 5 °C. b) Ni cathode: Specific energy charged (open triangles) and discharged (open circles), as well as energy efficiency (solid squares) vs. cycle number for charge and discharge rates ranging from 6 mA cm^{-2} (0.1C) to 160 mA cm^{-2} (3.2C). c) Fe/Ni cathode: Specific charge (open triangles) and discharge power (open circles) vs. cycle number. d) Ni cathode: Specific charge (open triangles) and discharge power (open circles) vs. cycle number. The color code is the same as introduced in figure 5-2 and 5-4.

We summarize the rate capability of both types of planar sodium-metal chloride cells in figure 5-5. For each cycle of the rate test, we show the specific energy for charge and discharge, and the calculated roundtrip energy efficiency, as obtained by galvanostatic, capacity-limited cycling between 10% SOC and 90% SOC (figure 5-5a-b). For the Fe/Ni cells, due to increased overpotentials at higher current densities, the discharge energy decreases from 315 Wh kg^{-1} to 292 Wh kg^{-1} when increasing the discharge rates from 0.1C to 1.6C, with energy efficiencies of 97% and 89%, respectively. For the Ni cells, the discharge energies range between 325 Wh kg^{-1} and 281 Wh kg^{-1} when increasing the discharge rates from 0.1C to 3.2C, with energy efficiencies between 99% and 84%, respectively. Figure 5-5c-d show the corresponding specific power during charge and discharge, averaged over the entire capacity window between 10% SOC and 90% SOC, as a function of the cycle number. We first discuss the Fe/Ni cells: While for a discharge current of 6 mA cm^{-2} (0.1C) the average discharge power results in 47 W kg^{-1}, during the fast discharge at 80 mA cm^{-2} (1.6C), we obtain an average discharge power of 580 W kg^{-1}. Within the high-voltage plateau, the maximum discharge power even reaches 608 W kg^{-1}, while at the end of the low-voltage plateau the discharge power is around 530 W kg^{-1} (see figure 5-12). When discharging the Ni cells at 80 mA cm^{-2} (1.6C), we obtain a slightly higher average discharge power of 598 W kg^{-1}, due to the higher average cell potential of the Ni cell. The measured power of the Ni cells further increases to 1105 W kg^{-1} when discharging at 160 mA cm^{-2} (3.2C). Since during discharge of the pure Ni cells only the high-voltage Ni dechlorination is performed (and no low-voltage Fe dechlorination), the cell potential stays high over the entire SOC window. This enables even higher discharge rates by avoiding conflicts with the lower cut-off voltage.
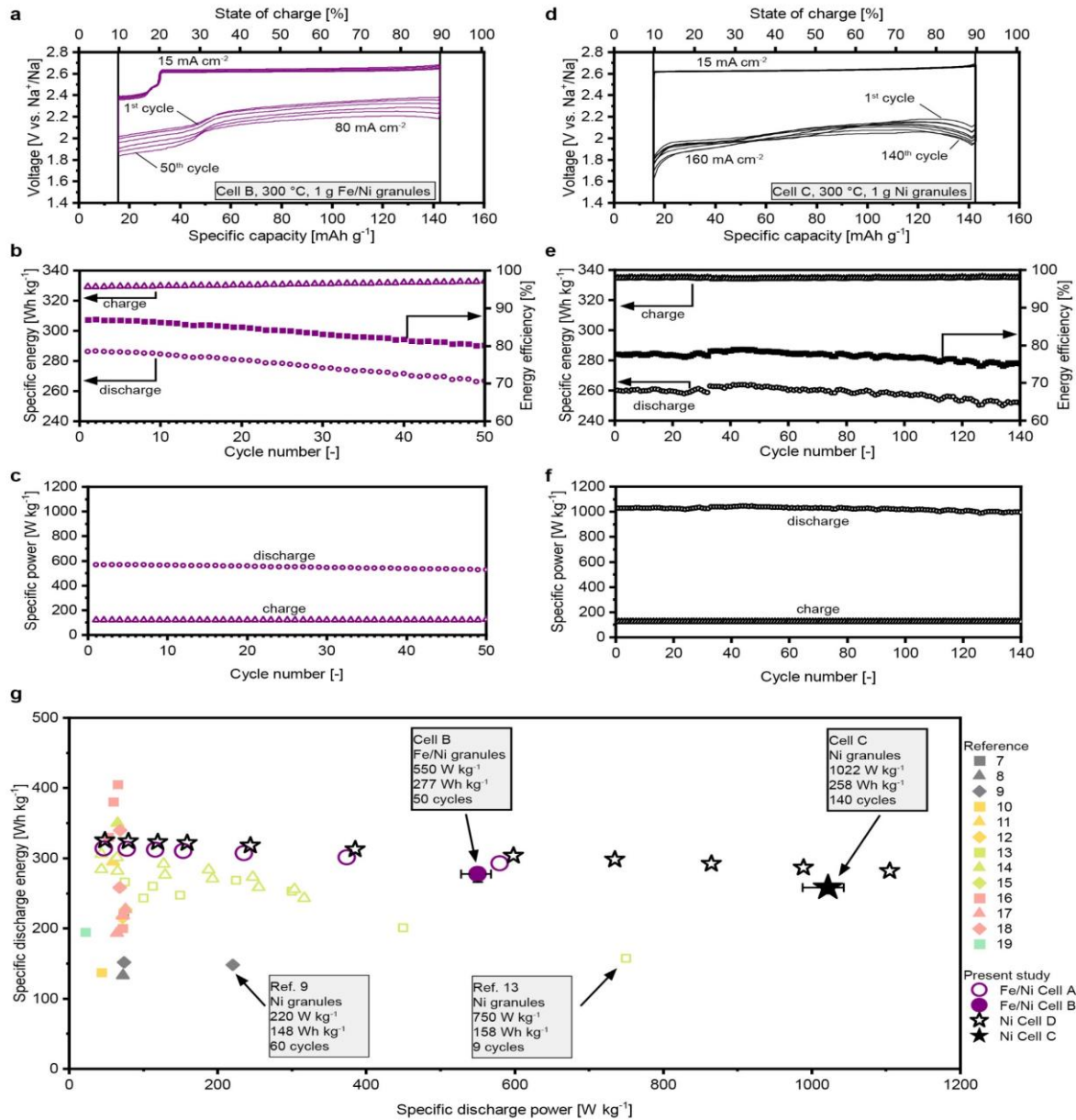
Figure 5-6: High-power discharging. a-c) Fe/Ni cathode: a) Cell voltage vs. specific capacity (charging at 15 mA cm^{-2}, 0.3C, and discharging at 80 mA cm^{-2}, 1.6C, over 50 cycles, showing every 10th cycle). b) Specific energy charged and discharged, as well as energy efficiency. c) Averaged specific charge and discharge power. d-f), Ni cathode: d) Cell voltage vs. specific capacity (charging at 15 mA cm^{-2}, 0.3C, and discharging at 160 mA cm^{-2}, 3.2C, over 140 cycles, showing every 20th cycle). e) Specific energy charged and discharged, as well as energy efficiency. f) Averaged specific charge and discharge power. g) Ragone plot showing specific discharge energy vs. specific discharge power of the present study as compared to literature. Performance shown for equal or less than 10 cycles is represented by open symbols, while more than 10 cycles are represented with solid symbols. The theoretical areal capacity is approximately 50 mAh cm^{-2} in all studies except for ref. 8, 13 that study higher areal capacities (table 5-1).

In figure 5-6a-f, we show high-power discharging of our sodium-metal chloride cells, while applying a charge rate of 15 mA cm^{-2} (0.3C). Over a total of 50 cycles, the Fe/Ni cell supplies an average specific discharge energy of 277 Wh kg^{-1} at an average discharge power 550 W kg^{-1}, when discharged at 80 mA cm^{-2} (1.6C). The fading observed in figure 5-6b over the 50 cycles illustrates that these conditions stress the Fe/Ni cell and lead to degradation. In contrast, the Ni cell supplies an average specific discharge energy of 258 Wh kg^{-1} at an average discharge power 1022 W kg^{-1}, when discharged at 160 mA cm^{-2} (3.2C), with only minor signs of degradation over a total of 140 cycles.

In figure 5-6g, we compare the performance achieved in the present study to reports on planar Na-NiCl$_2$ and Fe-NiCl$_2$ cells by showing specific discharge energy vs. specific discharge power with respect to the cathode granule weight in a Ragone plot. We show data from the rate test in figure 5-5, as well as the average of the 50 cycles for the Fe/Ni cathode (error bars represent the maximum and the minimum value obtained over the 50 cycles), and the average of the 140 cycles for the Ni cathode. In literature, we find data from both high-temperature experiments (around 300 °C), and from intermediate temperature experiments (around 190 °C). We can further distinguish two main groups, based on the number of cycles demonstrated. We define a first group with long-term studies, showing more than ten cycles (typically between 50 and 300 cycles, represented in figure 5-6g by solid symbols). The majority of these studies achieved a specific discharge power below 100 W kg^{-1}. To date, the highest specific power in the long-term cycling group is 220 W kg^{-1}, achieved over 60 cycles at a temperature of 280 °C and at a specific energy of 148 Wh kg^{-1}.[9] Comparing this to our present Fe/Ni cell result, we find that we were able to increase the specific power by more than a factor two, while simultaneously increasing the specific energy by 87%. More importantly, our Ni cell could increase the specific power by more than a factor four compared to ref. 9, while increasing the specific energy by 74%. In the second group, we present studies showing short-term cycling of equal or less than ten cycles (represented in figure 5-6g by open symbols). Here, the specific power ranges between 100 W kg^{-1} and 750 W kg^{-1}.[13] Interestingly, there is a roughly linear trend in the Ragone plot for the short-term cycling group from literature, where the specific energy drastically decreases with increasing specific power. By plotting our rate test results with three cycles per data point from figure 5-5 into the Ragone plot, we can show that in our cells with the capacity-limited cycling protocol, the specific energy is more stable against increasing the power. Comparing our results both against long-term and short-term cycling results from the literature illustrates the strengths of the proposed cells.

While for cells with a mixed Fe/Ni cathode, charge rates are limited to comparably low current densities due to the risk of starting a Fe overcharge reaction at approximately 2.75 V, cells without Fe in the cathode can be charged substantially faster. We demonstrate this in figure 5-7. In figure 5-7a, we show a rate test with charge rates increasing from 20 mA cm^{-2} up to 110 mA cm^{-2}, which corresponds to a C-rate above 2C. As shown in figure 5-7b, we can achieve these high charge rates combined with discharge rates of 160 mA cm^{-2} at

energy efficiencies of around 80%. For this high-power cycling, both charge and discharge power range around 1000 W kg^{-1} (figure 5-7c). By comparing this performance to the existing results on planar Na-NiCl$_2$ and Fe-NiCl$_2$ cells, we find that this represents a remarkable increase. To date, the highest reported charge rates for planar sodium-metal chloride cells are 30 mA cm^{-2} (corresponding to a specific charge power of 239 W kg^{-1}) at a specific capacity of 90 mAh g^{-1}.[9] We can conclude that the Ni cells in the present study with a charge rate of 110 mA cm^{-2} (corresponding to a specific charge power of 976 W kg^{-1}) at a specific capacity of 127 mAh g^{-1} provide a substantial increase in specific charge power by more than a factor four while simultaneously increasing the specific capacity by more than 40%.
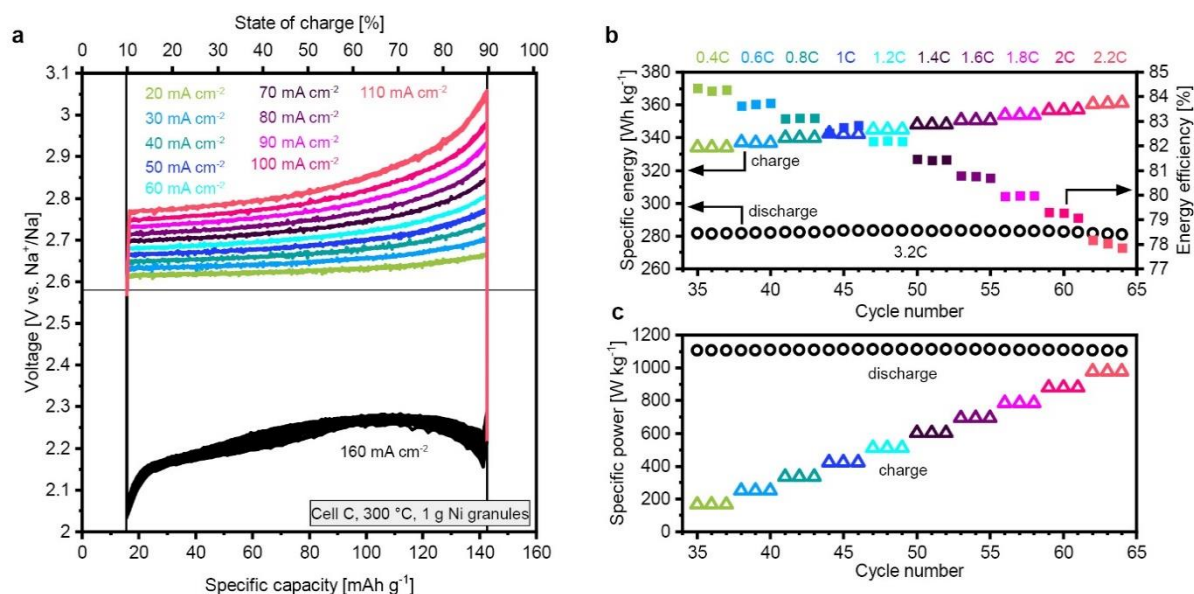
Figure 5-7: High-power charge rate test of the Ni cathode. a) Voltage vs. specific capacity, where discharge rates are constant at 160 mA cm^{-2}, while charge rates increase from 20 mA cm^{-2} in steps of 10 mA cm^{-2} up to 110 mA cm^{-2}, with three cycles per rate. b) Corresponding specific energy charged and discharged, as well as energy efficiency vs. cycle number, also highlighting the C-rates. c) Corresponding averaged, specific charge and discharge power vs. cycle number.

5.3 Conclusion

We compared planar sodium-metal chloride cells with Fe/Ni cathodes to cells with pure Ni cathodes. Based on rate tests, we found an ohmic cell behavior over the majority of the cycling window irrespective of composition. By analyzing the effective cell resistance, we showed that combining Fe and Ni in the cathode allows to initiate two individual reaction fronts progressing across the cathode. As a result, the effective cell resistance shows a non-monotonic behavior versus state of charge (SOC). Such cells with Fe/Ni cathodes showed high specific discharge energy and power of 277 Wh kg^{-1} and 550 W kg^{-1}, respectively, over

a total of 50 cycles. Within the group of long-term cycling results in literature with more than ten cycles shown, the presented cell performance substantially exceeds previous reports on planar sodium-metal chloride cells, increasing specific power by more than a factor two, while simultaneously increasing the specific energy by 87% as compared to the best performing cells to date. Remarkably, cells with pure Ni cathodes showed even higher specific discharge power of 1022 W kg^{-1}, while maintaining a high specific discharge energy of 258 Wh kg^{-1} over a total of 140 cycles, thereby increasing the specific power by more than a factor of four over the state-of-the-art, while simultaneously increasing the specific energy by 74%. Furthermore, Ni cathodes demonstrated also substantially enhanced charging performance with a specific power of 976 W kg^{-1} and a specific capacity of 127 mAh g^{-1}. With our study we show that rationally designing the cathode based on mechanistic understanding of the involved electrochemical and transport processes provides a pathway to markedly increase the performance of the sodium-metal chloride technology. For future work it is necessary to study more dynamic cycling protocols and higher mass loadings to further probe the effect of cathode composition. Furthermore, it is desirable to develop solutions to transfer from lab cells (as used in the present study) towards commercial cell designs that are economically viable. This could enable a large-scale deployment of this powerful technology.

5.4 Methods

In figure 5-1a, we show a schematic cross-sectional view of our high-temperature planar sodium-metal chloride lab cell. Considerations on how to adapt such a cell design to maximize energy density on cell level for commercialization were discussed in ref. 6. We assembled the cells from two α-alumina collars (99.7% Al$_2$O$_3$, inner diameter 20 mm) and one Na-β"-alumina solid electrolyte disc. Na-β"-alumina discs were prepared by pressing spray-dried Li-stabilized Na-β"-alumina powder into disc-shaped green bodies with a diameter of 45 mm and a thickness of approximately 4 mm. The green bodies were placed onto buffer green discs and sintered inside a ceramic encapsulation in static air at 1600 °C (Nabertherm HT 40/17, heating rate 3 K min^{-1}, dwell time 5 min).[34] Subsequently, the sintered Na-β"-alumina discs were ground down to a thickness of 1 mm (Elb surface grinding machine with diamond blade and sample water cooling), cleaned in isopropyl alcohol, and dried in an oven under air at 100 °C. Inside a tube furnace at 300 °C, we measured a conductivity of 0.2 S cm^{-1} for the Na-β"-alumina using electrochemical impedance spectroscopy (Zahner IM6, frequency 1 Hz to 1 MHz, amplitude 20 mV) in four-point-probe configuration (figure 5-13).[34] Subsequently, the solid electrolyte discs were glass sealed between the two α-alumina collars using a high-temperature glass sealing at 1010 °C (Carbolite CWF 1200, heating rate 3 K min^{-1}, dwell time 5 min), similar to the process in state-of-the-art commercial tubular cells[1] to obtain the ceramic subassembly of the cell (figure 5-1b-c). A K-type

thermocouple was inserted into a slit machined into one of the α-alumina collars to accurately measure the cell temperature. To avoid dewetting of Na from the sodiophobic Na-β"-alumina surface, the anode side of the Na-β"-alumina was spray coated with a porous carbon coating (composed of 7 wt.% carbon black, 11 wt.% sodium hexamethaphosphate, 55 wt.% isopropanol, 27 wt.% water, and 0.3 wt.% acetone) using an airbrush system (Aztek, pressurized air, ~2 bar) and dried at 280 °C in air (Carbolite CWF 1200, heating rate 5 K min^{-1}, dwell time 5 min) to remove all remaining solvents (porosity and thickness of coating after drying ~80% and 50 µm (inset in figure 5-1c), respectively). Further details on the carbon coating can be found in ref. 31. Cell assembly and charge/discharge cycling was performed in an Ar-filled glove box (typically $c_{H2O} < 0.1$ ppm, $c_{O2} < 0.1$ ppm). We filled the cathode compartment with 1 g of millimeter-sized cathode granules. We characterized the materials based on Brunauer–Emmett–Teller (BET) measurements in a BET surface area analyzer. Two different cathode compositions were investigated: Fe/Ni granules (used in Cell A and Cell B, where during cycling Fe and Ni are electrochemically active) consist of the three metallic components Ni (50 wt.%, filamentary Ni255, BET surface area: 0.64 m^2 g^{-1}), Fe (7 wt.%, BET surface area: 0.15 m^2 g^{-1}), and Al (0.5 wt.%, BET surface area: 0.16 m^2 g^{-1}). Furthermore, they contain micro-fine NaCl (39 wt.%) and the following additives: FeS (2 wt.%), NaF (2 wt.%), and NaI (0.5 wt.%). The addition of a small amount of Al to the cathode has been discussed as beneficial since it can provide additional porosity.[2,22] The sulfur provided in the form of FeS has shown to prevent Ni particle growth during cycling[2] and can facilitate the initial activation of Fe and Ni.[10] Ni granules (used in Cell C and Cell D, where during cycling only Ni is electrochemically active) consist of the two metallic components Ni (54 wt.%, filamentary Ni255), and Al (0.5 wt.%). Furthermore, they contain NaCl (42 wt.%) and the following additives: FeS (2 wt.%), NaF (2 wt.%), and NaI (0.5 wt.%). The granules were manufactured by mixing and compacting the raw materials using a laboratory roller press (Komarek B050A, roll force 30 kN), granulated using a laboratory granulator (Komarek G100SA) and sieved to remove particles larger than 1.6 mm. Images from both granule types obtained via scanning electron microscopy (SEM) and energy-dispersive X-ray spectroscopy (EDS) are presented in figure 5-14 and figure 5-15. X-ray powder diffraction (XRD) analysis of the cathode materials is shown in figure 5-16. After filling the cathode compartment with the granules, we added 0.5 g of secondary electrolyte NaAlCl$_4$ (anhydrous, powder, 99.99%) and vacuum infiltrated the molten NaAlCl$_4$ into the granules at a pressure of less than 10 mbar and a temperature of 200 °C (dwell time ~20 min) (figure 5-1d). We added a Ni foam (99.5% purity, 1.6 mm thickness, 95% porosity) and additional 0.2 g of NaAlCl$_4$ to the cathode side. The rigid Ni foam serves as both a current collector and NaAlCl$_4$ reservoir, compensating volume changes of the cathode material during charge/discharge cycling (figure 5-1e) – See supporting information note 1: Ni foam. Into the anode compartment, we added a disc of ~0.3 g of Na (99.9% purity, thickness ~1 mm). In principle, no initial Na is required on the anode side, as Na is generated electrochemically

during the charging of the cell, and the porous carbon coating functions as electrode. However, excess Na facilitates formation cycling and the study of the cathode compartment on lab scale. Liquid sodium plating and stripping dynamics was investigated in detail in a previous study demonstrating ultra-high current densities beyond 1000 mA cm^{-2} without dendrite formation.[31] The anode and cathode compartments were closed with spring-loaded Ni pistons. The entire assembly was compressed between stainless steel top and bottom plates using six stainless steel bolts and alumina washers for electrical insulation (figure 5-1f). Ni-wires fixed by screws connected the backside of the Ni pistons with the stainless steel top and bottom plates to bypass the electrical resistance of the springs. We used graphite seals placed between the α-alumina collars and the top and bottom plates to seal the cell towards the outside. The resulting active cell area was 3.14 cm^2, resulting in a cathode granule mass loading of 0.32 g cm^{-2}. Cells were charge/discharge cycled at 300 °C (Biologic VSP3e). The cell temperature during cycling was monitored and controlled with a precision of better than ± 10 °C using a resistive coil heater (SAF KM-HC-GS).

5.5 Supporting information

Supporting information note 1: Ni foam

In the cathode compartment, we employ a Ni foam. It serves as a current collector and provides a reservoir volume for the NaAlCl$_4$. This is important, since during cycling the cathode experiences volumetric changes due to the chemical reactions, mass transport and thermal fluctuations.[6] The flexibility of the Ni foam ensures a good electrical contact to the granules during cycling and can accommodate access amounts of NaAlCl$_4$ within its porosity. In this study, we load the cathode compartment of our laboratory test cells with 1 g cathode granules and infiltrate the granules with 0.5 g NaAlCl$_4$. Subsequently, we add the Ni foam and another 0.2 g NaAlCl$_4$ in powder form. For the cathode granules, we determined a tap density of approximately 2 g cm^{-3}, providing a porosity between the granules of about 50%. Using BET, for the Fe/Ni granules we measured a surface area of 1.1 m^2 g^{-1}, while for the pure Ni granules we measured 0.94 m^2 g^{-1}. On average, the granules provide about 1 m^2 g^{-1} surface area. The density of NaAlCl$_4$ at 300 °C is 1.6 g cm^{-3}. Considering that there is 1 g of cathode granules in the cathode compartment and given the cylindrical shape of the cathode compartment with a base area of 3.14 cm^2, the granules form a layer of about 1.6 mm in height in the compartment. The free space between the granules (0.25 cm^3) can accommodate roughly 0.4 g of NaAlCl$_4$, while the remaining NaAlCl$_4$ is stored in the Ni foam. The Ni foam is cut in a disc shape of 19 mm diameter and has a thickness of about 1.6 mm thickness. The foam has a porosity of 95%. The total mass of the foam added to the cathode compartment is 0.3 g. Based on BET measurements, we determined a surface area of 0.156 m^2 g^{-1} for the Ni foam. Given the porosity of the foam, the remaining 0.3 g of NaAlCl$_4$ within the cathode compartment that are not in the free space between the

granules fill the foam by about 40%. Therefore, the potentially active area of the Ni foam, where it is in contact with the $NaAlCl_4$, is 0.02 m^2. In contrast, the cathode granules provide about 1 m^2 of active area. It is therefore justified to neglect the contribution of the Ni foam as active material, since its surface area is only a few percent of the surface area provided by the granules.

Supporting information note 2: Resistance estimation

In figure 5-2, we analyze the cell behavior during charge and discharge. We want to better understand the underlying phenomena enabling the combination of high specific energy and high power observed for our cathode. To this end, we extract the effective cell resistance for charge curves in figure 5-2c and the discharge curves in figure 5-2d. This is possible, as the measured charge curves follow a linear trend in cell voltage vs. current density over most parts of the SOC window. In discharge, the linear trend between the cell voltage traces vs. current density holds almost ideally over the entire SOC window (see figure 5-9).

To determine the cell resistance during charge, we first compute the averaged charge voltage traces for the four different charge current densities of 6, 10, 15 and 20 mA cm^{-2}. The averaged curve for a given current density is obtained by evaluating the arithmetic mean from the three measured charge curves per current density as shown in figure 5-9a. Based on the four averaged charge curves, we perform linear interpolations for the voltage vs. current density as a function of the specific capacity – as shown exemplarily in figure 5-9a. In figure 5-9b, we plot the deviation from the linear interpolation for the four charge curves as a function of specific capacity. The deviation from linearity is for all four current densities well below 0.1% within the voltage plateaus associated with Fe- and Ni-chlorination, while it increases to a maximum of around 1.7% within the transition region between the two plateaus. In summary, we find that the charge behavior is almost ideally linear within the plateau regions, while there are deviations from linearity within the plateau transition region.

To determine the cell resistance during discharge, we perform the same steps as for the charge resistance. First, we compute the averaged charge voltage traces for the four different charge current densities of 20, 31, 50 and 80 mA cm^{-2}. The averaged curve for a given current density is obtained by evaluating the arithmetic mean from the three measured discharge curves per current density as shown in figure 5-9c. Based on the four averaged discharge curves, we perform linear interpolations for the voltage vs. current density as a function of the specific capacity – as shown exemplarily in figure 5-9c. In figure 5-9d, we plot the deviation from the linear interpolation for the four discharge curves as a function of specific capacity. The deviation from linearity is for all four current densities well below 0.1% within the voltage plateaus associated with $FeCl_2$- and $NiCl_2$-dechlorination. In contrast to the charge voltage traces, the deviation from linearity does not exceed 0.5% over

the entire SOC window. In summary, we find that the discharge behavior is almost ideally linear within the entire SOC window. In contrast to the discharge voltages traces obtained from the discharge rate test in figure 5-2d, the discharge voltage traces in figure 5-2c only provide an ohmic response within the high-voltage and the low-voltage plateau, while the transition region shows non-linear behavior due to the shift of the high-voltage edge. Therefore, the discharge data from figure 5-2c is less suitable for a resistance assessment. The remarkable linear response during charge in figure 5-2c and discharge shown in figure 5-2d enables us to directly obtain the effective cell resistance from the charge and discharge curves. We will discuss the resistance computation on the example of the discharge process, while it is directly applicable also to compute the charge resistance. We first consider the general relation for the discharge cell voltage U_{cell} given as:[35]

$$U_{cell} = OCV - i_D\, R_{ohmic} - \eta_c - \eta_a \qquad\qquad \text{Equation 39}$$

where OCV is the open circuit voltage, i_D is the discharge current, R_{ohmic} summarizes all ohmic (linear) contributions to the resistance, while η_c and η_a account for all non-linear polarization contributions from the cathode and the anode including species transport and charge transfer. Due to the almost ideal linear behavior of the cell voltage as a response to a change of the current density, η_c and η_a are practically negligible for our analysis and equation 39 simplifies to:

$$U_{cell} = OCV - i_D\, R_{ohmic} \qquad\qquad \text{Equation 40}$$

On this basis, we can compute the effective cell resistance during discharge vs. specific capacity and SOC as shown in figure 5-2f. For every moment during discharge (here shown as specific capacity and SOC) the resistance is obtained as the negative slope of the interpolated line between the voltage traces of the four different current densities. The computed resistance shows an intriguing behavior: At the initiation of discharge at 90% SOC, it starts at a value of ~0.6 Ω, which translates into ~2 Ωcm^2 for the area specific resistance (ASR) based on the active solid electrolyte area. As the discharge progresses and the NiCl$_2$ dechlorination reaction takes place, we observe a practically linear increase in the cell resistance up to a specific capacity of around 60 mAh g^{-1}, corresponding to ~40% SOC. This is where the NiCl$_2$ dechlorination voltage plateau ends (compare figure 5-2d). Subsequently, the effective cell resistance sharply reduces down to 0.55 Ω. Within the transition between the NiCl$_2$ dechlorination and FeCl$_2$ dechlorination, there is a small intermediate peak in the resistance profile at around 50 mAh g^{-1} that we attribute to the fluorine added as an additive in the cathode granules, where Ni + 2 NaF $\leftrightarrow$ NiF$_2$ + 2 Na at a cell voltage of 2.39 V.[22] After the transition to the FeCl$_2$ dechlorination reaction, the cell resistance starts to rise again roughly linearly, reaching 0.8 Ω at the end of discharge at 10% SOC. In figure 2f, we can distinguish between two main types of resistance contribution. There is a base resistance

of around 0.6 Ω (~2 Ωcm^2) that is always present, independent of SOC. It is composed of the resistance related to the wiring and connectors of our experimental cell, contacting of the active materials, as well as the resistivity of the employed Na-β"-alumina solid electrolyte. We measured the resistivity of our Na-β"-alumina solid electrolyte as a function of temperature and found a value of 5 Ωcm at 300 °C (see figure 5-13). Given the dimensions of the solid electrolyte (area 3.14 cm^2, thickness 0.1 cm), this translates into a resistance contribution of 0.16 Ω. Furthermore, the resistance associated with the anode reaction and interface can be considered to contribute to the base resistance, since it was shown in ref. 31 that the anode resistance is practically SOC-independent as long as few percent of the total Na amount remain in the anode, which is the case in our experiments. The present base resistance compares well to the values obtained in ref. 31, where symmetrical cells composed of Na-β"-alumina solid electrolytes sandwiched between Na were studied at 250 °C, and cell resistances of around 0.43 Ω (~1.3 Ωcm^2) were measured. In addition to the base resistance, we have to consider an SOC-dependent, variable resistance that is responsible for the non-monotonic behavior of the resistance vs. SOC as shown in figure 5-2d. To understand this non-monotonic cell resistance behavior, we propose a schematic as shown in figure 5-3c-d. The schematic focuses on the cathode, since it is the cathode where the SOC-dependence of the resistance originates. In figure 5-3c, we sketch a cross-sectional view of the cathode at around 70% SOC. At this point, where the discharge is in an early stage, the NiCl$_2$ dechlorination reaction was initiated at the solid electrolyte interface and progresses away from the solid electrolyte towards the current collector along the depth of the cathode. As a result, the ionic transport path for the reaction (NiCl$_2$ + 2 Na → Ni + 2 NaCl) increases, since the Na ions have to travel from the solid electrolyte interface where they enter the cathode through the NaAlCl$_4$ until they reach the reaction site. This longer travel path results in increased overpotentials and therefore increased resistance. The resistance associated with the Na ion transport can be estimated based on the resistivity of the NaAlCl$_4$. At a temperature of 300 °C, the resistivity of NaAlCl$_4$ is 0.78 Ω cm.[36] Considering a cathode filling of 1 g cathode granules (containing Ni, Fe, Al, NaCl, and additives, but excluding the NaAlCl$_4$), a measured tap density of the granulated cathode material of ~2 g cm^{-3}, a density of the cathode granules of 3.9 g cm^{-3} computed based on the granule composition, we obtain a cathode granule thickness of 1.6 mm at a porosity of around 50%. The pores between the granules are filled with the molten NaAlCl$_4$. This results in an effective cross section of the NaAlCl$_4$ for the Na ion transport of ~1.5 cm^2. The resistance to expect for the Na ion transport through the NaAlCl$_4$ is computed based on the NaAlCl$_4$ resistivity multiplied by the transport length divided by the effective cross sectional area. The Na ion transport resistance scales linearly with the transport length, where the ionic resistance vanishes directly at the solid electrolyte interface since the transport length is zero, while it reaches a maximum at the current collector where the Na ions have to travel through the entire cathode starting from the solid electrolyte. Based on the depth of the

cathode (1.6 mm) and the effective cross-sectional area of the $NaAlCl_4$ of 1.5 cm^2, the resistance resulting from the Na ion transport through the entire depth of the cathode at the end of the Ni dechlorination voltage plateau is ~0.13 Ω. The result compares well in order of magnitude with the observed rise in resistance at the end of the Ni plateau by ~0.3 Ω. When taking into account increased transport lengths due to tortuosity within the granulated cathode structure, the estimated resistance would further rise. At the end of the Ni plateau, when the overpotentials lowered the cell voltage to levels below values of roughly 2.32 V, the $FeCl_2$ dechlorination reaction can be initiated. In figure 3d, we sketch the discharge situation at around 15% SOC. At this stage, the $NiCl_2$ dechlorination reaction reaches far into the cathode so that substantial overpotentials arise. Simultaneously, the $FeCl_2$ dechlorination reaction was initiated at the solid electrolyte interface, thereby providing very short ionic transport paths and therefore low resistance. As discharge continues, similar to the $NiCl_2$ dechlorination reaction, the reaction front has to progress away from the solid electrolyte into the depth of the cathode to find the $FeCl_2$ required for the reaction ($FeCl_2$ + 2 Na → Fe + 2 NaCl). The associated longer ionic transport paths again lead to an increase in the resistance. We can conclude that modelling the cathode discharge reaction with our proposed simple approach based on a reaction front mechanism[2] is well explaining the observed, non-monotonic resistance behavior. The obtained mechanistic insight enables us to understand why a mixed cathode with Fe and Ni can be beneficial for specific conditions and how cathodes can be tailored to different demands in specific power and specific energy.

Furthermore, the determined cell resistance combined with equation 40 enables us to determine the OCV during discharge by simply extrapolating from the four averaged discharge traces shown in figure 5-9c to a current density of 0 mA cm^2. This is justified due to the linearity of the increase in overpotential as shown in figure 5-9d. We show the resulting discharge OCV vs. specific capacity and SOC in figure 5-17.

Supporting information note 3: Granulation

To probe the effect of cathode granulation and microstructure, we also studied a cell with a non-granulated cathode (Cell E). To this end, we used the cathode material in a pellet-shape instead of as granules. The cathode material pellets are an intermediate product during cathode granule fabrication. After mixing the raw materials and compacting them in the laboratory roller press, the cathode material is in the shape of flakes (or large pellets). These flakes are approximately 2 mm thick and up to a few cm^2 in area. Out of one of these larger flakes we cut a disc-shaped pellet with approximately 19 mm diameter and 2 mm thickness, see figure 5-10a-b. The weight of the pellet was 1.317 g and it contained the same composition as the Fe/Ni cathode granules. BET measurements revealed a surface area of approximately 1.1 m^2 g^{-1} for the Fe/Ni pellet, which is very similar to the granulated Fe/Ni cathode material. We added 0.659 g of $NaAlCl_4$ via vacuum infiltration. Everything else remained unchanged as compared with the cell assembly procedure outlined in the

Experimental Section. The theoretical reversible capacity of the cell with the cathode pellet was 209 mAh (i.e. 159 mAh g^{-1}). The theoretical irreversible contribution due to reaction 8 was 20 mAh (i.e. 15 mAh g^{-1}). Therefore, in maiden charge, we attempted to charge the cell with the pellet up to a total of 230 mAh (i.e. 174 mAh g^{-1}). In figure 5-10c we show the results of the maiden charge. While a cell with a granulated Fe/Ni cathode shows two pronounced voltage plateaus during maiden charge associated with reaction 9 and reaction 10, the voltage trace of the cell with a non-granulated Fe/Ni cathode is less clearly defined. Throughout the entire maiden charge, the overpotentials are substantially higher for the non-granulated cathode compared to the granulated counterpart. Especially at high SOC, the overpotentials rise substantially for the non-granulated cathode up to levels where the upper cutoff voltage of 2.75 V is reached. Therefore, the maiden charge had to be stopped at 95% SOC. The comparison between a granulated and a non-granulated cathode shows that while the provided specific surface area is not affected by granulation, the observed overpotentials strongly depend on granulation. While in the granulated case there are NaAlCl$_4$-filled channels between the cathode granules that ensure an efficient ion transport (especially Na ions from the reaction site to the solid electrolyte), such channels are missing in the non-granulated pellet. Therefore, the resistance rises drastically especially at high SOC for the non-granulated case, while it remains almost constant for the granulated case. This simple comparison illustrates the importance of the cathode granulation process and the appropriate balance between porosity (for good ionic transport) and electronic backbone (for good electric conductivity through the cathode).
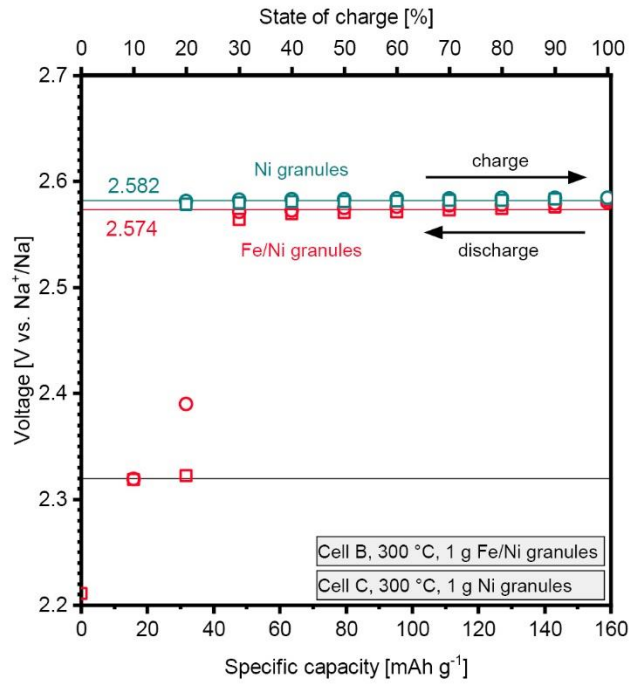
Figure 5-8: Open circuit voltage (OCV) determined based on galvanostatic intermitted titration technique (GITT). Comparison between the Fe/Ni cathode (red color) and the Ni cathode (blue color). Circles and squares represent the results from charge and discharge, respectively. OCV is measured after one hour of cell relaxation. On average, the OCV in the high-voltage plateau is 2.574 V for the Fe/Ni cathode vs. 2.582 V for the Ni cathode.
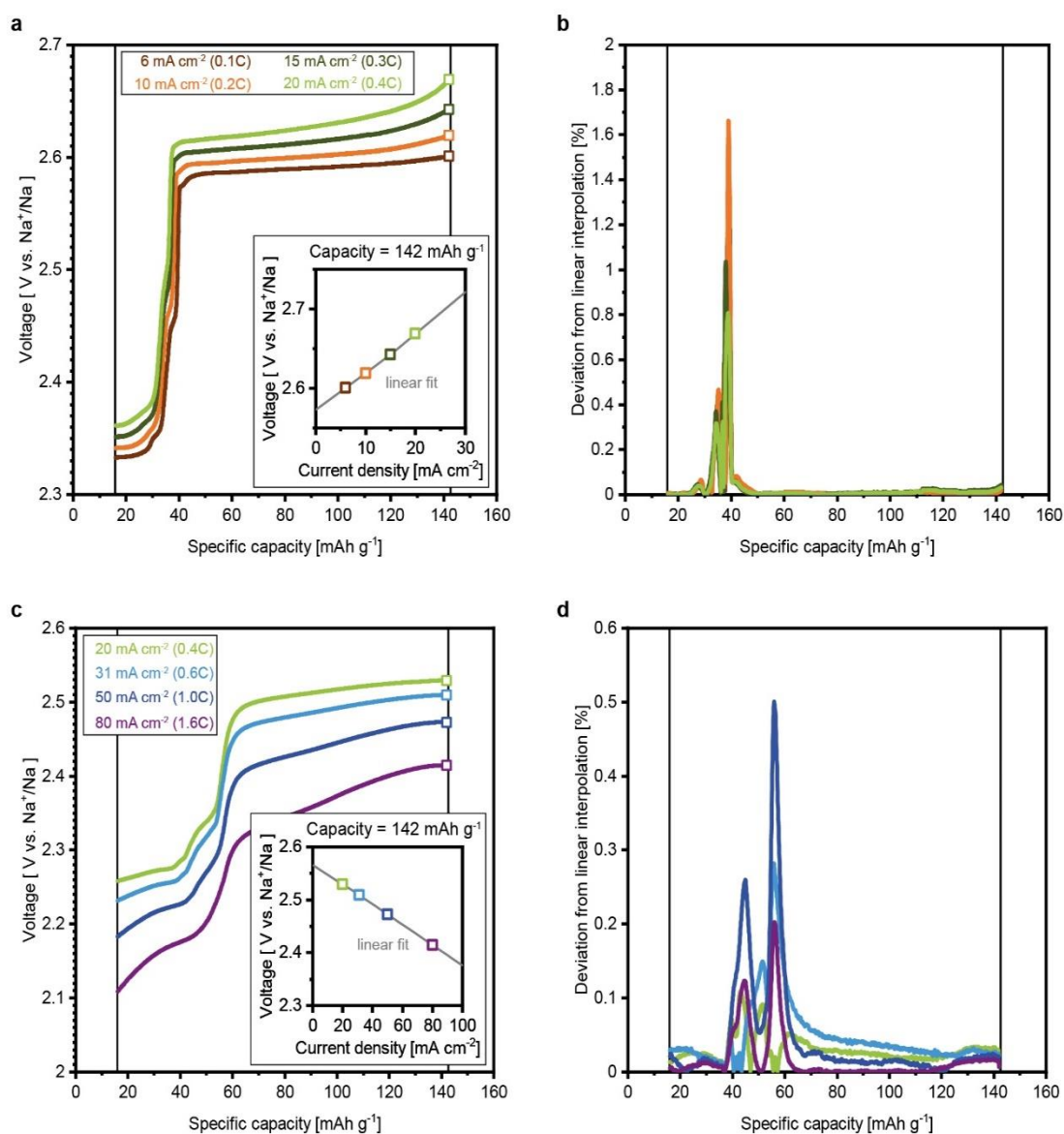
Figure 5-9: Cell resistance computation for Fe/Ni cathodes. a) Average charge voltage vs. specific capacity computed from the three voltage traces per charge current as shown in figure 5-2c. The color code is the same as introduced in figure 5-2. Inset: Example for a linear interpolation performed between the voltage traces, here at a specific capacity of 142 mAh g⁻¹. b) Deviation from the linear interpolation between the four averaged charge voltage traces as shown in a, as a function of specific capacity. c) Average discharge voltage vs. specific capacity computed from the three voltage traces per discharge current as shown in figure 5-2d. Inset: Example for a linear interpolation performed between the voltage traces, here at a specific capacity of 142 mAh g⁻¹. d) Deviation from the linear interpolation between the four averaged discharge voltage traces as shown in c, as a function of specific capacity.
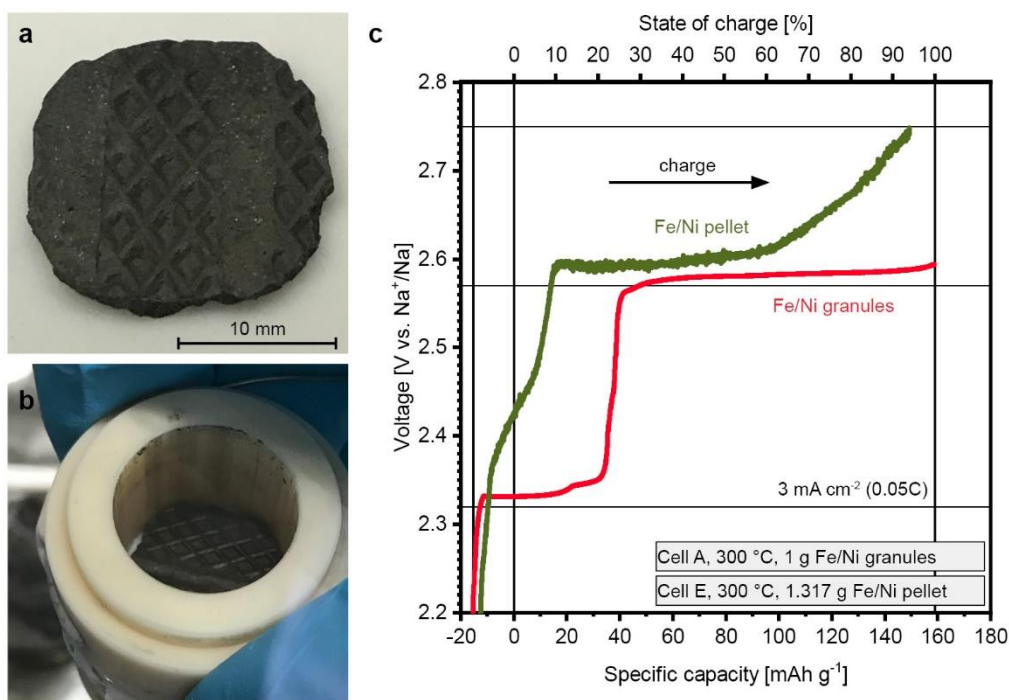
Figure 5-10: Cell with a non-granulated Fe/Ni cathode pellet. a) Photograph of the non-granulated Fe/Ni cathode pellet. b) Photograph of the Fe/Ni cathode pellet inside the ceramic subassembly before NaAlCl₄ vacuum infiltration. c) Cell voltage vs. specific capacity during maiden charge of the cell with a Fe/Ni cathode pellet as compared to a cell with a granulated Fe/Ni Cathode. The maiden charge of the cell with the Fe/Ni pellet was stopped at 95% SOC, when the upper cutoff voltage of 2.75 V was reached.
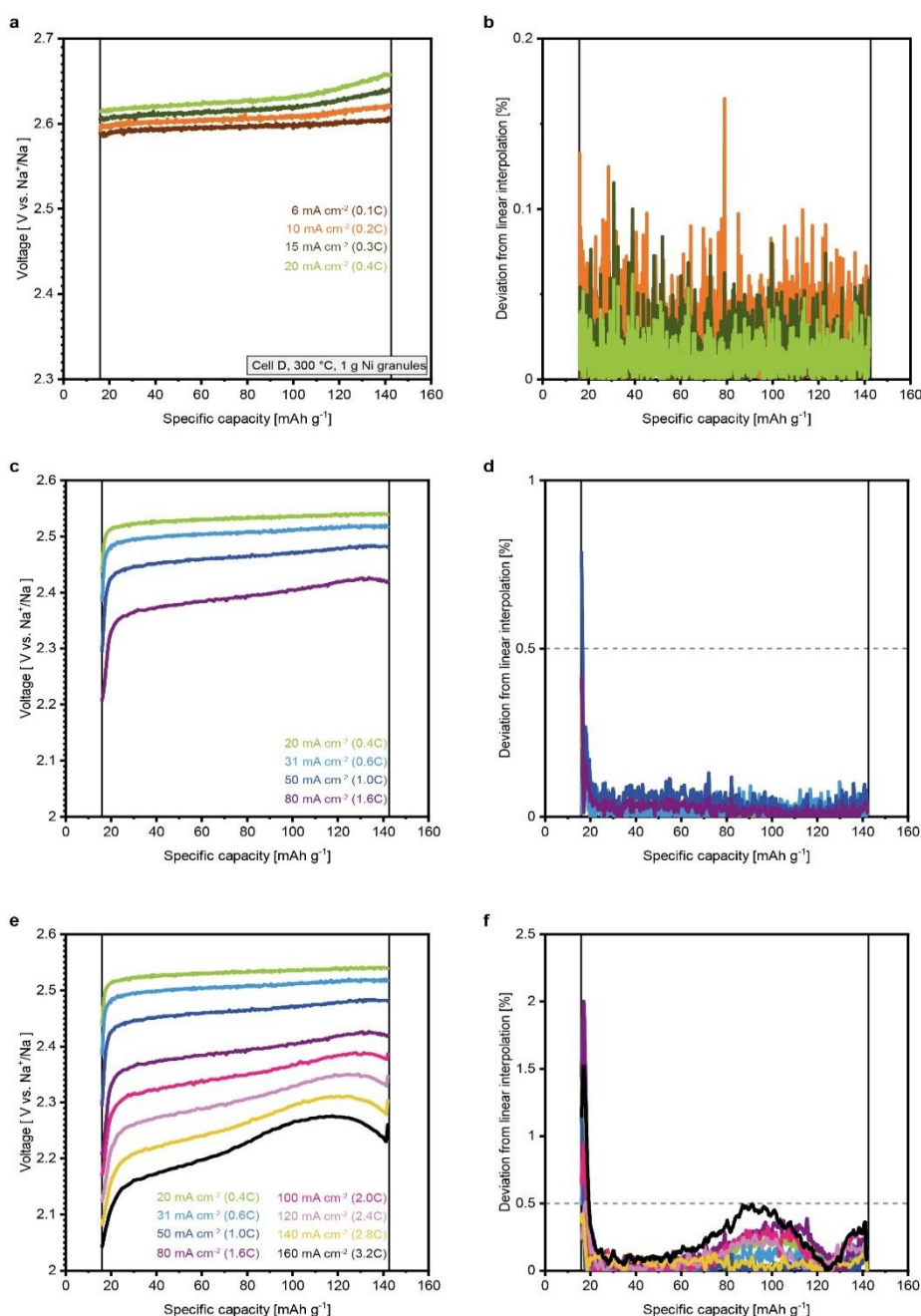
Figure 5-11: Cell resistance computation for pure Ni cathodes. a) Average charge voltage vs. specific capacity computed from the three voltage traces per charge current as shown in figure 5-4c. b) Deviation from the linear interpolation between the four averaged charge voltage traces shown in a), as a function of specific capacity. c) Average discharge voltage vs. specific capacity computed from the three voltage traces per discharge current as shown in figure 5-4d, considering current densities between 20 and 80 mA cm⁻². d) Deviation from the linear interpolation between the four averaged discharge voltage traces shown in c, as a function of specific capacity. e) Average discharge voltage vs. specific capacity computed from the three voltage traces per discharge current as shown in figure 5-4d, considering current densities between 20 and 160 mA cm⁻². f) Deviation from the linear interpolation between the eight averaged discharge voltage traces shown in e, as a function of specific capacity.
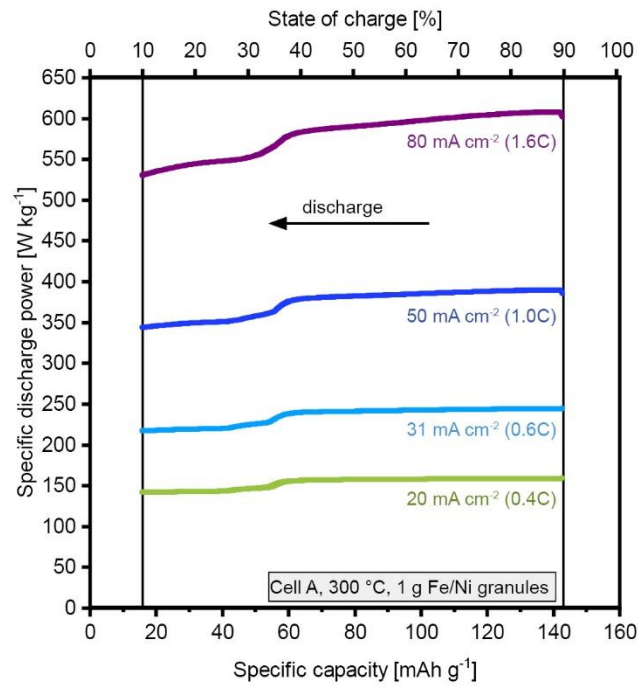
Figure 5-12: Specific discharge power vs. specific capacity during the discharge rate test as introduced in figure 5-2d for the Fe/Ni cathode.
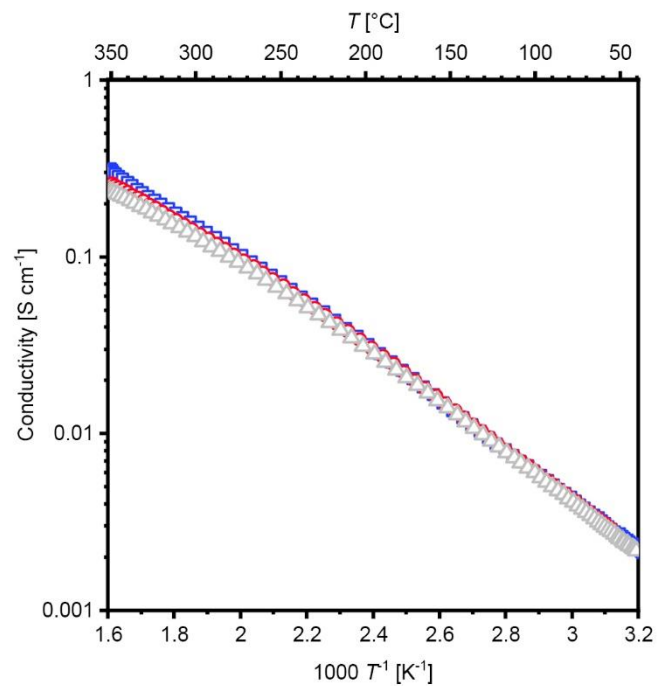
Figure 5-13: Conductivity of Na-β''-alumina solid electrolyte as a function of temperature. Three independent measurements.

Element	Norm. amount [wt.%]	Error [%]
Na	30.65	2.09
Cl	23.42	0.87
Ni	38.94	1.32
Fe	6.90	0.24
Al	0.08	0.03
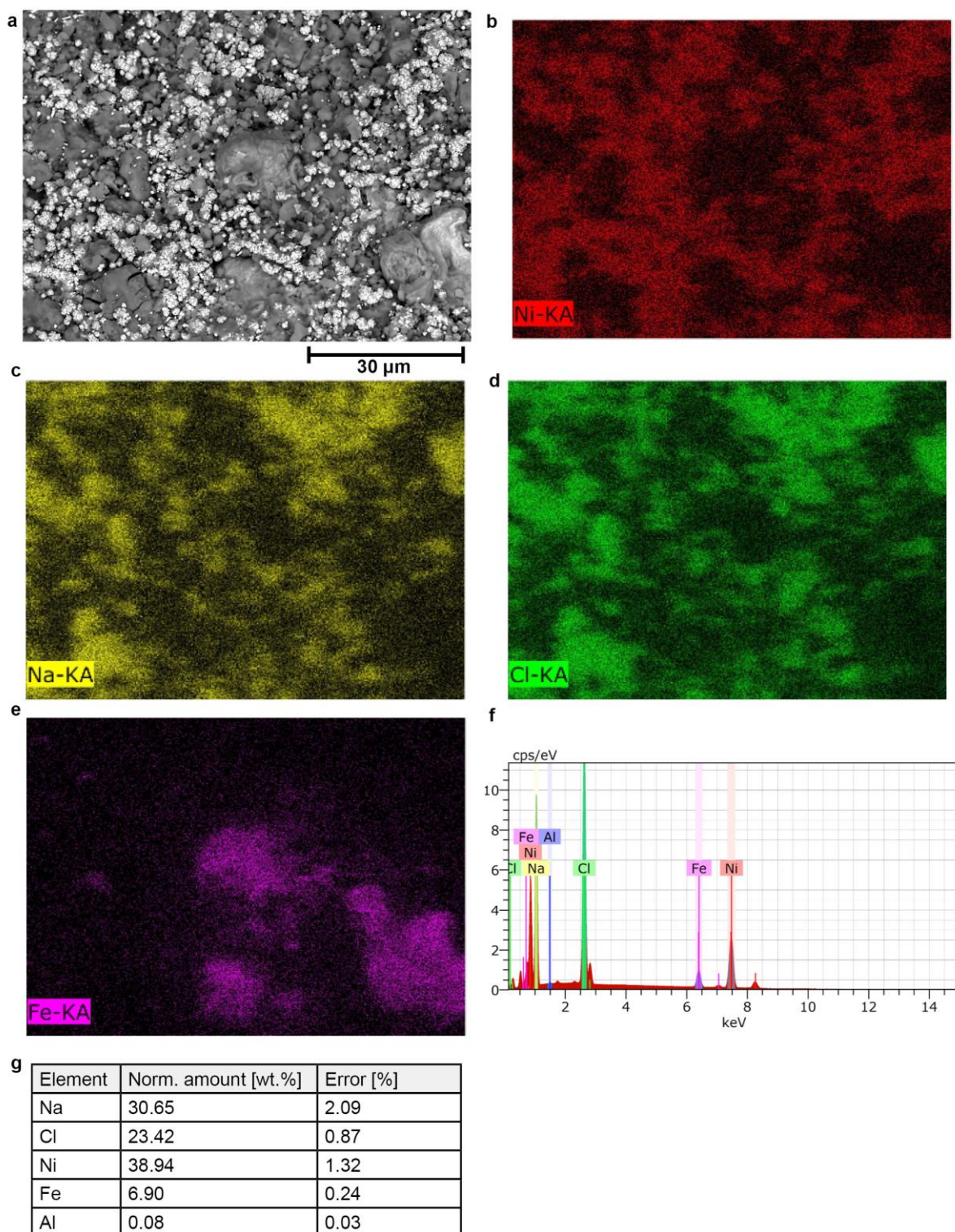
Figure 5-14: Microstructure and composition of Fe/Ni granules, obtained via scanning electron microscopy (SEM) and energy-dispersive X-ray spectroscopy (EDS).
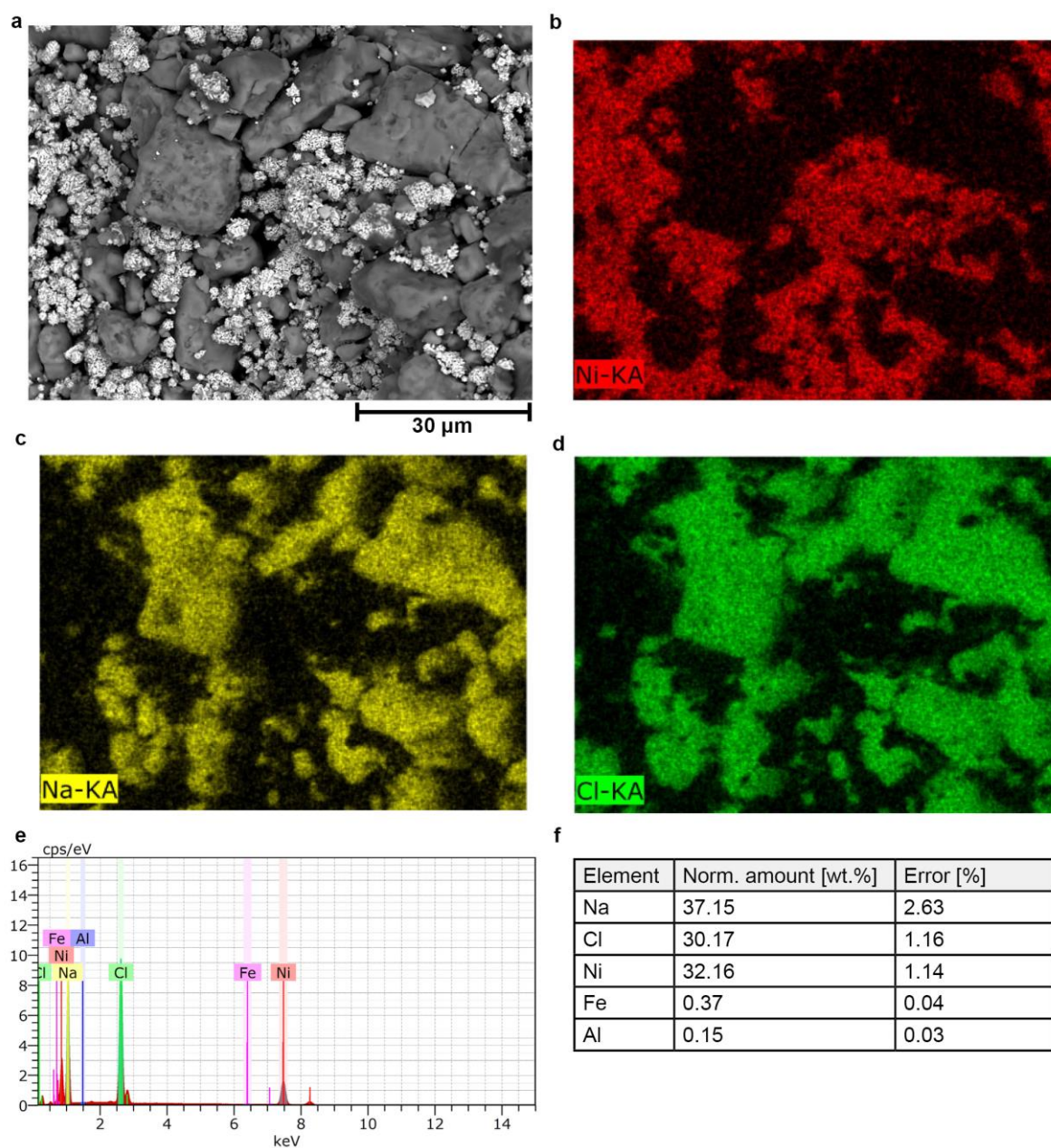
Figure 5-15: *Microstructure and composition of Ni granules, obtained via scanning electron microscopy (SEM) and energy-dispersive X-ray spectroscopy (EDS).*

Element	Norm. amount [wt.%]	Error [%]
Na	37.15	2.63
Cl	30.17	1.16
Ni	32.16	1.14
Fe	0.37	0.04
Al	0.15	0.03
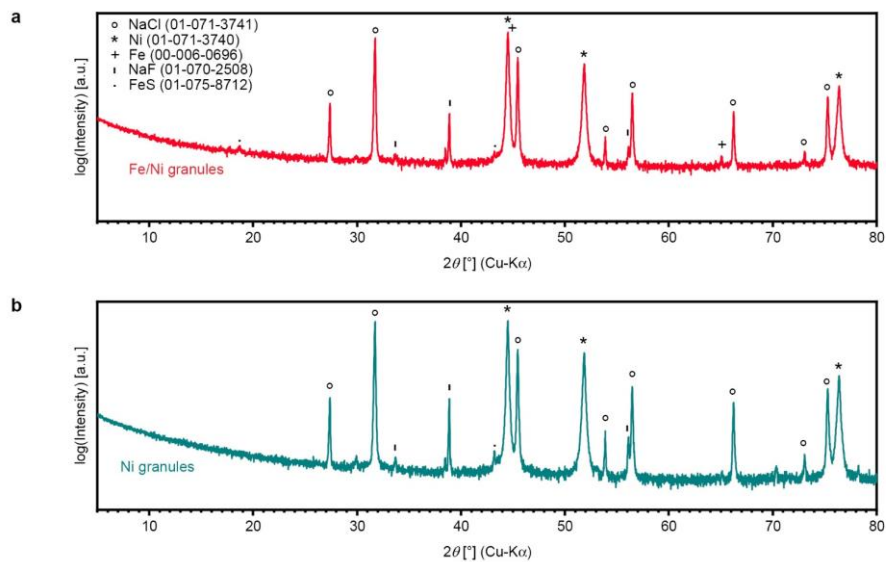
Figure 5-16: X-ray powder diffraction (XRD) analysis of the cathode materials. a) Fe/Ni granules. b) Ni granules.
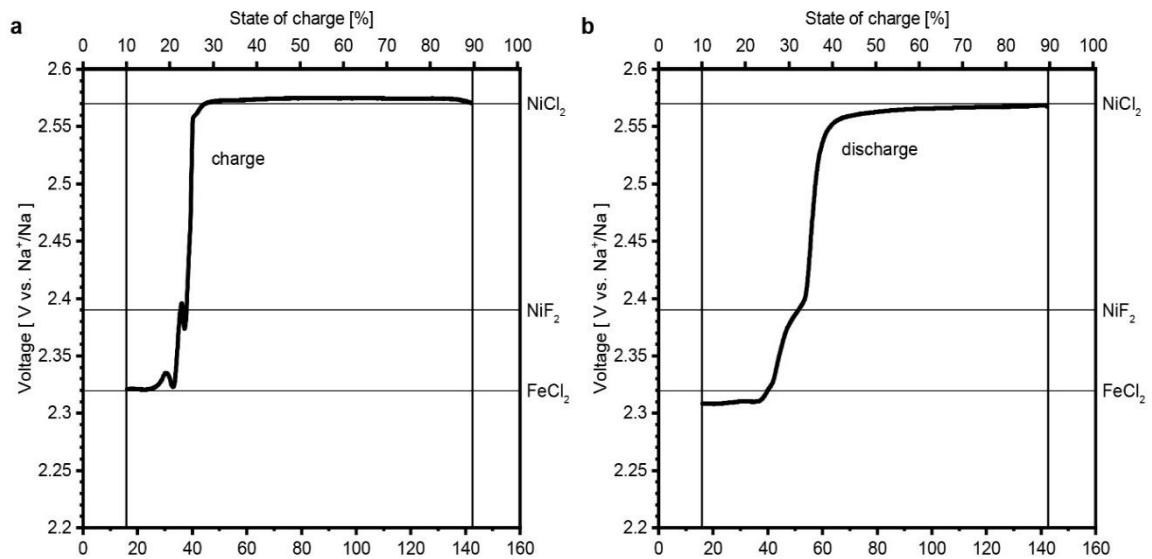
Figure 5-17: Effective cell voltage of Fe/Ni cathode at 0 mA cm-2. a) Cell voltage obtained from linear extrapolation to 0 mA cm^{-2} (equation 40) based on the charge voltage traces presented in Figure 5-2c. Horizontal lines at 2.32 V, 2.39 V, and 2.57 V highlight the equilibrium potentials of the associated cell reactions, namely Fe + 2 NaCl $\leftrightarrow$ FeCl$_2$ + 2 Na (reaction 9), Ni + 2 NaF $\leftrightarrow$ NiF$_2$ + 2 Na (additive reaction), and Ni + 2 NaCl $\leftrightarrow$ NiCl$_2$ + 2 Na (reaction 10), respectively. b) Cell voltage obtained from linear extrapolation to 0 mA cm^{-2} (equation 40) based on the discharge voltage traces presented in figure 5-2d.

Ref.	Cycles [nbr]	Specific discharge power [W kg^{-1}]	Specific discharge energy [Wh kg^{-1}]	Areal capacity [mAh cm^{-2}]
7	300	73.2	219.6	52.3
8	150	72.3	133	83.3
9	60	73.8	152	52.3
	60	220.5	148	52.3
10	100	43.7	137	54
11	200	59.25	295	53.6
12	100	71.7	215.1	52.3
13	10	225	268.7	52
	10	300	253.0	52
	9	450	200.8	52
	9	750	157.5	104
	9	112.5	259.7	104
	9	150	247.3	156
	10	75	266.1	156
	10	100	243.2	156
14	1	43.7	284.1	52.7
	1	65.25	281.6	52.7
	1	129.6	276.3	52.7
	1	193.05	270.9	52.7
	1	255.6	259.0	52.7
	1	316.5	243.2	52.7
	1	43.5	305.6	52.7
	1	64.95	300.8	52.7
	1	127.5	291.9	52.7
	1	188.1	283.8	52.7
	1	247.2	273.2	52.7
	1	303.75	255.8	52.7
	350	65.25	350	52.7
15	10	75.6	226.8	52.3
16	300	52.56	330	65.3
	300	59.32	380	65.3
	300	65.25	405	65.3
	300	72	200	65.3
17	60	75.75	227.25	52.3
	60	72.75	218.25	52.3
	60	64.5	193.5	52.3
18	200	68.7	340	52.3
	200	68.25	258	52.3
19	50	21.92	194.8	50

Table 5-1: Data extracted from literature used for comparison in figure 5-6g.

References

[1]   J. L. Sudworth, *J. Power Sources* 1994, *51*, 105.

[2]   J. Sudworth, *J. Power Sources* 2001, *100*, 149.

[3]   C.-H. Dustmann, *J. Power Sources* 2004, *127*, 85.

[4]   S. F. Schneider, C. Bauer, P. Novák, E. J. Berg, *Sustain. Energy Fuels* 2019, *3*, 3061.

[5]   C. Vaalma, D. Buchholz, M. Weil, S. Passerini, *Nat. Rev. Mater.* 2018, *3*, 18013.

[6]   M. V. F. Heinz, G. Graeber, D. Landmann, C. Battaglia, *J. Power Sources* 2020, *465*, 228268.

[7]   H. J. Chang, X. Lu, J. F. Bonnett, N. L. Canfield, S. Son, Y.-C. Park, K. Jung, V. L. Sprenkle, G. Li, *J. Power Sources* 2017, *348*, 150.

[8]   H.-J. Chang, N. L. Canfield, K. Jung, V. L. Sprenkle, G. Li, *ACS Appl. Mater. Interfaces* 2017, *9*, 11609.

[9]   G. Li, X. Lu, J. Y. Kim, J. P. Lemmon, V. L. Sprenkle, *J. Mater. Chem. A* 2013, *1*, 14935.

[10]   G. Li, X. Lu, J. Y. Kim, V. V. Viswanathan, K. D. Meinhardt, M. H. Engelhard, V. L. Sprenkle, *Adv. Energy Mater.* 2015, *5*, 1500357.

[11]   X. Zhan, M. E. Bowden, X. Lu, J. F. Bonnett, T. Lemmon, D. M. Reed, V. L. Sprenkle, G. Li, *Adv. Energy Mater.* 2020, *10*, 1903472.

[12]   G. Li, X. Lu, J. Y. Kim, J. P. Lemmon, V. L. Sprenkle, *J. Power Sources* 2014, *249*, 414.

[13]   X. Lu, H. J. Chang, J. F. Bonnett, N. L. Canfield, K. Jung, V. L. Sprenkle, G. Li, *J. Power Sources* 2017, *365*, 456.

[14]   K. Jung, H.-J. Chang, J. F. Bonnett, N. L. Canfield, V. L. Sprenkle, G. Li, *J. Power Sources* 2018, *396*, 297.

[15]   G. Li, X. Lu, J. Y. Kim, M. H. Engelhard, J. P. Lemmon, V. L. Sprenkle, *J. Power Sources* 2014, *272*, 398.

[16]   H.-J. Chang, X. Lu, J. F. Bonnett, N. L. Canfield, S. Son, Y.-C. Park, K. Jung, V. L. Sprenkle, G. Li, *Adv. Mater. Interfaces* 2018, *5*, 1701592.

[17]   X. Lu, G. Li, J. Y. Kim, J. P. Lemmon, V. L. Sprenkle, Z. Yang, *J. Power Sources* 2012, *215*, 288.

[18]   G. Li, X. Lu, J. Y. Kim, K. D. Meinhardt, H. J. Chang, N. L. Canfield, V. L. Sprenkle, *Nat. Commun.* 2016, *7*, 10683.

[19]   G. Li, X. Lu, C. A. Coyle, J. Y. Kim, J. P. Lemmon, V. L. Sprenkle, Z. Yang, *J. Power Sources* 2012, *220*, 193.

[20]   M. Uitz, M. Sternad, S. Breuer, C. Täubert, T. Traußnig, V. Hennige, I. Hanzu, M. Wilkening, *J. Electrochem. Soc.* 2017, *164*, A3503.

[21]   Y. Kuang, C. Chen, D. Kirsch, L. Hu, *Adv. Energy Mater.* 2019, *9*, 1901457.

[22]   R. C. Galloway, S. Haslam, *J. Power Sources* 1999, *80*, 164.

[23]   C.-W. Ahn, M. Kim, B.-D. Hahn, I. Hong, W. Kim, G. Moon, H. Lee, K. Jung, Y.-C. Park, J.-H. Choi, *J. Power Sources* 2016, *329*, 50.

[24] R. Benato, N. Cosciani, G. Crugnola, S. Dambone Sessa, G. Lodi, C. Parmeggiani, M. Todeschini, *J. Power Sources* 2015, *293*, 127.

[25] J. Rijssenbeek, H. Wiegman, D. Hall, C. Chuah, G. Balasubramanian, C. Brady, in *2011 IEEE 33rd Int. Telecommun. Energy Conf.*, IEEE, 2011, pp. 1–4.

[26] V. Zinth, S. Seidlmayer, N. Zanon, G. Crugnola, M. Schulz, R. Gilles, M. Hofmann, *J. Electrochem. Soc.* 2015, *162*, A384.

[27] C. Daniel, J. O. Besenhard, *Handbook of Battery Materials*, Wiley-VCH Verlag GmbH & Co. KGaA, Weinheim, Germany, 2011.

[28] R. J. Bones, J. Coetzer, R. C. Galloway, D. A. Teagle, *J. Electrochem. Soc.* 1987, *134*, 2379.

[29] T. Javadi-Doodran, Microstructure and conductivity of the sodium-nickel-chloride (ZEBRA) battery cathode, McMaster University, 2012.

[30] R. Christin, Multiphysics Modeling of Sodium-nickel-chloride Cells, Université Grenoble Alpes, 2015.

[31] D. Landmann, G. Graeber, M. V. F. Heinz, S. Haussener, C. Battaglia, *Mater. Today Energy* 2020, *18*, 100515.

[32] T. Javadi, A. Petric, *J. Electrochem. Soc.* 2011, *158*, A700.

[33] G. P. Power, I. M. Ritchie, *J. Chem. Educ.* 1983, *60*, 1022.

[34] M.-C. Bay, M. V. F. Heinz, R. Figi, C. Schreiner, D. Basso, N. Zanon, U. F. Vogt, C. Battaglia, *ACS Appl. Energy Mater.* 2019, *2*, 687.

[35] C. H. Hamann, A. Hamnett, W. Vielstich, in *Electrochemistry*, 2007.

[36]   K. S. Mohandas, N. Sanil, P. Rodriguez, *Min*

6. Pressure management and cell design in solid-electrolyte batteries, at the example of a sodium-nickel-chloride battery [*]

Cells designs with planar Na-β"-alumina electrolytes are a key enabler to reduce cost of sodium-nickel-chloride batteries. In this study, we assess the mechanical stress induced by replacement of the conventional tubular Na-β"-alumina electrolyte by a planar design. Further, solutions to mitigate stress on the planar electrolyte are discussed.

Author contributions

M.H. conceived the idea for this study together with G.G., D.L., and C.B. M.H. performed the stress calculations together with G.G. and D.L. M.H. analyzed the results, prepared the figures, and wrote the manuscript. G.G., D.L., and C.B. critically reviewed and edited the manuscript. All coauthors read, commented, and approved the final manuscript.

Abstract

Solid electrolytes in combination with alkali-metal anodes offer the potential to enhance battery energy density and safety. The inherent challenges associated with cell pressure management have to be accounted for in the cell design but are not sufficiently understood. Here we present a theoretical study linking the effects of thermal and chemo-mechanical expansion of electrode materials to the stresses acting on tubular and planar solid electrolytes, at the example of the sodium-nickel-chloride battery chemistry. Based on our analysis, we derive three strategies to reduce these stresses. Namely, we propose (i) to increase the cell closing temperature during production, (ii) to reduce the gas pressure in the cell (e.g. by applying a vacuum) and (iii) to rationally balance the volume of the two electrode compartments. Mechanical considerations developed herein form the foundation for the development of next-generation battery cell designs.

6.1 Introduction

The demand for efficient and sustainable battery technologies is rapidly increasing. Solid-electrolyte batteries with alkali-metal electrodes are receiving much attention, as this combination promises enhanced battery energy density and safety.[1-4] Recent studies focused on enhancing bulk conductivity of solid electrolytes, reducing interfacial resistance between solid electrolytes and alkali-metal anodes, preventing dendrite formation, and improving alkali-metal plating/stripping efficiency.[5-7] Only a few reports address the chemo-mechanical analysis of solid-electrolyte batteries on cell level so far.[8-10] In solid-electrolyte batteries, the electrolyte serves both as ion conductor and as separator between anode and cathode, and is often the load-bearing structure.

The combination of alkali-metal anode and solid-electrolyte separator can be paired with a cathode incorporating either a liquid or a solid secondary electrolyte. Chemo-mechanical volume expansion of the cathode materials during charging/dicharging is a critical factor. Especially in combination with a solid secondary electrolyte, volume expansion of cathode materials leads to ionic contact loss during cycling causing rapid capacity fading.[8, 9] This is one of the main reasons, why all-solid-state batteries are still at a relatively early stage of development. A secondary electrolyte in the liquid state circumvents these challenges, but overall volume changes including the contribution of thermal expansion must be managed in both cases and taken into account in the battery cell design.

Two commercial battery technologies that employ a sodium-metal anode in combination with a solid electrolyte separator are sodium-sulfur (Na-S) and sodium-nickel-chloride (Na-NiCl$_2$) batteries operating at 300 °C. These batteries employ a ceramic Na-β''-alumina electrolyte, abundant, non-critical cathode materials, delivering near ideal faradaic efficiencies coupled with long shelf and cycle life (e.g. >15 years, 4500 cycles[11]). Na-S batteries for stationary applications feature large cells with up to 630 Ah capacity,[12] while Na-NiCl$_2$ cells tend to be smaller, with rated capacity of approximately 40 Ah.[13] In both cases, the cell design takes advantage of a tubular ceramic electrolyte geometry, which facilitates sealing and significantly reduces mechanical stresses acting on the ceramic electrolyte, compared to planar designs of the same active area. However, the tubular electrolyte shape complicates cell assembly and quality control procedures. Therefore, attempts are made to adopt a planar cell design also for high temperature sodium batteries.[14] While a planar design demands improved sealing technology, it enables application of high-volume manufacturing routines and potentially increases power and energy density of the cells.

For such batteries, it is important to consider the brittle nature of the ceramic electrolyte and to match cell design with tolerable failure rates. Recent numerical simulations on planar Na-β''-alumina geometries indicate that the mismatch of thermal expansion coefficients in the load bearing structures could lead to critical residual stresses upon thermal cycling during cell assembly and operation, even in the absence of electrode materials.[10]

Investigations on the crucial phenomena related to phase change and mass transport during electrochemical cycling resulting in pressure differences between electrode compartments are currently missing.

Here we investigate the effect of chemo-mechanical expansion of electrode materials by exemplarily comparing tubular and planar Na-NiCl$_2$ cells. Considering variable cell closure and operating temperatures between 25 °C and 600 °C, we discuss how both changes in temperature and electrochemical reactions cause considerable volume changes in the electrodes at different states of charge. These volume changes induce substantial pressure differences between the hermetically sealed electrode compartments, resulting in geometry-dependent stresses acting on the ceramic β''-alumina electrolyte. Based on our calculations, we derive design and operation guidelines for solid-electrolyte batteries.

6.2 Results and discussion

Pressure tolerance of different cell geometries

Pressure changes inevitably arise during operation of Na-NiCl$_2$ cells, as both electrochemical reactions and variations in temperature cause substantial volume changes of the electrode materials. During high-temperature battery operation, the anode material, sodium, is liquid, and the active cathode materials, mainly NiCl$_2$ and FeCl$_2$, are immersed in a molten secondary electrolyte based on NaAlCl$_4$. Loss of ionic contact between cathode materials and secondary electrolyte during cycling is therefore not an issue for Na-NiCl$_2$ cells. Indeed, the excellent long-term stability of high-temperature Na-NiCl$_2$ cells[15] proves that the functionality of electrode materials is not significantly impacted by these volume changes. Nevertheless, the resulting pressure changes in the hermetically sealed electrode compartments impose geometry dependent constraints on the cell design.

To illustrate this, we compare two simplified geometries for Na-NiCl$_2$ cells with the same capacity: one based on an electrolyte tube with hollow circular cross section and closed bottom (figure 6-1a, tubular cell), and one based on a circular electrolyte plate (figure 6-1b, planar cell). While the tubular cell design reflects the state-of-the-art in commercial cells,[11] the planar design is frequently discussed in research papers.[10, 14] Simultaneously, these geometries differ widely in their mechanical properties. Their comparison illustrates the general trend between more spherically-shaped, robust solid electrolytes and mechanically demanding planar geometries. Both cell designs feature the same active area A = 207.3 cm^2, the same electrolyte thickness t_e =0.15 cm, and the same effective compartment volumes, $V_{c,eff}$ = 163.1 cm^3 at the cathode, and $V_{a,eff}$ = 66.9 cm^3 at the anode (table 6-1 in supporting information), representing typical values of commercial tubular Na-NiCl$_2$ cells.

As ceramic Na-β''-alumina electrolytes are brittle, their mechanical properties are governed by the largest defects present. Thus, the maximum principal stress hypothesis,[16, 17]

determines the criterion for failure. For the tubular cell, the solid electrolyte conforms to a thin-walled cylindrical pressure vessel with closed bottom, dominated by (circumferential) hoop stress in a biaxial stress condition, σ_h.[18] This results in a relevant maximum stress $\sigma_{max,tubular}$ scaling with the pressure difference between the electrode compartments Δp, the tube radius r_{tube}, and the electrolyte thickness t_e according to

$$\sigma_{max,tubular} = \sigma_h = \frac{\Delta p \, r_{tube}}{t_e} \qquad \text{Equation 41}$$

Note that $\sigma_{max,tubular}$ is independent of the tube length, by which the electrolyte area can be increased without affecting its mechanical properties.

For the planar cell, we consider a thin circular plate with uniform load and clamped edges, dominated by radial stress, σ_r.[19] The resulting maximum principle stress (located along the edge) features a quadratic relation with the plate radius r_{plate} corresponding to

$$\sigma_{max,planar} = \sigma_r = \frac{3 \, \Delta p \, r_{plate}^2}{4 \, t_e^2} \qquad \text{Equation 42}$$

Compared to tubular cells of the same active area, planar cells thus feature drastically increased maximum stresses on their electrolyte structure, when subjected to pressure. For the simplified geometries in figure 6-1, this amounts to $\sigma_{max,tubular} \approx 12 \, \Delta p$ and $\sigma_{max,planar} \approx 2200 \, \Delta p$.

We illustrate equation 42 (planar cell geometry) by plotting the relation between cell geometry (r_{plate}, A, t_e) and Δp for different σ_{max} in figure 6-2. To avoid failure of the solid electrolyte, its fracture strength $\sigma_{fracture}$ must surpass the maximum stress σ_{max} at all times. In terms of cell design, this involves a limitation of the geometrical parameters (r_{plate}, A, t_e), respecting both the fracture strength $\sigma_{fracture}$ of the electrolyte, and the pressure differences Δp occurring in the cell during processing and operation. While Na-β''-alumina features an elastic modulus on the order of hundred GPa,[20] like most ceramics, its fracture strength is significantly lower. Average $\sigma_{fracture}$ values reported for Na-β''-alumina ceramics range from 100 MPa to 300 MPa.[21] Assuming $\sigma_{fracture} = 200$ MPa, pressure differences Δp must thus not exceed 0.9 bar to avoid failure of the planar geometry in figure 6-1b (P$_1$ in figure 6-2a, $t_e = 0.15$ cm). However, it is important to take into account that fracture strength of brittle materials depends on the size distribution of defects as described by the Weibull theory. [22] Based on their characteristic fracture strength, σ_0, and Weibull modulus, m, ceramic electrolytes feature a certain failure probability also at stresses well below their average fracture strength $\sigma_{fracture}$. Thus, with lower σ_{max} values of e.g. 50 and 10 MPa, tolerable Δp decrease to 0.2 bar and 45 mbar, respectively (P$_2$ and P$_3$ in figure 6-1b). This affects the scrap rates in cell production and is of particular importance when considering the cell design for large-scale batteries comprising thousands of cells.

Restrictions on Δp become even more stringent for thinner electrolytes, with pressure differences Δp limited to below 16 mbar for $t_e = 200$ μm (0.02 cm, P$_4$ in figure 6-2b). This

demonstrates that electrolyte thicknesses around 20 µm (0.002 cm), as typically applied for separators in liquid electrolyte batteries, are not easily accessible for solid electrolyte cells: Even for small cells with 3 cm^2 active area, pressure differences must not exceed 11 mbar (P5 in figure 6-2b). Pressure evolution is thus a decisive aspect limiting active area and capacity in the design of planar battery cells. In the following, we assess the volume changes of the electrode materials in Na-NiCl$_2$ batteries and their effect on evolution of cell pressure during operation in more detail.

a) tubular cell

top view

$r = 1.73$ cm
$= r_c + 0.5\, t_e$

cathode
electrolyte
anode

$A = 207.3$ cm^2

$\sigma_{max,\,tubular} \approx 12\,\Delta p$

side view

$l = 20$ cm

b) planar cell

top view

$r = 8.12$ cm

$A = 207.3$ cm^2

$\sigma_{max,\,planar} \approx 2200\,\Delta p$

side view
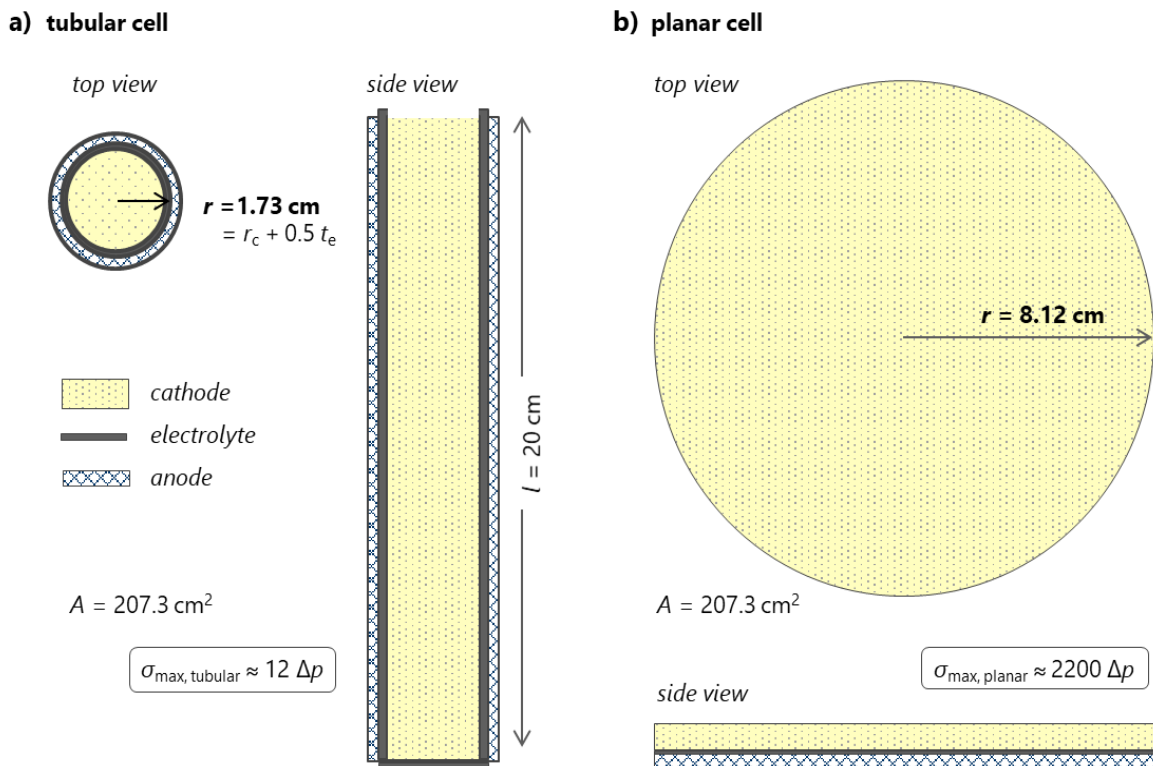
Figure 6-1: Geometries of simplified Na-NiCl$_2$ cells, with a) tubular cell geometry (hollow circular cross section with closed bottom), and b) planar cell geometry (circular electrolyte).
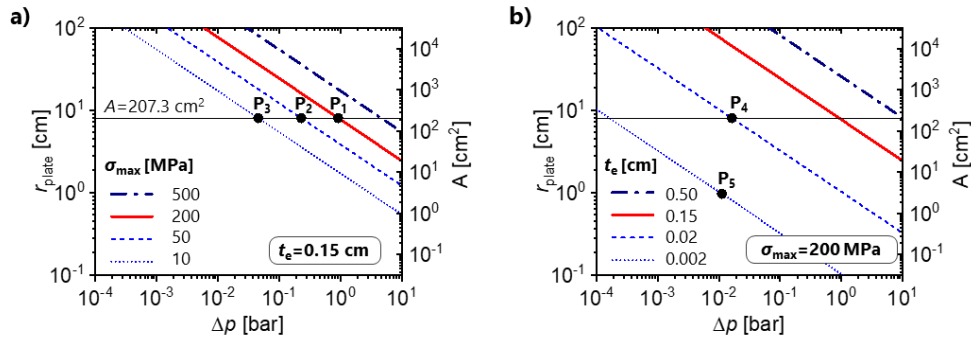
Figure 6-2: Restrictions on planar cell geometry (r_{plate}, A, t_e) as a function of pressure difference Δp and maximum tolerable stress σ_{max}. a) Influence of variable σ_{max} at constant electrolyte thickness, t_e = 0.15 cm. b) Influence of t_e at constant σ_{max} = 200 MPa. Radius and area ($A = 207.3 \ cm^2$) corresponding to the planar geometry of figure 6-1b are marked in both plots.

Volume changes of electrode materials and evolution of cell pressure during operation

State-of-the-art Na-NiCl$_2$ cells are assembled in the discharged state, with a cathode composed mainly of NaCl, Ni, Fe and a molten secondary electrolyte based on NaAlCl$_4$, but with no anode material present. The liquid sodium anode forms electrochemically upon charging. The charging reaction thus implies a net transport of sodium from cathode to anode, accompanied by a conversion reaction of Ni and Fe to NiCl$_2$ and FeCl$_2$, respectively. As a result, the volumes of cathode and anode materials $V_{m,c}$ and $V_{m,a}$ vary with the state of charge (SOC, see figure 6-3a). To maintain a constant active area of the battery cells during operation, wetting layers[23] in combination with metal shims are applied at the anode for current collection.[24, 25] At the cathode, the current collector is combined with a highly porous carbon felt, which provides a reservoir for liquid NaAlCl$_4$.[15] Here, we assume a simplified cathode composition comprising the active components Ni, Fe, Al, and NaCl as summarized in table 6-2a. This composition includes 70 wt% of excess Ni (relative to NaCl) to assure a stable conductive backbone.[24, 26] Iron and aluminum amount to 20% and 5% of the electroactive Ni species, respectively. The volume of NaAlCl$_4$ equals the volume of the cathode materials at 300 °C (see section A in supporting information). For simplicity, we omit common additives vital for cell functionality such as FeS, NaF, NaI, as they occur only in small quantities. We consider the following electrochemical reactions for 250 g of cathode material, resulting in a total capacity of 47.5 Ah. This corresponds to a rated capacity of 40 Ah after maiden cycling, where the added capacity ensures wetting of the anode with liquid sodium during subsequent cycles.

Pre-charge reaction:

Al + 4 NaCl $\leftrightarrow$ NaAlCl$_4$ + 3 Na	1.60 V (2.8 Ah, up to 6% SOC)	Reaction 11

Normal operation:

Fe + 2 NaCl $\leftrightarrow$ FeCl$_2$ + 2 Na	2.35 V (7.4 Ah, up to 22% SOC)	Reaction 12
Ni + 2 NaCl $\leftrightarrow$ NiCl$_2$ + 2 Na	2.58 V (37.2 Ah, up to 100% SOC)	Reaction 13
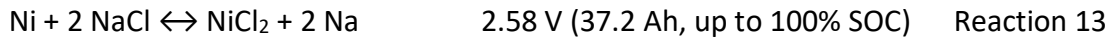
The pre-charge reaction (reaction 11) based on aluminum is normally activated only during maiden charge in state-of-the-art Na-NiCl$_2$ batteries. Due to its low voltage of 1.6 V, it provides the first layer of sodium at the anode, improving the conductive path to the current collector.[13] Normal charge/discharge operation is based on iron and nickel charging as introduced in reactions 12 and 13.
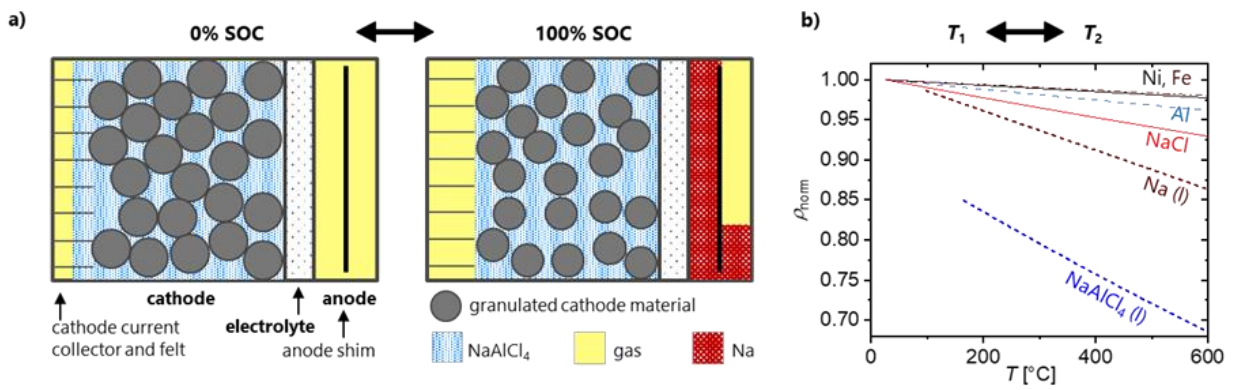
Figure 6-3: Origin of volume changes in the Na-NiCl$_2$ system. a) The volume of the electrode materials changes at different state of charge (SOC) due to electrochemical reactions (reactions 11-13). b) Volumetric variation further occurs due to density changes of the electrode materials with temperature. Here, densities of electrode materials are normalized to their respective room temperature values to obtain ρ_{norm}.

Apart from material transport and electrochemical reactions, volume changes arise due to temperature differences, e.g. between cell fabrication and closure at T_1 and battery operation at T_2. While the influence of thermal expansion on the solid electrode components (e.g. NaCl, Al, Ni, Fe) is relatively small, the densities of the molten components NaAlCl$_4$ and sodium decrease substantially with temperature (figure 6-3b; see table 6-2b for absolute densities). These materials also undergo a phase change from solid to liquid between room temperature and operating temperature (T_{melt}(NaAlCl$_4$)=157 °C, T_{melt}(Na)=98 °C). As a result, their densities decrease from 2.01 g cm^{-3} to 1.60 g cm^{-3} (NaAlCl$_4$) and from 0.97 g cm^{-3} to 0.88 g cm^{-3} (Na) between 25 °C and 300 °C, respectively (figure 6-10). Nor-

malized by their respective room temperature values, the densities of NaAlCl$_4$ and Na decrease by 31% and by 14% between 25 °C and 600 °C, those of NaCl by 7%, and those of Ni and Fe by 2% (figure 6-3b).

The volumetric evolution of cathode and anode materials resulting from both electrochemical reactions and temperature dependent densities are summarized in figure 6-4a for cell closure at T_1 = 25 °C and operation at T_2 = 300 °C. The length of bars represents the volume of the electrode materials at a given temperature and SOC, relative to that of the electrode compartments, $V_{a,eff}$ and $V_{c,eff}$ (figure 6-4b). Due to thermal expansion, the cathode material features a volume increase from 119 cm^3 to 134 cm^3 between cell closure and operation at 0% SOC. With increasing SOC, the filling level of the cathode decreases from 82 vol% to 70 vol%, while that of the anode material increases from 0 vol% to 69 vol%. The effect of variable temperatures at cell closure (T_1) and during operation (T_2) is depicted by the corresponding volume change of anode and cathode materials, $\Delta V_{m,a}$ and $\Delta V_{m,c}$ (figure 6-4b and c, figure 6-10, table 6-2). To assess the effects of local heat generation in case of cell failure, e.g. due to overcharge,[27] we consider not only normal battery operation at 300 °C, but also T_2 = 600 °C. Data for T_2 = 25 °C is given as reference, although Na-NiCl$_2$ cells with solidified Na and NaAlCl$_4$ are not operational. As sodium-ions from the cathode are plated at the anode as metallic sodium (mainly nickel and iron charging, reaction 12, 13), the volume of the anode material increases by 43.1 cm^3 at 25 °C, and by 50.2 cm^3 at 600 °C (figure 6-4b). Apart from differences in the initial cathode volume (thermal expansion, figure 6-4c), its decrease with increasing SOC is similar for all cell closure and operating temperatures (-20.1 cm^3 to -21.2 cm^3). Aluminum charging (reaction 11) adds a small deviation to this trend, forming NaAlCl$_4$ with low, temperature-dependent density at the cathode. As a result, the cathode material $V_{m,c}$ features a slight volume increase going from 0% to 6% SOC at T_2= 600 °C (figure 6-4c).
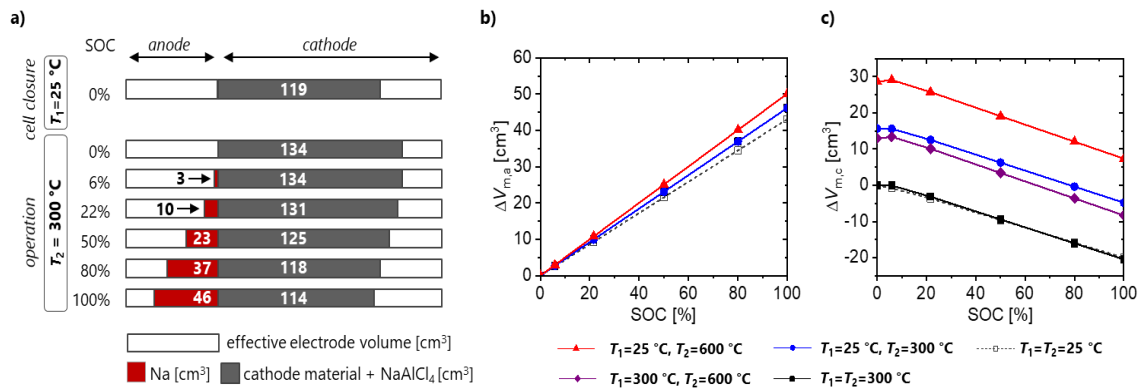
Figure 6-4: Quantification of volume changes in simplified Na-NiCl$_2$ cells. a) Effective electrode volumes ($V_{c,eff}$, $V_{a,eff}$) and volumetric evolution of anode and cathode materials for cell closure at T_1=25 °C and operation at T_2=300 °C. Numbers and length of bars represent volume [cm^3]. The effect of variable temperatures (T_1=25 °C or 300°C; T_2=25 °C, 300 °C or 600 °C) on the volume changes is shown in b) for the sodium anode, $\Delta V_{m,a} = V_{m,a2} - V_{m,a1}$,

and in c) for the cathode material + NaAlCl₄, $\Delta V_{m,c} = V_{m,c2} - V_{m,c1}$. The volume changes of anode materials in b) are independent of T_1, curves with the same T_2 overlap.

These volume changes of electrode materials, $V_{m,a}$ and $V_{m,c}$, lead to pressure changes in the (inert) gas volumes, $V_{g,a}$ and $V_{g,c}$, incorporated in the hermetically sealed electrode compartments (figure 6-3a, figure 6-4a). As the electrode materials are considered incompressible, the gas undergoes compression and expansion during charge and discharge cycling, compensating the volume changes of the electrode materials. For simplicity, we treat the effective volumes of the electrode compartments $V_{a,eff} = V_{g,a} + V_{m,a}$ and $V_{c,eff} = V_{g,c} + V_{m,c}$ as constant. According to the ideal gas law, the pressure p_2 in state 2 (= during operation) scales with pressure p_1 in state 1 (= at cell closure), with the corresponding temperatures T_2, T_1, and with the gas volumes V_2, V_1 according to

$$p_{a2} = p_{a1} \frac{V_{g,a1}}{V_{g,a2}} \frac{T_{a2}}{T_{a1}} , p_{c2} = p_{c1} \frac{V_{g,c1}}{V_{g,c2}} \frac{T_{c2}}{T_{c1}} \qquad \text{Equation 43}$$

Stresses in the ceramic electrolyte result from pressure differences between anode and cathode compartment:

$$\Delta p_2 = p_{a2} - p_{c2} \qquad \text{Equation 44}$$

Positive or negative Δp_2 lead to stresses on the electrolyte in one or the other direction. Especially for symmetrical planar cells, we aim at reducing the magnitude $|\Delta p_2|$ to reduce the maximum stress on the electrolyte. If anode and cathode compartments are sealed at the same temperature and pressure ($p_{a1} = p_{c1} = p_1$, $T_{a1} = T_{c1} = T_1$, see Section B in supporting information for further discussion), the pressure difference between the electrode compartments during operation simplifies to

$$\Delta p_2 = \frac{T_2}{T_1} p_1 \left(\frac{V_{g,a1}}{V_{g,a2}} - \frac{V_{g,c1}}{V_{g,c2}} \right) \qquad \text{Equation 45}$$

In this study, state 1 refers to cell closure at temperature T_1 in the discharged state (0% SOC), while state 2 refers to cell operation at T_2 and a given SOC. Accordingly, to reduce the pressure difference Δp_2 between the cell compartments we can adapt the cell design and processing based on three strategies, namely

(i) by increasing the temperature T_1 at which the electrode compartments are closed (or decrease T_2, but this is driven by the application),

(ii) by reducing the pressure p_1 at which the electrode compartments are closed (e.g. applying a vacuum), and

(iii) by balancing the volume of the two electrode compartments to minimize $\frac{V_{g,a1}}{V_{g,a2}} - \frac{V_{g,c1}}{V_{g,c2}}$.

To illustrate these strategies, the pressures resulting from the volume changes in figure 6-4 are shown in figure 6-5 for different temperature combinations and cell closure pressures (based on the electrode volumes according to figure 6-1). All data is summarized in table 6-2. For cell closure at ambient pressure, p_1 =1.013 bar, the cathode pressure p_{c2} (figure 6-

5a) and the anode pressure p_{a2} (figure 6-5b) range from 0.6 bar to 11.9 bar. Based on equation 41, this corresponds to pressure differences Δp_2 between -5.5 bar and +8.3 bar, and to maximum stresses on the electrolyte between -6.6 MPa and +10.0 MPa in the tubular cell geometry (figure 6-5c). In the planar geometry, the same Δp_2 lead to intolerably high stresses of up to 1.8 GPa (equation 42; figure 6-5c).

These pressures can be reduced by increasing the cell closure temperature according to strategy (i). If cells are closed at T_1=300 °C instead of T_1=25 °C, pressure differences Δp_2 during operation at T_2=600 °C range from -1.3 bar to +5.0 bar, with a maximum stress of 6.0 MPa for the tubular geometry. Nevertheless, intolerably high stress of up to +1.1 GPa remains for the planar geometry (figure 6-5c).
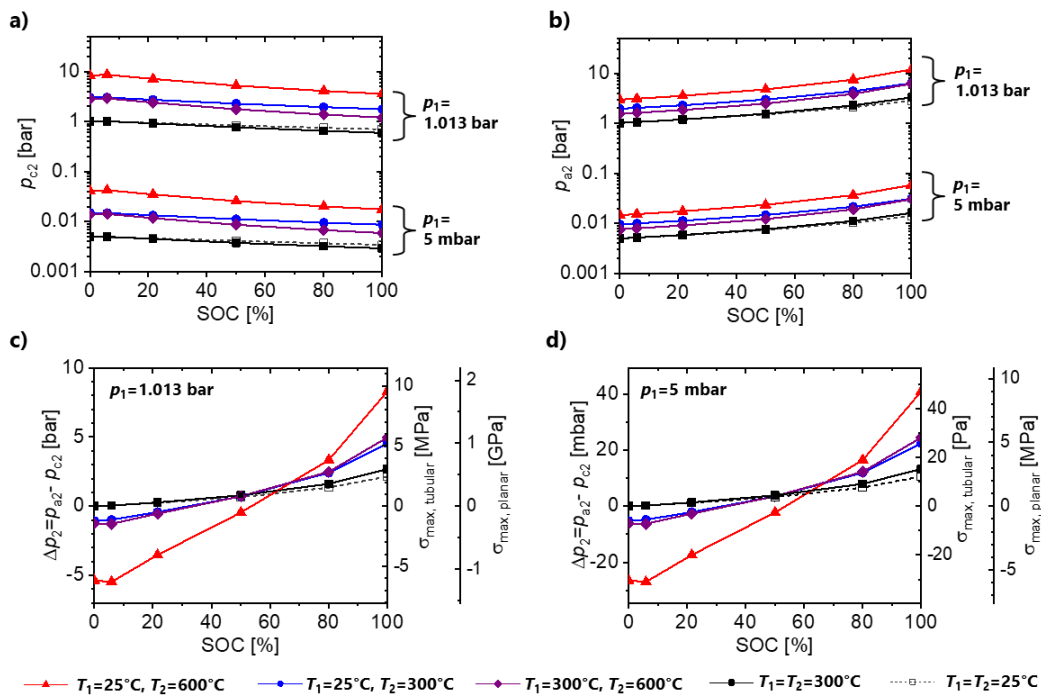
Figure 6-5: Pressure evolution in Na-NiCl₂ cells versus state of charge (SOC) for different cell closure (T₁, p₁) and operating conditions (T₂). a) Cathode pressure p_{c2} and b) anode pressure p_{a2} for cell closure at p_1 = 1.013 bar and at p_1 = 5 mbar. Corresponding pressure difference Δp_2 and maximum stresses $\sigma_{max,tubular}$ and $\sigma_{max,planar}$ acting on the electrolyte in tubular and planar cell geometry c) for cell closure at p_1 = 1.013 bar, and d) for cell closure at p_1 = 5 mbar. Legend applies to all graphs.

However, a drastical reduction in differential pressure is obtained by reducing the cell closure pressure according to strategy (ii). For p_1 = 5 mbar, the maximum stresses are reduced to 0.5% compared to p_1=1.013 bar (figure 6-5a,b). In this case, pressure differences Δp_2 range from -27 mbar and +41 mbar (figure 6-5d). The maximum stresses for the planar geometry range from -6.0 MPa to +9.0 MPa, which is comparable to those of the tubular geometry sealed at a cell closure pressure p_1 of 1.013 bar. Thus, cell closure at reduced

pressure is an effective means to maintain tolerable stress levels in a planar cell geometry. It is also compatible with state-of-the-art cathode assembly in Na-NiCl$_2$ cells with granulated cathode materials [15], which can be evacuated after the filling procedure.
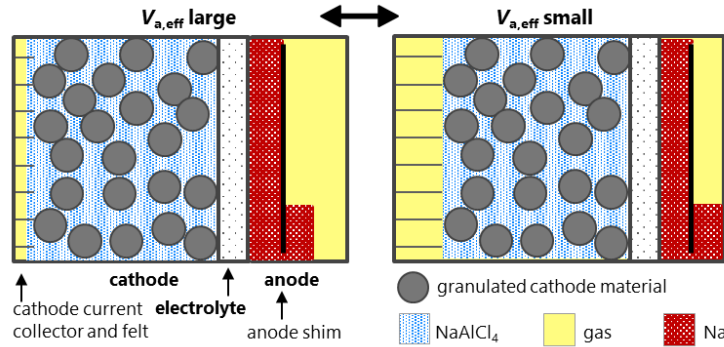
Figure 6-6: Variation of the effective electrode volumes at constant total electrode volume $V_{tot} = V_{a,eff} + V_{c,eff}$, shown schematically for SOC > 0%.

To balance the volumes of the electrode compartments according to (iii), we consider the situation depicted schematically in figure 6-6. For different SOC and operating temperatures (25 °C, 300 °C, or 600 °C), the volumes of the anode material range between 0 cm^3 and 50.2 cm^3, and those of the cathode materials range between 147.7 cm^3 and 98.6 cm^3. At a constant total electrode volume of e.g. V_{tot} = 230 cm^3, we may thus vary the size of the effective anode volume in the cell design 50.2 cm^3< $V_{a,eff}$ < 82.3 cm^3 to accommodate the electrode materials at all temperatures and SOC. Variations in the gas volume are enabled by the design of electrode shims, current collectors, or felts. The effective cathode volume is adapted according to V_{tot} =$V_{c,eff}$+$V_{a,eff.}$. The evolution of Δp_2 with $V_{a,eff}$, state of charge, and temperature is shown in figure 6-7 (p$_1$ = 1.013 bar), further considering different total electrode volumes V$_{tot}$. In general, $|\Delta p_2|$ features maximum values when the material volumes V$_{m,c}$ and V$_{m,a}$ approach the effective electrode volumes $V_{c,eff}$ and $V_{a,eff}$ at low and high SOC. The effective anode volume $V_{a,eff}$ can thus be chosen to minimize the magnitude $|\Delta p_2|$ to the range of temperature and SOC targeted for application. With more pronounced volume changes at the anode than at the cathode (figure 6-4), this is generally achieved by incorporating larger gas volumes in $V_{a,eff}$ than in $V_{c,eff}$ (figure 6-7; see also section C in supporting information).

For the specific cell geometry in figure 6-1 (V_{tot} = 230 cm^3), we obtain the situation depicted in figure 6-7e-h, with the effective anode volume V$_{a,eff}$ = 66.9 cm^3 marked by a dashed line. At T_1=25 °C and T_2=300 °C, this configuration results in pressure differences Δp_2 between -1.1 bar and +4.5 bar at 0% and 100% SOC, respectively (figure 6-7f). By increasing $V_{a,eff}$ close to its limits, $|\Delta p_2|$ can be reduced to < 2.8 bar. However, the situation changes at increased operating temperature: At T_1=25 °C and T_2=600 °C, an effective anode volume of $V_{a,eff}$ = 70 cm^3 would be ideal, restricting $|\Delta p_2|$ ≤ 6.9 bar (figure 6-7h).

Of course, Δp_2 is also strongly affected by the total electrode volume V_{tot}. In figure 6-7a-d, V_{tot} is decreased to 220 cm^3, resulting in high $|\Delta p_2| \geq 10$ bar at T_1=25 °C and T_2=600 °C (figure 6-7d). By increasing the total gas volume to V_{tot} = 300 cm^3 (figure 6-7i-l), the pressure difference can be reduced to $|\Delta p_2|$ < 2.1 bar at all SOC, selecting an anode volume of V$_{a,eff}$ ≈112 cm^3. However, this pressure difference still corresponds to a maximum stress of $\sigma_{max,planar} \approx 0.5$ GPa on the planar electrolyte structure in figure 6-1. Similar values are also obtained for (hypothetical) room temperature application (T_1=T_2=25 °C, figure 6-7a, e, i). Based on the criterion that Δp must thus not exceed 0.9 bar even at a high fracture strength of $\sigma_{fracture} = 200$ MPa, a planar cell design according to figure 6-1b thus requires cell closure at reduced pressure.

In future studies, an experimental assessment of pressures evolving in such cells, e.g. by high-temperature pressure transducers, could be of interest. This would also indicate if additional side reactions are of relevance. For example, here we did not include evaporation of Na and NaAlCl$_4$ at elevated sealing temperatures. As discussed in section B of the supporting information, this effect is small as it entails pressures of condensable vapors on the order of 10 mbar in the cell compartments.[30-32] Additionally, we did not include gravitational effects, as gravitational pressure resulting from material density, ρ, acceleration of free fall, g, and material height, h, at the electrodes according to $\Delta p = \rho\, g\, h$ is negligible for the geometries considered (e.g. 10^{-5} bar for Na at the bottom of a 20 cm high tube). We also did not consider bulging of the electrode compartments. Indeed, pressure differences would be compensated by electrode compartments expanding and contracting with the volume changes of the electrode materials. For T_1=25 °C and T_2=300 °C, this would require volume changes between +10 vol% and -3 vol% at the cathode with increasing SOC. The anode compartment would even be required to increase by +69 vol%. Integration of such severe volume changes in the cell design is challenging and may compromise the safety of solid-electrolyte battery stacks. Similarly, Δp_2 vanishes if the volume changes at anode and cathode correspond to each other at all times. This would require cathode materials featuring a volume increase of +0.9 cm^3 Ah^{-1} upon charging to match Na-metal anodes, or of + 0.4 cm^3 Ah^{-1} to match Li-metal anodes.
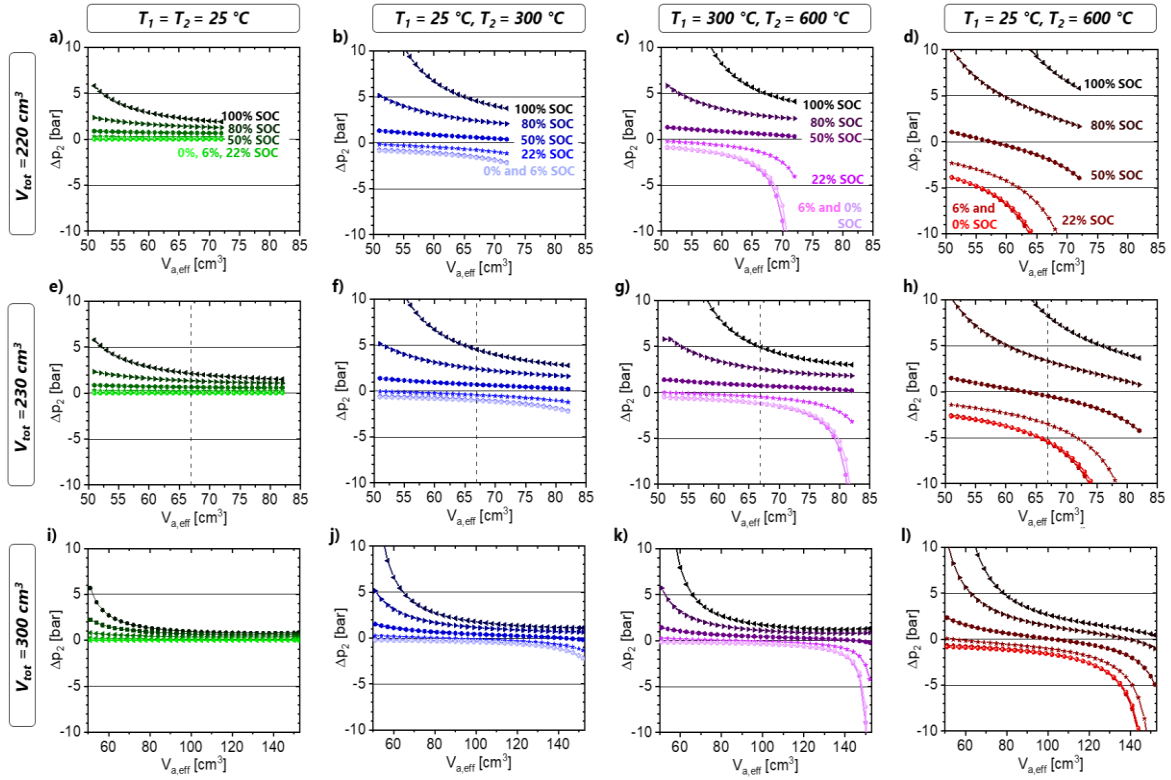
Figure 6-7: Evolution of pressure difference Δp_2 with change of effective anode volume $V_{a,eff}$ for different temperatures and SOC (p1 = 1.013 bar). Influence of total electrode volume a-d) V_{tot} = 220 cm³, e-h) V_{tot} = 230 cm³, and i-l) V_{tot} = 300 cm³, and influence of cell closure and operating temperatures a,e,i) T_1 = 25 °C, T_2 = 25 °C, b,f,j) T_1 = 25 °C, T_2 = 300 °C, c,g,k) T_1 = 300 °C, T_2 = 600 °C, d,h,l) T_1 = 25 °C, T_2 = 600 °C. Legend in a-d refers to all graphs.

6.3 Conclusion

In this study, we demonstrate how both electrochemical reactions and changes in temperature cause substantial volume changes of the electrode materials at different states of battery operation. These volume changes induce substantial pressure differences in the hermetically sealed electrode compartments of Na-NiCl$_2$ battery cells resulting in stresses acting on the ceramic β''-alumina electrolyte.

We show that planar cell designs are much more vulnerable to stress evolution than tubular designs. In Na-NiCl$_2$ batteries, as in most existing battery systems, the volume of the electrode materials ΔV_m changes with both SOC and temperature. Evolution of pressure differences in hermetically sealed battery cells during operation can be adapted by the choice of (i) temperature and (ii) pressure applied during sealing of the cell, as well as by (iii) a cell design providing volumetric balance of the gas volumes present in the electrode compartments.

In practical terms, reducing the pressure during cell closure is the most effective strategy to reduce pressure differences in planar battery cells to a level where maximum stresses on the solid electrolyte are non-critical.

6.4   Supporting information

a) tubular cell

		cathode	electrolyte	anode
$t_c=r_c$, $t_e=\Delta r_e$, $t_a=\Delta r_a$	[cm]	1.65	**0.15**	0.30
$l=l_c=l_e=l_a$	[cm]		20.0	
A	[cm^2]		**207.3**	
$V_{compartment}$	[cm^3]	171.1		73.5
$V_{contact}$	[cm^3]	8.0		6.6
$V_{c,eff}$, $V_{a,eff}$	[cm^3]	**163.1**		**66.9**
$V_{tot}=V_{c,eff}+V_{a,eff}$	[cm^3]	230.0		

b) planar cell

		cathode	electrolyte	anode
$r=r_c=r_e=r_a$	[cm]		8.12	
t_c , t_e , t_a	[cm]	0.83	**0.15**	0.35
A	[cm^2]		**207.3**	
$V_{compartment}$	[cm^3]	171.1		73.5
$V_{contact}$	[cm^3]	8.0		6.6
$V_{c,eff}$, $V_{a,eff}$	[cm^3]	**163.1**		**66.9**
$V_{tot}=V_{c,eff}+V_{a,eff}$ [cm^3]		230.0		

Table 6-1: Dimensions of simplified Na-NiCl$_2$ cells with a) tubular cell geometry (hollow circular cross section with closed bottom), and b) planarcell geometry (circular electrolyte). For the tubular cell, the thickness of cathode, electrolyte and anode correspond to tube radius $t_c=r_c$ and annuli $t_e=\Delta r_e$, $t_a=\Delta r_a$. The effective electrode volumes $V_{c,eff}$ and $V_{a,eff}$ are obtained by subtracting the volumes of contacting materials $V_{contact}$ (e.g. current collectors) from the compartment volumes $V_{compartment}$.

a) (cathode mass)

		m [wt%]	m [g]	V(25°C) [cm^3]
cathode material	**Ni**	54.3%	135.8	15.3
	NaCl	42.2%	105.5	48.6
	Fe	3.10%	7.75	1.0
	Al	0.37%	0.94	0.3
	Σ		250.0	65.2
secondary electrolyte	**NaAlCl$_4$**		107.4	53.4
	total		357.4	118.6

b)

	ρ(25°C) [g cm^{-3}]	α_l [10^{-6} K^{-1}]
Ni	8.90	13.4
NaCl	2.17	44.0
Fe	7.87	11.8
Al	2.70	23.1
NiCl$_2$	3.51	20*
FeCl$_2$	3.16	20*

Figure 6-8: Composition and material properties of the Na-NiCl$_2$ system. a) Simplified composition of Na-NiCl$_2$ cell with 250 g cathode material (47.5 Ah) as assembled in the discharged state. b) Density and linear thermal expansion coefficients α_l of the solid components[28] (*no reports for NiCl$_2$ and FeCl$_2$, values estimated; see figure 6-10 for influence of variable thermal expansion coefficients).
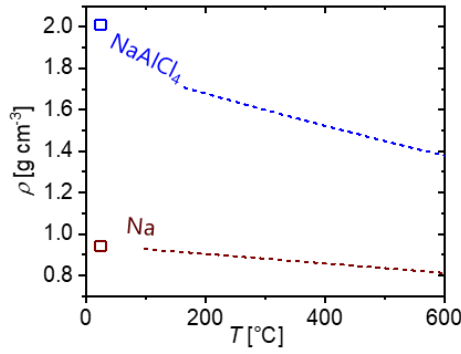
Figure 6-9: Temperature dependent density ρ of NaAlCl$_4$ and Na at room temperature (symbols) and in the molten state (dotted lines).[28, 29]
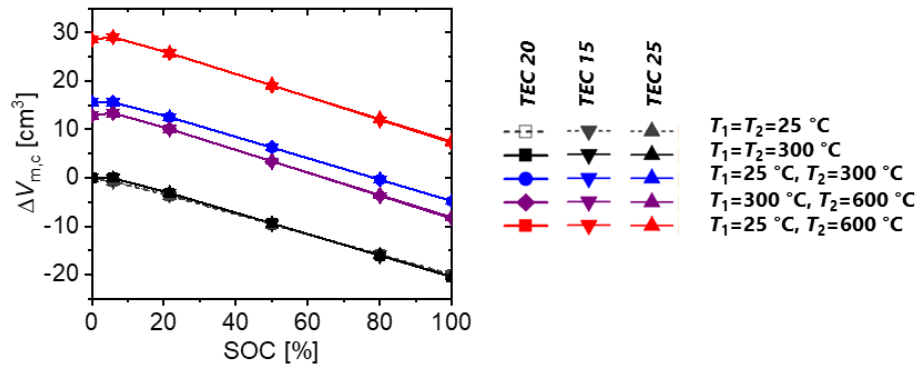
Figure 6-10: Quantification of volume changes at the cathode assuming variable thermal expansion coefficients for NiCl$_2$ and FeCl$_2$. Thermal expansion coefficients of 15·10^{-6} K^{-1} (TEC15), 20·10^{-6} K^{-1}(TEC20), and 25·10^{-6} K^{-1} (TEC25) do not significantly affected the volume changes of the cathode material.

a)

T_1=25 °C, T_2= 600 °C
p_1=1013 mbar
V_{c1}=118.63 cm²
V_{a1}=0 cm²

			p_1=1013 mbar			p_1=5 mbar		
SOC	$\Delta V_{m,a}$	$\Delta V_{m,c}$	p_{a2}	p_{c2}	Δp_2	p_{a2}	p_{c2}	Δp_2
	[cm²]	[cm²]	[bar]	[bar]	[bar]	[mbar]	[mbar]	[mbar]
0%	0.00	28.60	2.97	8.33	-5.36	14.64	41.11	-26.47
6%	2.95	29.05	3.10	8.57	-5.47	15.32	42.31	-26.99
22%	10.82	25.76	3.54	7.06	-3.52	17.47	34.85	-17.38
50%	25.08	19.09	4.75	5.20	-0.46	23.42	25.68	-2.26
80%	40.12	12.05	7.41	4.07	3.34	36.57	20.09	16.48
100%	50.15	7.36	11.85	3.56	8.29	58.46	17.55	40.91

b)

T_1=300 °C, T_2= 600 °C
p_1=1013 mbar
V_{c1}=134.31 cm²
V_{a1}=0 cm²

			p_1=1013 mbar			p_1=5 mbar		
SOC	$\Delta V_{m,a}$	$\Delta V_{m,c}$	p_{a2}	p_{c2}	Δp_2	p_{a2}	p_{c2}	Δp_2
	[cm²]	[cm²]	[bar]	[bar]	[bar]	[mbar]	[mbar]	[mbar]
0%	0.00	12.93	1.54	2.80	-1.26	7.62	13.84	-6.22
6%	2.95	13.37	1.61	2.89	-1.27	7.97	14.24	-6.27
22%	10.82	10.08	1.84	2.38	-0.54	9.09	11.73	-2.65
50%	25.08	3.41	2.47	1.75	0.72	12.18	8.64	3.54
80%	40.12	-3.62	3.86	1.37	2.48	19.02	6.76	12.26
100%	50.15	-8.32	6.16	1.20	4.97	30.41	5.91	24.50

c)

T_1=25 °C, T_2= 300 °C
p_1=1013 mbar
V_{c1}=118.63 cm²
V_{a1}=0 cm²

			p_1=1013 mbar			p_1=5 mbar		
SOC	$\Delta V_{m,a}$	$\Delta V_{m,c}$	p_{a2}	p_{c2}	Δp_2	p_{a2}	p_{c2}	Δp_2
	[cm²]	[cm²]	[bar]	[bar]	[bar]	[mbar]	[mbar]	[mbar]
0%	0.00	15.67	1.95	3.01	-1.06	9.61	14.85	-5.24
6%	2.72	15.61	2.03	3.00	-0.97	10.02	14.82	-4.80
22%	9.97	12.52	2.29	2.71	-0.42	11.29	13.39	-2.09
50%	23.11	6.24	2.98	2.27	0.71	14.68	11.18	3.50
80%	36.98	-0.38	4.35	1.93	2.42	21.48	9.53	11.96
100%	46.22	-4.80	6.30	1.76	4.54	31.08	8.67	22.41

d)

T_1=300 °C, T_2= 300 °C
p_1=1013 mbar
V_{c1}=134.31 cm²
V_{a1}=0 cm²

			p_1=1013 mbar			p_1=5 mbar		
SOC	$\Delta V_{m,a}$	$\Delta V_{m,c}$	p_{a2}	p_{c2}	Δp_2	p_{a2}	p_{c2}	Δp_2
	[cm²]	[cm²]	[bar]	[bar]	[bar]	[mbar]	[mbar]	[mbar]
0%	0.00	0.00	1.01	1.01	0.00	5.00	5.00	0.00
6%	2.72	-0.07	1.06	1.01	0.05	5.21	4.99	0.22
22%	9.97	-3.15	1.19	0.91	0.28	5.88	4.51	1.37
50%	23.11	-9.43	1.55	0.76	0.78	7.64	3.77	3.87
80%	36.98	-16.06	2.26	0.65	1.61	11.18	3.21	7.97
100%	46.22	-20.47	3.28	0.59	2.69	16.17	2.92	13.25

e)

T_1=25 °C, T_2= 25 °C
p_1=1013 mbar
V_{c1}=118.63 cm²
V_{a1}=0 cm²

			p_1=1013 mbar			p_1=5 mbar		
SOC	$\Delta V_{m,a}$	$\Delta V_{m,c}$	p_{a2}	p_{c2}	Δp_2	p_{a2}	p_{c2}	Δp_2
	[cm²]	[cm²]	[bar]	[bar]	[bar]	[mbar]	[mbar]	[mbar]
0%	0.00	0.00	1.01	1.01	0.00	5.00	5.00	0.00
6%	2.54	-0.77	1.05	1.00	0.06	5.20	4.91	0.28
22%	9.30	-3.67	1.18	0.94	0.24	5.81	4.62	1.19
50%	21.56	-9.59	1.50	0.83	0.66	7.38	4.11	3.27
80%	34.50	-15.84	2.09	0.75	1.34	10.32	3.69	6.64
100%	43.12	-20.01	2.85	0.70	2.15	14.06	3.45	10.62

Table 6-2: Volume and pressure changes with SOC at varaible cell closure and operation conditions. Cell geometry according to figure 6-1.

A) Packing density of cathode material and immersion in liquid NaAlCl4

The composition of cathode mass applied in this study features equal volumes of $NaAlCl_4$ and cathode materials at 300 °C. To assure immersion of the cathode material in liquid $NaAlCl_4$ at all SOC, a reservoir of liquid $NaAlCl_4$ is required, e.g. in a carbon felt. During charging from 0 % SOC to 100 % SOC at 300 °C, the volume of the solid cathode material decreases from 67.2 cm^3 to 46.7 cm^3, while the volume of liquid $NaAlCl_4$ remains constant at 67.2 cm^3. We assume an initial packing density of the cathode material of 59 vol% at 0 % SOC. At this condition, the liquid NaAlCl4 is contained in both the pore space (46.7 cm^3) and in the carbon felt reservoir (20.4 cm^3). At 100 % SOC, the packing density of the cathode material decreases to 41 %, and the remaining pore space of 67.2 cm^3 is fully occupied by liquid $NaAlCl_4$.

B) Vapor pressures of Na and NaAlCl₄

When deriving equation 45 from Equation 43 and 44, we assume that it is possible to seal the two cell compartments at the same temperature and pressure. This allows us to simplify the equation. However, it is true that both sodium and $NaAlCl_4$ evaporate at elevated temperatures and consequently a certain pressure will arise in both compartments, counteracting e.g. an evacuation to a very low pressure. In this context, it is important to note that the formed vapors are fully condensable and in a thermodynamic equilibrium with the active materials inside the anode and cathode compartment, respectively. Consequently, the maximum pressure arising due to the condensable vapors in the system corresponds to the respective saturation vapor pressure of the species in the compartment. For the case of sodium, the saturation vapor pressure is 0.02 mbar at 300 °C, and 34 mbar at 600 °C.[30] For $NaAlCl_4$, vapor pressures depend on the composition, namely the concentration of $AlCl_3$. In $Na-NiCl_2$ cells, NaCl-saturated $NaAlCl_4$ is used. For $NaAlCl_4$ with 49.5 mol% $AlCl_3$, the saturation vapor pressure is approximately 10 mbar at 600 °C and further decreases for decreasing temperatures.[31, 32] We conclude that the evaporation of Na and $NaAlCl_4$ can contribute to the arising pressure in the compartments at high temperatures. However, the contribution is limited to comparably small values so that our simplification in equation 45 is valid and enables to derive relevant strategies.

C) Optimizing the effective anode volume, $V_{a,eff}$

For a more general analysis of balancing the volumes of the electrode compartments and their respective gas volumes, we consider the volume changes of the electrode materials, $\Delta V_c = V_{m,c2} - V_{m,c1}$ and $\Delta V_a = V_{m,a2}$. For alkali-metal anode cells assembled in the discharged state ($V_{m,a1} = 0$, and $V_{g,a1} = V_{a,eff}$), equation 45 takes the form of

$$\Delta p_2 = p_1 \frac{T_2}{T_1} \left(\frac{V_{g,a1}V_{g,c2} - V_{g,c1}V_{g,a2}}{V_{g,a2}V_{g,c2}} \right) = \frac{T_2}{T_1} p_1 \frac{\Delta V_a V_{g,c1} - V_{a,eff}\Delta V_c}{(V_{a,eff} - \Delta V_a)(V_{g,c1} - \Delta V_c)} \qquad \text{Equation 46}$$

Hence, the magnitude of the pressure difference $|\Delta p_2|$ is reduced by substantially increasing $V_{g,a2}$ and $V_{g,c2}$ and thus the effective electrode volumes $V_{a,eff}$ and $V_{c,eff}$ in the denominator, but this negatively affects energy density and production cost of battery cells. The pressure difference Δp_2 vanishes if the volume changes at anode and cathode relate to the gas volumes present during cell closure according to $\frac{\Delta V_a}{\Delta V_c} = \frac{V_{a,eff}}{V_{g,c1}}$. However, as alkali-metal ions are transferred from anode to cathode, ΔV_a and ΔV_c typically feature opposite trends. For a given total electrode volume $V_{tot} = V_{c,eff} + V_{a,eff}$ we can thus determine optimal values for $V_{a,eff}$ from the extrema, $\frac{\partial \Delta p_2}{\partial V_{a,eff}} = 0$:

$$V_{a,eff} = \frac{(V_{tot}-V_{m,c1})\Delta V_a}{\Delta V_a+\Delta V_c} \pm \sqrt{\left(\frac{(V_{tot}-V_{m,c1})\Delta V_a}{\Delta V_a+\Delta V_c}\right)^2 - \frac{\left(V_{tot}-V_{m,c1}-\Delta V_c\right)^2\Delta V_a+\Delta V_c\,\Delta V_a^2}{\Delta V_a+\Delta V_c}} \qquad \text{Equation 47}$$

Considering that the material volumes at anode and cathode need to fit the corresponding electrode volumes at all times, minima according to equation 47 often lie outside the physical domain (see figure 6-7). In this case, Δp_2 decreases monotonically in $V_{a,eff}$, and we obtain an optimal $V_{a,eff}$ by equating $|\Delta p_2|$ at the ends of the operational range of interest, e.g. $\Delta p_2(100\% \text{ SOC}) = -\Delta p_2(0\% \text{ SOC})$, as applied above.

References

[1]   J. G. Kim, B. Son, S. Mukherjee, N. Schuppert, A. Bates, O. Kwon, M. J. Choi, H. Y. Chung, S. Park. Journal of Power Sources 282 (2015) 299–322.

[2]   J. Janek, W. G. Zeier. Nature Energy 1 (2016) 16141.

[3]   C. W. Sun, J. Liu, Y. D. Gong, D. P. Wilkinson, J. J. Zhang. Nano Energy 33 (2017) 363–386.

[4]   C. L. Zhao, L. L. Liu, X. G. Qi, Y. X. Lu, F. X. Wu, J. M. Zhao, Y. Yu, Y. S. Hu, L. Q. Chen. Advanced Energy Materials 8 (2018) 1703012.

[5]   P. Wang, W. J. Qu, W. L. Song, H. S. Chen, R. J. Chen, D. N. Fang. Advanced Functional Materials 29 (2019) 1900950.

[6]   M.-C. Bay, M. Wang, R. Grissa, M. V. F. Heinz, J. Sakamoto, C. Battaglia. Advanced Energy Materials (2019) 1902899.

[7]   T. Famprikis, P. Canepa, J. A. Dawson, M. S. Islam, C. Masquelier. Nature Materials 18 (2019) 1278–1291.

[8]   R. Koerver, W. B. Zhang, L. de Biasi, S. Schweidler, A. O. Kondrakov, S. Kolling, T. Brezesinski, P. Hartmann, W. G. Zeier, J. Janek. Energy & Environmental Science 11 (2018) 2142–2158.

[9]   M. Finsterbusch, T. Danner, C.-L. Tsai, S. Uhlenbruck, A. Latz, O. Guillon. ACS Applied Materials & Interfaces 10 (2018) 22329–22339.

[10]   K. Jung, J. P. Colker, Y. Z. Cao, G. Kim, Y. C. Park, C. S. Kim. Journal of Power Sources 324 (2016) 665–673.

[11]   R. Benato, N. Cosciani, G. Crugnola, S. D. Sessa, G. Lodi, C. Parmeggiani, M. Todeschini. Journal of Power Sources 293 (2015) 127–136.

[12]   Z. Wen, J. Cao, Z. Gu, X. Xu, F. Zhang, Z. Lin. Solid State Ionics 179 (2008) 1697 – 1701. Proceedings of the 16th International Conference on Solid State Ionics (SSI-16), Part II.

[13]   J. L. Sudworth. Journal of Power Sources 51 (1994) 105–114.

[14]   G. S. Li, X. C. Lu, J. Y. Kim, J. P. Lemmon, V. L. Sprenkle. Journal of Materials Chemistry A 1 (2013) 14935–14942.

[15]   J. L. Sudworth. J Power Sources 100 (2001) 149–163.

[16]   S. Krueger, T. Kentschke, H.-J. Barth. Multi-Axial Strength Data for Al_2O_3- and MgO-ZrO_2-Ceramics., Wiley, ISBN 9783527612765 (2007) pages 239–244.

[17]   F. Leckie, D. D. Bello (editors). Strength and Stiffness of Engineering Systems. Springer Science+Business Media (2009) page 277.

[18]   H. Altenbach. Holzmann/Meyer/Schumpich Technische Mechanik Festigkeitslehre, chapter 9. Springer (2014) pages 261–322.

[19]   K.-H. G. Feldhusen (editor). Dubbel Taschenbuch fuer den Maschinenbau. Springer (2014).

[20] P. Moseley. In J. L. Sudworth, A. R. Tilley (editors), The Sodium Sulfur Battery, chapter 2. Hall, Chapman and (1985) pages 17–76.

[21] X. Lu, G. Xia, J. P. Lemmon, Z. Yang. J Power Sources 195 (2010) 2431–2442.

[22] J. J. Petrovic. Metallurgical Transactions A 18 (1987) 1829–1834. ISSN 1543-1940.

[23] D. Reed, G. Coffey, E. Mast, N. Canfield, J. Mansurov, X. Lu, V. Sprenkle. J Power Sources 227 (2013) 94–100.

[24] R. C. Galloway, S. Haslam. Journal of Power Sources 80 (1999) 164–170. ISSN 0378-7753.

[25] C. H. Dustmann. J Power Sources 127 (2004) 85–92.

[26] R. Christin. Multiphysics modelling of sodium-nickel-chloride cells. Ph.D. thesis, Grenoble Alpes University (2015).

[27] K. Frutschy, T. Chatwin, R. Bull. J Power Sources 291 (2015) 117–125.

[28] J. R. Rumble. CRC Handbook of Chemistry and Physics. CRC Press, Taylor & Francis Group, 100th edition (2019).

[29] R. W. Berg, H. A. Hjuler, N. J. Bjerrum. J. Chem. Eng. Data 28 (1983) 251–253. ISSN 0021-9568.

[30] J. Fink, L. Leibowitz. Thermodynamic and transport properties of sodium liquid and vapor. Technical report, United States (1995).

[31] E. W. Dewing. J. Am. Chem. Soc. 77 (1955) 2639–2641. ISSN 0002-7863.

[32] H. Böhm. Materials for High-Temperature Batteries, chapter 21. John Wiley & Sons, Ltd. ISBN 9783527637188 (2011) pages 719–756.

7. Conclusion and outlook

The shift towards renewable electricity production and the further implementation of solar and wind power plants comes at the price of intermittency.[1] A formidable technology to mitigate the intermittency problem, providing peak-shifting abilities are batteries. The limited availability of lithium and cobalt used in current lithium-ion batteries will not allow large-scale electricity storage with this battery technology.[2] However, sodium-nickel-chloride batteries consist of relatively cheap and abundant materials, namely rock salt and nickel.[3] They provide great potential for large-scale electricity storage, but suffer currently from a reduced rate capability and high cell cost compared to lithium-ion batteries.[4]

This thesis provides design guidelines for next-generation sodium-nickel-chloride batteries with enhanced rate capability and discusses potential cost reduction. At the core of this work stands the deconvolution of transport processes by dedicated experiments at the negative and positive electrode of this battery type. The deconvolution led to the quantification of the rate-limiting processes, but also allowed the development of an advanced and detailed understanding of electrochemical conversion reactions on either electrode. The high-temperature electrochemical cell proved to be a reliable, modular tool allowing the assessment of the different transport processes as shown in chapters 3, 4, and 5.

The liquid sodium negative electrode in conjunction with a highly porous carbon coating proved to be not rate limiting in the temperature range of 140-250 °C, allowing current densities up to 2600 mA/cm^2 without any signs of limitation and/or dendrite formation in the Na-β"-alumina electrolyte.[5] Further, we showed 10 Ah/cm^2 of total capacity cycled, meeting the US Department of Energy goal for lithium metal anode batteries.[6] Even at an operating temperature of 140 °C, a current density of 100 mA/cm^2 is still achievable.[5] From the liquid sodium negative electrode no rate limitations are imposed to the overall performance of sodium-nickel-chloride battery.

At the positive electrode, mainly consisting of nickel and sodium chloride, an intrinsic rate limitation for planar model electrodes can be observed at current densities beyond 0.25 mA/cm^2 shown by the rate test for the nickel electrode in figure 4-2d. Beyond this current density, Ni^{2+} ions get locally depleted in the NaAlCl$_4$ secondary electrolyte, leading to a limited supply of reactants for the conversion reaction during charge and discharge. This diffusion limited process causes the rate limitation during chlorination and de-chlorination of the positive electrode and sets an intrinsic upper boundary for charging and discharging rates in sodium-nickel-chloride batteries. The cause of the diffusion limitation can either be mitigated by increasing the concentration of Ni^{2+} ions or by increasing the mobility of Ni^{2+} ions in the secondary electrolyte. The latter of which is favorable, as increased concentration leads to inhomogeneous chlorination that potentially causes isolation of active nickel from the electron conducting nickel structure. Possible detachment of nickel chloride from the electron conducting structure imposes a further risk of increased Ni^{2+}-ion concentration, as it harms the reversibility of the nickel chloride to nickel conversion reaction. The

effect of increased solubility on de-/chlorination behavior of transition metals can be demonstrated by comparing nickel and iron electrodes. Fe^{2+} ions have a 100 times higher solubility than Ni^{2+} ions, leading to a very inhomogeneous de-/chlorination and local pulverization of the iron electrode. Contrary to that, the nickel electrode forms a homogeneous nickel chloride conversion layer. The influence of solubility on electrode de-/chlorination behavior is thus of pivotal importance to enable an increased rate performance combined with long cycle life for metal-chloride electrodes.

In order to achieve capacities, which are relevant for practical applications, we studied porous nickel positive electrodes with an active nickel surface area of 3700 cm^2/g as deployed in commercial sodium-nickel-chloride batteries.[7] For these thick porous electrodes, we observed a rate limitation at a current density beyond 0.07 mA/cm^2 and therefore 3.5 times lower than in the planar model electrode case.[7] Note that this current is normalized by the corresponding active nickel area in the porous electrode (3700 cm^2/g). For the porous nickel electrode, we found that the global Na^+-ion transport in the $NaAlCl_4$ electrolyte to be rate limiting.[7]
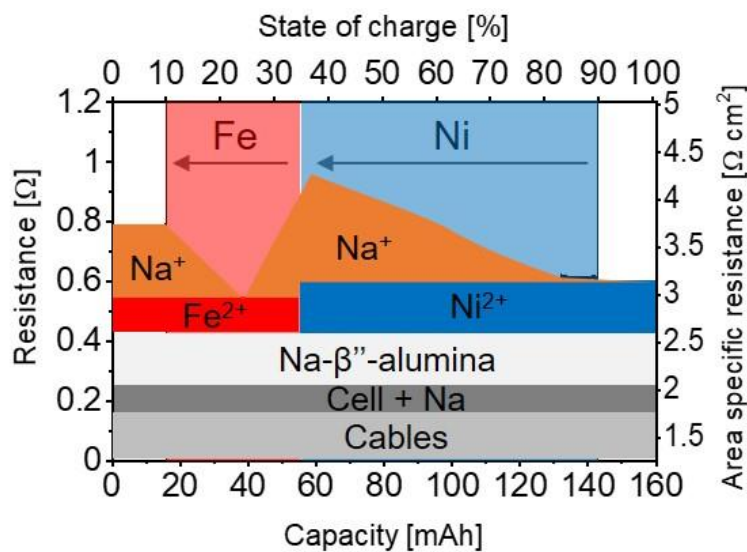
Figure 7-1: Contributions to overall cell resistance as function of state of charge, concluding the results of chapters 3-5.

Figure 7-1 shows the different contributions to the cell resistance during discharge at 0.07 mA/cm^2 for the experimental cell presented in chapter 5. Depending on state of charge the Na^+-ion transport is responsible for up to 40% of the entire cell resistance. This highlights the importance for the design of Na^+-ion pathways via larger pores in the nickel electrode and/or decreased transport path lengths (e.g. thinner electrodes, reduced tortuosity) in order to increase rate performance of sodium-nickel-chloride batteries.

Potential cost reduction for sodium-nickel-chloride batteries arises from replacement of the currently deployed tubular Na-β''-alumina electrolyte by a planar Na-β''-alumina electrolyte disc.[8] Reduction of geometric complexity to a planar disc leads to potential cost

reduction via facilitated production, quality surveillance, and improved failure statistics.[8] However, planar ceramic electrolytes are subject to severely higher mechanical stress than their tubular counterparts.[8] The mechanical stress arises from pressure differences between the hermetically sealed positive and negative electrode and due to temperature changes and cell cycling.[8] We found that the most practical solution to the problem is to seal positive and negative electrode at reduced pressure.[8] This mitigates the pressure difference arising from volume changes within the electrode compartments and allows implementation of planar Na-β"-alumina electrolyte discs.

With these conclusions, the following design-guidelines for next-generation sodium-nickel-chloride batteries can be proposed:

1. The liquid sodium negative electrode is not rate limiting, even at a low operation temperature of 140 °C. At the negative electrode no modification in terms of active area or surface-wetting enhancing agents are needed.
2. At current densities > 0.25 mA/cm^2 of active nickel electrode area, local Ni^{2+}-ion transport is limiting the rate capability of planar positive electrodes. Increased Ni^{2+} mobility in the $NaAlCl_4$ secondary electrolyte can increase the rate capability.
3. In thick, tortuous and porous electrodes, current densities > 0.07 mA/cm^2 lead to a rate limitation via Na^+-ion transport in the secondary electrolyte. Therefore, electrode pore size needs to be increased and electrode thickness and tortuosity reduced to accommodate a higher possible current density.
4. Increased mechanical stress on the planar electrolytes due to temperature change and cell cycling is mitigated via the reduction of atmospheric pressure during closing/sealing of the cell.

In this thesis, not every challenge for next-generation sodium-nickel-chloride batteries could be solved. I see particularly three open fields that should be addressed in next studies. First, the nickel de-/chlorination reaction should be implemented in a multi-physics model with exact geometric representation of the porous positive electrode, using the gathered parameters for charge transfer and diffusion as presented in chapter 4. This would enable the assessment of the two identified rate-limiting processes (e.g. Ni^{2+} & Na^+ transport) based on different current densities, state of charge and electrode microstructures. With the help of this model, electrode microstructure could be specifically designed to enhance rate capability while preserving energy density at the same time.

Second, in order to enhance Ni^{2+}-ion diffusion transport in the $NaAlCl_4$ secondary electrolyte at 300°C either solubility or mobility has to be increased, e.g. via increasing the $AlCl_3$ content in the $NaAlCl_4$ electrolyte[9] or by increasing the $NaAlCl_4$ viscosity.[10] Here the question arises if and if yes, which threshold of solubility is harmful for homogenous and re-

versible de-/chlorination of nickel. A comparative study about the de-/chlorination behavior at different Ni^{2+} concentrations in $NaAlCl_4$ could quantify the currently qualitative statements and enable a further increase in rate performance while maintaining cycle life.

A third point to mention is the substitution of nickel with iron or zinc as active material to reduce raw material cost. As presented in chapter 4, iron presents great rate capability but lacks reversible cycling and energy density. Here the de-/chlorination of iron and zinc has to be designed and tailored in detail to balance metal surface reactivity with electrolyte mobility and solubility to enable a homogeneous conversion reaction similar to nickel.

This thesis proposes measures to enhance rate capability and reduce cost of next-generation sodium-nickel-chloride batteries all with the aim to make them more competitive compared to lithium-ion batteries. The findings presented in this thesis offer stepping stones for the design of competitive large-scale grid storage batteries without use of critical raw materials,[11] enabling the incorporation of intermittently produced solar and wind energy into the electricity grid. Presently, electricity production accounts for one third of global CO_2 emissions,[12] this thesis is a further tiny puzzle piece for global CO_2 reduction and compliance to the Paris agreement on climate change.

References

[1]   D. H. Doughty, P. C. Butler, A. A. Akhil, N. H. Clark, J. D. Boyes, *Stationary electrical energy storage*, Electrochem. Soc. Interface, 2010, *19*, 49.

[2]   M. W. & S. P. Christoph Vaalma, Daniel Buchholz, *A cost and resource analysis of sodium-ion batteries*, Nat. Rev. Mater., 2018, *3*.

[3]   J. Coetzer, M. M. Thackeray, Patent: Cathode for an electrochemical cell and an electrochemical cell, US 4288506, 1978.

[4]   R. Benato, N. Cosciani, G. Crugnola, S. Dambone Sessa, G. Lodi, C. Parmeggiani, M. Todeschini, *Sodium-nickel-chloride battery technology for large-scale stationary storage in the high voltage network*, J. Power Sources, 2015, *293*, 127.

[5]   D. Landmann, G. Graeber, M. V. F. Heinz, S. Haussener, C. Battaglia, *Sodium plating and stripping from Na-β"-alumina ceramics beyond 1000 mA/cm^2*, Mater. Today Energy, 2020, *18*.

[6]   P. Albertus, S. Babinec, S. Litzelman, A. Newman, *Status and challenges in enabling the lithium metal electrode for high-energy and low-cost rechargeable batteries*, Nat. Energy, 2018, *3*, 16.

[7]   G. Graeber, D. Landmann, E. Svaluto-ferro, F. Vagliani, D. Basso, A. Turconi, M. V. F. Heinz, C. Battaglia, *Rational cathode design for high-power sodium-metal chloride batteries*, Adv. Funct. Mater., 2021, *2106367*.

[8]   M. V. F. Heinz, G. Graeber, D. Landmann, C. Battaglia, *Pressure management and cell design in solid-electrolyte batteries, at the example of a sodium-nickel-chloride battery*, J. Power Sources, 2020, *465*.

[9]   J. Prakash, L. Redey, D. R. Vissers, *Morphological considerations of the nickel chloride electrodes for zebra batteries*, J. Power Sources, 1999, *84*, 63.

[10] A. Ponrouch, E. Marchante, M. Courty, J. M. Tarascon, M. R. Palacín, *In search of an optimized electrolyte for Na-ion batteries*, Energy Environ. Sci., 2012, *5*, 8572.

[11] European Comission, Report: *Critical raw materials resilience: Charting a path towards greater security and sustainablity*, 2020.

[12] T. Goh, B. W. Ang, B. Su, H. Wang, *Drivers of stagnating global carbon intensity of electricity and the way forward*, Energy Policy, 2018, *113*, 149.

Curriculum vitae

Daniel Landmann

Mechanical Engineer • PhD Student in Renewable Energy Science and Engineering

Personal Details

Name:	Landmann, Daniel Alexander
Citizenship:	Basel, Switzerland
Nationality:	Swiss

Professional Experience

Since 2018	**PhD Student at EPFL and Empa, Swiss Federal Laboratories for Materials Science and Technology** in Dübendorf (Switzerland) at the laboratory Materials for Energy Conversion **PhD Thesis:** Design guidelines for next-generation sodium-nickel-chloride batteries, supervised by Dr. C. Battaglia and Prof. S. Haussener
2017	**Research Assistant at Empa, Swiss Federal Laboratories for Materials Science and Technology** in Dübendorf (Switzerland) at the laboratory Materials for Energy Conversion (501), Thermoelectrics
2011 – 2016	**Permanent Position at Dr. Ing. h.c. F. Porsche AG** in the R&D Center Weissach (Germany) in the department for Aerodynamics, Thermal Management and Thermal Protection (EGS) **Position:** Responsible for Thermal Protection Mid-Engine Sport Cars **Patent:** DE102013114658.9 "Arrangement for removing waste heat of an internal combustion engine"
2013 – 2014	**Deputy Team Leader** G06B (Aerodynamics, Thermal Management and Thermal Protection) Boxster/Cayman
2014 – 2016	**Deputy Head of Department** Thermal Protection, Porsche AG

Education

2008 – 2011	**Master Studies in Mechanical Engineering** at ETH Zurich Subject area: Energy, Flows and Processes, Composites **Master's degree:** 23.6.2011 (MSc. ETH Zurich in Mechanical Engineering)
2010 – 2011	**Master Thesis at Porsche Engineering Services GmbH** Thermomanagement of Vehicles with Alternative Drivetrains
2008	**Internship** at Dr. Ing. h. c. F. Porsche AG in the department for Aerodynamics and Thermal Protection (EGS1) Admission to the Porsche Talent Network
2004 – 2008	**Bachelor Studies in Mechanical Engineering** at ETH Zurich Co-initiator of the Formula Student Project at ETH Zurich **Teaching Assistant** at Autonomous Lab ETH Zurich

Skills and Expertise

Engineering	• Design of electrochemical battery cells • Design of battery calorimeters • Design of thermoelectric generators • Thermal design, development and testing of cars by experiments and simulation
Characterization methods	• Electrochemical characterization of battery materials and cells (galvanostatic, voltammetric and impedance spectroscopy) • Structural characterization using scanning electron microscopy, energy-dispersive x-ray spectroscopy and x-ray diffraction • Thermal characterization by calorimetry and thermal imaging • Multi-physics modeling of thermoelectric generators and batteries • Temperature measurement with thermocouples
Computational tools	Comsol, Matlab, Simulink, LabView, Igor, Excel VBA, MS Office, Bosch INCA, RADTherm, PowerFlow
Languages	German (native), English (full professional proficiency), French (limited professional proficiency)

Awards

Best Presentation Award at 2020 Materials Research Society (MRS) Fall Meeting
1st Poster Award at Empa PhD Symposium 2018
Admission to Dr. Ing. h.c. F. Porsche AG Talent Management 2008

Selected Publications

D. Landmann, G. Graeber, M.V.F. Heinz, S. Haussener, C. Battaglia, *Sodium stripping and plating from Na-β''-alumina beyond 1000 mA/cm^2*, Materials Today Energy, 2020, 100515

D. Landmann, Y. Tang, B. Kunz, R. Huber, D. Widner, P. Rickhaus, R. Widmer, H. Elsner, C. Battaglia, *Fabrication, characterization, and application-matched design of thermoelectric modules based on Half-Heusler FeNbSb and TiNiSn*, J. of Appl. Phys., 2019, 085113

D. Landmann, E. Svaluto-Ferro, M.V.F. Heinz, P. Schmutz, C. Battaglia*, Elucidation of the rate-limiting process in high-temperature metal-chloride batteries*, to be submitted

G. Graeber, D. Landmann, E. Svaluto-Ferro, M.V.F. Heinz, C. Battaglia, *Rational cathode design for high-power sodium-metal chloride batteries*, Adv. Funct. Mater., 2021, 2106367

Selected Presentations

International Sodium Battery Symposium IKTS	Dresden, Germany, Jan. 2021
Materials Research Society Fall Meeting (MRS)	Boston, MA, USA, Nov. 2020
Electrochemical Society (ECS) Pacific Rim Meeting	Honolulu, Hi, USA, Oct. 2020
2nd & 3rd Swiss Battery Days	Zürich, CH, Aug. 2019/Feb. 2021

List of figures

List of tables